

THE FORMATION OF HIGH-MASS STARS AND
STELLAR CLUSTERS IN THE EXTREME
ENVIRONMENT OF THE CENTRAL
MOLECULAR ZONE

Daniel Lewis Walker

A thesis submitted in partial fulfilment of the requirements of
Liverpool John Moores University
for the degree of
Doctor of Philosophy.
August 17, 2017

In loving memory of my grandmother, Anne Harding.
(1934 – 2015)

Acknowledgements

I am indebted to my supervisory committee – Steve Longmore, Nate Bastian and Toby Moore – for their help and guidance throughout. I would especially like to thank Steve Longmore for providing such excellent supervision, seeking out amazing opportunities and projects for me to join, and generally being a pleasure to work with.

I would like to express my gratitude to Qizhou Zhang, for providing me with the opportunity to spend a year working with him at the Harvard-Smithsonian Center for Astrophysics. I would also like to thank Charles Lada and Karin Öberg for their time and advice as part of my advisory committee at the CfA. I owe a special thanks to Cara Battersby, for all of her help and generally making me feel so welcome, particularly during my time at the CfA.

In addition to those already mentioned, I am thankful to all of those who contributed their time, effort and interest towards the work in this thesis. I would particularly like to thank Diederik Kruijssen, Adam Ginsburg, Thushara Pillai, Jonathan Henshaw, Jens Kauffmann, Eric Keto, Katharina Immer, Xing Lu, Ashley Barnes, Jill Rathborne, Andrew Walsh and Katharine Johnston for their consistent and invaluable feedback on numerous iterations of papers and proposals. I also thank Ben Davies and Nicolas Peretto for taking the time to act as the examiners for this thesis, and for their suggestions which greatly improved it.

Last, but certainly not least, I would like to thank all of my family and friends. To my parents, Allan and Jane, and my step-parents, Pete and Lisa, for their continued support and pride. To Amanda, for selflessly supporting me in this pursuit, and all of the quirks that came with it, along with her family, particularly her grandmother, Dot. And to my late grandmother and her partner, Anne and Alex, for I know how proud you both were, and that will forever be a source of inspiration.

Abstract

The process of converting gas into stars underpins much of astrophysics, yet many fundamental questions surrounding this process remain unanswered. For example – how sensitive is star formation to the local environmental conditions? How do massive and dense stellar clusters form, and how does this crowded environment influence the stars that form within it? How do the most massive stars form and is there an upper limit to the stellar initial mass function (IMF)? Answering questions such as these is crucial if we are to construct an end-to-end model of how stars form across the full range of conditions found throughout the Universe.

The research described in this thesis presents a study that utilises a multi-scale approach to identifying and characterising the early precursors to young massive clusters and high-mass proto-stars, with a specific focus on the extreme environment in the inner few hundred parsecs of the Milky Way – the Central Molecular Zone (CMZ). The primary sources of interest that are studied in detail belong to the Galactic centre ‘dust ridge’ – a group of six high-mass ($M \sim 10^{4-5} M_{\odot}$), dense ($R \sim 1-3$ pc, $n \gtrsim 10^4$ cm $^{-3}$), and quiescent molecular clouds. These properties make these clouds ideal candidates for representing the earliest stages of high-mass star and cluster formation. The research presented makes use of single-dish and interferometric far-infrared and (sub-)millimetre observations to study their global and small-scale properties.

A comparison of the known young massive clusters (YMCs) and their likely progenitors (the dust ridge clouds) in the CMZ shows that the stellar content of YMCs is much more dense and centrally concentrated than the gas in the clouds. If these clouds are truly precursors to massive clusters, the resultant stellar population would have to

undergo significant dynamical evolution to reach central densities that are typical of YMCs. This suggests that YMCs in the CMZ are unlikely to form ‘monolithically’. Extending this study to include YMCs in the Galactic disc again shows that the known population of YMC precursor clouds throughout the Galaxy are not sufficiently dense or central concentrated that they could form a cluster that then expands due to gas expulsion. The data also reveal an evolutionary trend, in which clouds contract and accrete gas towards their central regions along with concurrent star formation. This is argued to favour a ‘conveyor-belt’ mode of YMC formation and is again not consistent with a monolithic formation event.

High angular resolution observations of the dust ridge clouds with the Submillimeter Array are presented. They reveal an embedded population of compact and massive cores, ranging from $\sim 50 - 2150 M_{\odot}$ within radii of $\sim 0.1 - 0.25$ pc. These are likely formation sites of high-mass stars and clusters, and are strong candidates for representing the initial conditions of extremely massive stars. Two of these cores are found to be young, high-mass proto-stars, while the remaining 13 are quiescent. Comparing these cores with high-mass proto-stars in the Galactic disc, along with models in which star formation is regulated by turbulence, shows that these cores are consistent with the idea that the critical density threshold for star formation is greater in the turbulent environment at the Galactic centre.

Publications

The following is a list of published and submitted works that I have either led or been a part of over the course of the work presented in this thesis. The work in Chapter 2 is based upon that presented in Walker et al. (2015) [9]. Chapter 3 details a follow-up to this work that was published in Walker et al. (2016) [5]. Chapter 4 is based on a paper that has recently been submitted [1].

1. **Walker, D.**, Longmore, S. N., Zhang, Q., Battersby, C., Keto, E., Kruijssen, J. M. D., Ginsburg, A., Lu, X., Henshaw, J. D., Kauffmann, J., Pillai, T., Mills, E., Walsh, A. J., Bally, J., Ho, L. C., Immer, K., Johnston, K. G. (2017): *Star formation in a high-pressure environment: An SMA view of the Galactic centre dust ridge*, submitted to the Monthly Notices of the Royal Astronomical Society
2. Barnes, A. T., Longmore, S. N., Battersby, C., Bally, J., Kruijssen, J. M. D., Henshaw, J. D., **Walker, D.** (2017): *Star formation rates and efficiencies in the Galactic Centre*, submitted to the Monthly Notices of the Royal Astronomical Society
3. Lin, Y., Liu, H. B., Li, D., Zhang, Z-Y., Ginsburg, A., Pineda, J. E., Qian, L., Galvn-Madrid, R., McLeod, A. F., Rosolowsky, E., Dale, J. E., Immer, K., Koch, E., Longmore, S., **Walker, D.**, Testi, L. (2016): *Cloud Structure of Galactic OB Cluster-forming Regions from Combining Ground- and Space-based Bolometric Observations*, *Astrophysical Journal*, 828, 32
4. Battersby, C., Keto, E., Zhang, Q., Longmore, S. N., Kruijssen, J. M. D., Pillai, T., Kauffmann, J., **Walker, D.**, Lu, X., Ginsburg, A., Bally, J., Mills, E. A. C.,

- Henshaw, J. D., Immer, K., Patel, N., Tolls, V., Walsh, A. J., Johnston, K., Ho, L. C. (2016): *A Brief Update on the CMZoom Survey*, Astrophysics of the Galactic Centre Proceedings, IAU Symposium No. 322
5. **Walker, D.**, Longmore, S. N., Bastian, N., Kruijssen, J. M. D., Rathborne, J. M., Galvn-Madrid, R., Liu, H. B. (2016): *Comparing young massive clusters and their progenitor clouds in the Milky Way*, Monthly Notices of the Royal Astronomical Society, 457, 4536
 6. Longmore, S., Barnes, A., Battersby, C., Bally, J., Kruijssen, J. M. D., Dale, J., Henshaw, J., **Walker, D.**, Rathborne, J., Testi, L., Ott, J., Ginsburg, A. (2016): *Using young massive star clusters to understand star formation and feedback in high-redshift-like environments*, European Astronomical Society Publication Series, 75, 43
 7. Henshaw, J. D., Longmore, S. N., Kruijssen, J. M. D., Davies, B., Bally, J., Barnes, A., Battersby, C., Burton, M., Cunningham, M. R., Dale, J. E., Ginsburg, A., Immer, K., Jones, P. A., Kendrew, S., Mills, E. A. C., Molinari, S., Moore, T. J. T., Ott, J., Pillai, T., Rathborne, J., Schilke, P., Schmiedeke, A., Testi, L., **Walker, D.**, Walsh, A., Zhang, Q. (2016): *Molecular gas kinematics within the central 250 pc of the Milky Way*, Monthly Notices of the Royal Astronomical Society, 457, 2675
 8. Ginsburg, A., Walsh, A., Henkel, C., Jones, P. A., Cunningham, M., Kauffmann, J., Pillai, T., Mills, E. A. C., Ott, J., Kruijssen, J. M. D., Menten, K. M., Battersby, C., Rathborne, J., Contreras, Y., Longmore, S., **Walker, D.**, Dawson, J., Lopez, J. A. P. (2015): *High-mass star-forming cloud G0.38+0.04 in the Galactic center dust ridge contains H₂CO and SiO masers*, Astronomy Astrophysics, 584, 7
 9. **Walker, D.**, Longmore, S. N., Bastian, N., Kruijssen, J. M. D., Rathborne, J. M., Jackson, J. M., Foster, J. B., Contreras, Y. (2015): *Tracing the conversion of gas into stars in Young Massive Cluster Progenitors*, Monthly Notices of the Royal Astronomical Society, 449, 715

Contents

Contents	viii
List of Tables	xii
List of Figures	xiii
1 Introduction	1
1.1 Star formation – an overview	2
1.1.1 Probing the structure of molecular clouds	2
1.1.2 The stellar initial mass function (IMF)	7
1.1.3 Low-mass star formation	8
1.1.4 High-mass star formation	10
1.1.5 Star clusters	14
1.1.6 The formation of young massive clusters (YMCs)	15
1.1.7 The environmental dependence of star formation	18
1.2 The Central Molecular Zone – a laboratory for understanding extreme star formation	22
1.3 Goals of this work	23
1.4 Observing techniques: from far-IR to radio telescopes	24

1.4.1	Receivers: detecting long-wavelength light	24
2	Comparing young massive clusters and their gas-phase progenitors in the extreme environment of the Central Molecular Zone	29
2.1	Introduction	29
2.2	Results	30
2.2.1	Dust Column Densities & Temperatures	30
2.2.2	Dust Mass	34
2.2.3	Radius	35
2.2.4	Gas Velocity Dispersion	37
2.2.5	Virial masses	39
2.2.6	Time-scales	41
2.3	Discussion	41
2.3.1	Comparing Clouds & Clusters	43
2.4	Conclusions from Walker et al. (2015)	56
3	Comparing young massive clusters and their progenitors throughout the Milky Way	57
3.1	Introduction	57
3.2	Data	59
3.2.1	Galactic Centre	59
3.2.2	Galactic disc	60
3.3	Results	63
3.4	Discussion	70

3.4.1	‘Popping’ and ‘in-situ’ clusters – can Galactic clouds form a YMC at a high initial density?	72
3.4.2	On the clumpy sub-structure of molecular clouds	74
3.4.3	The peculiar shape of Westerlund 1	75
3.5	Conclusions from Walker et al. (2016)	76
4	Star formation in a high-pressure environment: An SMA view of the Galactic Centre dust-ridge	78
4.1	Introduction	79
4.2	Observations & Data	79
4.2.1	<i>CMZoom</i> – An SMA Legacy Survey of the Central Molecular Zone	79
4.3	Results	82
4.3.1	1.3mm Continuum Emission	82
4.3.2	Molecular Line Emission	85
4.4	Discussion	89
4.4.1	Young precursors to high-mass stars?	89
4.4.2	Do the properties of high-mass cores vary with environment?	91
4.5	Conclusions from Walker et al. (submitted)	97
4.6	Appendix: Gas Temperature Modelling	98
4.6.1	Line fitting	99
5	On-going and future work	110
5.1	A time-line for high-mass star assembly with ALMA	110

5.2	An ALMA view of a high-mass proto-star in the CMZ cloud G0.38+0.04113	
5.3	Searching for proto-cluster candidates with HOPS and ATLASGAL	116
6	Conclusions	125
6.1	Summary	125
6.2	Concluding remarks	127
A		
	SMA data calibration and imaging	129
B		
	Images of HOPS YMC precursor candidates	133
	Bibliography	148

List of Tables

2.1	Estimated global properties of clouds G0.253+0.016, 'd', 'e' and 'f' . . .	42
3.1	Summary of the global properties of the gas and stellar content at three distinct phases in three different formation scenarios for YMCs. . . .	59
3.2	Global properties of the sample of likely YMC progenitor gas clouds used in Walker et al. (2016).	65
3.3	Global properties of the sample of the YMCs used in Walker et al. (2016).	66
3.4	Mass contained within a radius of 0.1 pc for the clouds and clusters in Walker et al. (2016).	72
4.1	Global properties of the clouds observed with the SMA in Walker et al. (2017, submitted).	80
4.2	Summary of the SMA observations presented in Walker et al. (2017, submitted).	82
4.3	Summary of the identified cores in dust ridge clouds b–f as revealed by SMA observations, along with determined core properties from Walker et al. (2017, submitted).	86
5.1	Properties of the HOPS sources that have been identified as candidate precursors to YMCs.	119

List of Figures

1.1	Schematic of the general view of low-mass proto-stellar accretion (Hartmann et al., 2016).	11
1.2	Mass vs. radius for Galactic gas clouds and YMCs (Longmore et al., 2014a).	19
1.3	Star formation rate vs. molecular gas mass for local molecular clouds and galaxies (Lada et al., 2012).	20
2.1	Herschel (HiGAL) column density and temperature maps of the Galactic centre dust ridge.	31
2.2	Mass as a function of column density threshold for dust ridge clouds G0.253+0.016, ‘d’ ‘e’ and ‘f’.	35
2.3	Enclosed mass as a function of radius for dust ridge clouds G0.253+0.016, ‘d’ ‘e’ and ‘f’.	36
2.4	Spatially averaged HNCO line profiles for dust ridge clouds ‘d’ ‘e’ and ‘f’.	38
2.5	Integrated HNCO intensity maps of clouds ‘d’ and ‘e/f’.	40
2.6	Enclosed mass as a function of radius for G0.253+0.016, ‘d’, ‘e’, ‘f’ (given SFE = 1/3), the gas in Sagittarius B2 Main & North, and the stellar content of the Arches cluster.	50

2.7	Mass surface density profiles as a function of radius for G0.253+0.016, ‘d’, ‘e’, ‘f’ (given SFE = 1/3), the gas in Sagittarius B2 Main & North, the proto-cluster(s) embedded within Sagittarius B2 Main & North, and the stellar content of the Arches cluster.	51
2.8	Normalised mass surface density profiles as a function of radius for G0.253+0.016, ‘d’, ‘e’, ‘f’ (given SFE = 1/3), the gas in Sagittarius B2 Main & North, the proto-cluster(s) embedded within Sagittarius B2 Main & North, and the stellar content of the Arches cluster.	53
2.9	Mass surface density profiles as a function of radius for G0.253+0.016 and the stellar content of the Arches cluster. Shown is the limit above which a star formation efficiency greater than 100% would be required for G0.253 to form an Arches-like cluster at it’s current mass distribution. Also displayed is the mass-flow rate that would be required for a cloud like G0.253 to collapse to the mass distribution of an Arches-like cluster within a free-fall time, as well as the infall velocities that would be required for the cloud to collapse within a free-fall time.	54
3.1	Enclosed mass surface density profiles as a function of radius for the YMC precursor clouds in the CMZ and in the Galactic disc.	64
3.2	Enclosed mass surface density profiles as a function of radius for the Galactic (proto-)YMCs	65
3.3	Enclosed gas mass profiles as a function of radius for the known potential Galactic YMCs precursors.	71
3.4	Mass surface density profile of G0.253+0.016, overlaid with Plummer sphere models.	75
4.1	Three-colour image of the dust ridge at the Galactic centre, overlaid with the primary beam coverage of the SMA observations.	82

4.2	Dust ridge clouds ‘b’ – ‘f’ as seen with the SMA at 230 GHz and $\sim 3''$ – $4''$ angular resolution.	84
4.3	Mass-radius plot for all of the dust ridge cores uncovered with the SMA observations, along with high-mass proto-stellar cores in the Galactic disc from the literature.	93
4.4	Dust ridge clouds and cores in the context of the Field et al. (2011) model, showing that they may be gravitationally bound under the assumption of pressure equilibrium at $P/k \sim 10^8 \text{ K cm}^{-3}$	95
4.5	Gas temperature estimation as a function of the ratio of $3_{2,1}-2_{2,0}/3_{0,3}-2_{0,2}$ lines of para- H_2CO for different models.	100
4.6	<i>Top</i> : Integrated intensity map of the para- H_2CO $3_{0,3}-2_{0,2}$ transition towards ‘c1’. <i>Bottom</i> : Spatially-averaged spectrum of the para- H_2CO lines.	104
4.7	<i>Top</i> : Integrated intensity map of the CH_3CN J=12–11 k-ladder towards ‘c1’. <i>Bottom</i> : Spatially averaged spectrum of the CH_3CN J=12–11 k-ladder.	105
4.8	<i>Top</i> : Integrated intensity map of the para- H_2CO $3_{0,3}-2_{0,2}$ transition towards ‘c2’. <i>Bottom</i> : Spatially-averaged spectrum of the para- H_2CO lines.	106
4.9	<i>Top</i> : Integrated intensity map of the para- H_2CO $3_{0,3}-2_{0,2}$ transition towards ‘d2’. <i>Bottom</i> : Spatially-averaged spectrum of the para- H_2CO lines.	107
4.10	<i>Top</i> : Integrated intensity map of the para- H_2CO $3_{0,3}-2_{0,2}$ transition towards ‘d6’. <i>Bottom</i> : Spatially-averaged spectrum of the para- H_2CO lines.	108

4.11	<i>Top</i> : Integrated intensity map of the para-H ₂ CO 3 _{0,3} -2 _{0,2} transition towards ‘e1’. <i>Bottom</i> : Spatially-averaged spectrum of the para-H ₂ CO lines.	109
5.1	The four high-mass dust ridge cores that are being targeted with ALMA at 230 GHz and 0.13'' resolution.	111
5.2	ALMA 230 GHz continuum image of cores ‘e1’ and ‘e2’ in dust ridge cloud ‘e’ (G0.489-0.010)	112
5.3	Three-colour image of dust ridge cloud ‘c’ (G0.38+0.04).	113
5.4	Overview of the masers detected towards dust ridge cloud ‘c’ (G0.38+0.04).	115
5.5	ALMA 86 GHz continuum image of cores ‘c1’ and ‘c2’ in dust ridge cloud ‘c’ (G0.38+0.04).	115
5.6	Mass-radius plot for 605 sources from the HOPS catalogue.	119

Chapter 1

Introduction

Preface

This thesis presents a study of the Galactic centre ‘dust ridge’ – a group of six high-mass ($M \sim 10^{4-5} M_{\odot}$), dense ($R \sim 1-3$ pc, $n \gtrsim 10^4$ cm $^{-3}$), and quiescent molecular clouds that lie at a projected galactocentric distance of ~ 100 pc, and span roughly 37 pc in projected longitude. The research presented focuses primarily on studying these clouds observationally in the context of the very early stages of high-mass star and cluster formation in this extreme environment.

The outline of this thesis is as follows: this chapter presents an overview of the current understanding of the process of star formation (§1.1), with particular focus on the fields that are pertinent to this research, namely young massive cluster (YMC) formation, high-mass star formation and the environmental dependence of the star formation process. Chapter 2 presents a study in which the properties of these dust ridge clouds are derived. The properties of these clouds are compared with those of YMCs in the Galactic centre and discussed in the context of YMC formation scenarios. These results are published in Walker et al. (2015). Chapter 3 extends the research of the previous chapter to include YMCs and their likely precursor clouds in the Galactic disc, the results of which are published in Walker et al. (2016). Chapter 4 presents high

angular resolution observations of the dust ridge clouds using the Submillimeter Array (SMA). These observations reveal a population of high-mass dust cores, ranging from quiescent cores to young, embedded, high-mass proto-stars. Chapter 5 gives a brief discussion of active projects to follow up the discovery of these high-mass cores using ALMA, as well as a preliminary search for the quiescent precursors to YMCs in the Galactic disc. A summary of this work and future directions in the field are given in Chapter 6.

1.1 Star formation – an overview

The mechanisms by which stars form, evolve and deposit their energy, momentum and enriched material into the interstellar medium influence processes across a huge range of scales, from the formation of planets to the evolution of galaxies. The ultimate goal of star formation is to develop a general theory of the process that describes the formation of stars across the full mass range and as a function of their natal environment. Significant advances in pursuit of this goal have been made over recent decades, particularly in understanding the formation of low and intermediate mass stars in the disc of our own Galaxy, where we are able to resolve pre/proto-stellar cores on spatial scales on which individual stars are forming. However, there remain many open questions surrounding the nature of star formation outside of these circumstances. In the following sections, a brief overview of the current understanding in the field of star formation is presented.

1.1.1 Probing the structure of molecular clouds

Molecular clouds are the birthplaces of stars in galaxies. They are the coldest (10–20 K) and densest ($n_H \sim 10^{2-5} \text{ cm}^{-3}$) component of the interstellar medium (ISM) (Larson, 2003). Though such properties are ideal for forming stars, they are not so

ideal from our perspective as observers. The most abundant constituent of molecular clouds – Hydrogen – is in its molecular form, H_2 . In this form, Hydrogen is very difficult to observe as it does not emit efficiently at the low temperatures observed in molecular clouds. One of the best proxies for tracing the bulk of the material in these clouds comes in the form of thermal emission from dust grains. Dust is ubiquitous in molecular clouds and is observed to be present at a roughly constant ratio of 1:100 with respect to the gas, though this will change with metallicity, and in regions like the Galactic centre may be up to a factor of 2 lower than this (see e.g. Longmore et al., 2013a, and references therein). The dust grains are able to absorb and emit continuum radiation and therefore provide an excellent tool with which to observe the bulk physical properties of molecular clouds.

To observe the dust emission from molecular clouds, we must target the most appropriate wavelengths. Given typical temperatures in molecular clouds of $\sim 10\text{--}30$ K, the dust emits most efficiently in the (sub)-millimetre regime. At shorter wavelengths, the dust grains emit much less efficiently and they absorb background emission from stars and stand out as absorption features. This can be demonstrated via inspection of the equation of radiative transfer, which can be written as follows –

$$I_\nu = I_\nu(0)e^{-\tau_\nu} + B_\nu(T)[1 - e^{-\tau_\nu}] \quad (1.1)$$

where I_ν is the intensity, $I_\nu(0)$ is the initial intensity, τ_ν is the optical depth and $B_\nu(T)$ is the Planck function, which describes the intensity of radiation at a given frequency that is emitted from a black-body at a temperature, T –

$$B_\nu(T) = \frac{2h\nu^3}{c^2} \frac{1}{\exp(h\nu/kT)} \quad (1.2)$$

Equation 1.1 can effectively be split up into multiple terms. $I_\nu(0)e^{-\tau_\nu}$ describes the intensity ($I_\nu(0)$) of background radiation that is incident upon the far side of the absorbing material (from the observer’s perspective). This incident radiation is attenuated by the absorbing material, the amount by which is given by the optical depth, τ_ν , which

depends on the amount of material along the line of sight (i.e. column density) and the opacity of the material. The $B_\nu(T)[1 - e^{-\tau_\nu}]$ term describes the intensity of the black-body emission at temperature T , and its attenuation due to the optical depth.

At short wavelengths (high frequency) and typical cloud temperatures of $\sim 10\text{--}20$ K, the exponential term in the Planck function is significant (since $h\nu \gg kT$) and hence $B_\nu(T)$ becomes negligible. Equation 1.1 can therefore be simplified and approximated as $I_\nu = I_\nu(0)e^{-\tau_\nu}$, and hence a cloud would be observed as an extinction feature at short wavelengths.

At longer (e.g. sub-millimetre) wavelengths and the same temperature, $h\nu < kT$ and so the Planck function is no longer negligible. However, typical dust opacities in the sub-mm regime are $\kappa_\nu \sim 0.01 \text{ cm}^2 \text{ g}^{-1}$, which means that the $e^{-\tau_\nu}$ terms in Equation 1.1 are negligible (unless the cloud has extremely high column densities). The equation can therefore be approximated as $I_\nu = \tau_\nu B_\nu(T)$. Given that $\tau_\nu = \Sigma \kappa_\nu$, where Σ is the surface density, this means that if we have a measure of both the dust temperature and opacity, it is possible to determine the surface density and related physical properties such as the column density and cloud mass. Sub-mm/far-IR observations of molecular clouds are therefore ideal for measuring bulk cloud properties via the thermal dust continuum emission.

Observations of molecular clouds at these longer wavelengths has revealed that the internal structure of molecular clouds is not regular – it is clumpy, highly sub-structured and hierarchical (e.g. Larson, 1981; Elmegreen, 2008). This complex morphology has led to a non-universal nomenclature that is used to classify different structures within molecular clouds. In general, over-densities on the scales on which clusters of stars can form ($\sim 0.1 - 1$ pc) are referred to as ‘clumps’. Within these clumps, compact ($\ll 0.1$ pc) over-densities in which individual stars/binaries/multiples form are referred to as ‘cores’ (McKee & Ostriker, 2007).

Star formation in these cores occurs when self-gravity dominates and the core collapses. Classically, Jeans analysis (Jeans, 1902), which describes the conditions in which an over-density in a uniform isothermal medium is susceptible to gravitational

collapse, has been used to describe this process. Jeans (1902) considered the growth of plane-wave density perturbations in the medium. The density perturbations can be described by the standard form of the wave equation: $\rho = Ae^{i(kx-\omega t)}$. The propagation of such waves in the medium can be characterised by the dispersion relation –

$$\omega^2 = k^2 c_s^2 - 4\pi G \rho_0 = c_s^2 (k^2 - k_J^2) \quad (1.3)$$

where ω is the angular frequency, k is the wavenumber ($k = 2\pi/\lambda$), G is the gravitational constant, ρ_0 is the volume density, $c_s = \sqrt{kT/\mu}$ is the sound speed and $k_J = \sqrt{(4\pi G \rho_0)/c_s^2}$ is the Jeans, or critical, wavenumber. If $k < k_J$, this means that $\omega^2 < 0$ and ω must therefore be imaginary, with solutions of $\omega = \pm i\alpha$. The positive solution to ω yields a positive exponent in the wave equation, and $k < k_J$ therefore corresponds to exponential growth of the perturbations. Thus, *Jeans instability* occurs if the wavenumber (k) is smaller than the critical wavenumber (k_J). Expressed in terms of the wavelength ($\lambda = 2\pi/k$), we obtain the *Jeans length* –

$$\lambda_J = \frac{2\pi}{k_J} = c_s \pi^{1/2} (G \rho_0)^{-1/2} = \left(\frac{\pi k T}{G \rho_0 \mu} \right)^{1/2} \quad (1.4)$$

Assuming spherical symmetry the *Jeans mass* can be described as –

$$M_J = \frac{4\pi}{3} \lambda_J^3 \rho_0 = \frac{4\pi^{5/2} c_s^3}{3G^{3/2} \rho_0^{1/2}} = \left(\frac{\pi^5 k^3 T^3}{G^3 \rho_0 \mu^3} \right)^{1/2} \quad (1.5)$$

The Jeans analysis is a simplistic formulation and neglects many important physical processes, including those of rotation, magnetic fields, turbulence, external pressure and the detailed geometry of the medium. More detailed formulations exist (see Larson, 2003, and references therein), but the Jeans analysis provides a useful framework in which to make approximations for the formation properties of self-gravitating cores in molecular clouds. It also presents a way of explaining the observed fragmented hierarchical structure of the ISM. If regions that exceed the Jeans criteria collapse and remain isothermal, the Jeans mass will decrease as the density of the medium increases,

and hence smaller regions that exceed this mass will be susceptible to collapse. As regions fragment, they will at some point reach high enough densities that they will become optically thick and the temperature of the fragments will begin to increase. As the Jeans mass is more sensitive to the temperature than the density, this increase in temperature leads to a significant increase in the Jeans mass, and hence no further fragmentation should occur.

While gravity plays an obvious role in shaping the internal structure in molecular clouds, it is not the only factor at play. Turbulence is known to be fundamental in governing the properties of the ISM, and indeed all astrophysical phenomenon involving gas dynamics (see the review by McKee & Ostriker, 2007). Turbulence arises when the inertial forces in a fluid are much greater than its viscosity. This results in large scale instabilities that cascade energy down to smaller spatial scales. Turbulent motions within molecular clouds are often found to be greater than the sound speed in the medium, resulting in supersonic shocks that create regions of enhanced density. Supersonic turbulence within the ISM leads to these post-shock density fluctuations over a wide range of spatial scales, and if any density enhancements are significant enough, they may be susceptible to gravitational collapse, and hence the formation of (proto-)stars. However, unlike gravity, turbulent motions need not be conducive to forming structures, and can equally disrupt the density structure of the gas. The complex interactions between turbulent flows and gravity in the interstellar medium are therefore fundamental in regulating the density structure and hence star forming potential of molecular clouds.

Many numerical simulations have shown that the predicted distribution of densities – the probability distribution function (PDF) – is well described by a log-normal distribution (e.g. Nordlund & Padoan, 1999; Ostriker et al., 2001). This form of distribution can be explained as being due to the gas experiencing many random, independent shocks that change the density (Vazquez-Semadeni, 1994). As the shocks are random and additive, the form of the PDF therefore approaches a log-normal distribution, as per the central limit theorem. The mean of the density fluctuations grows as \mathcal{M}^2 , where \mathcal{M} is the Mach number (Padoan et al., 1997). When self-gravity becomes important

(i.e. the formation and subsequent collapse of self-gravitating cores), the density PDF is expected to remain log-normal, with the addition of a power-law tail at the high densities, corresponding to the dense, self-gravitating material (Nordlund & Padoan, 1999). These theoretical predictions have been shown to hold observationally. Measurements of the column density PDF have shown that Galactic molecular clouds are consistent with log-normal distributions due to turbulence (Padoan et al., 2014). It therefore seems that turbulence may play a dominant role in seeding the multi-scale structure of molecular clouds. It has also been predicted that turbulence alone may be responsible for determining the stellar initial mass function, whereby the highest density regions in the turbulent medium become self-gravitating, separate from the flow and collapse as proto-stellar cores (e.g. Krumholz & McKee, 2005; Padoan & Nordlund, 2011).

1.1.2 The stellar initial mass function (IMF)

The probability distribution of stellar masses at their birth (i.e. once they arrive at the zero-age main sequence) is known as the stellar initial mass function (IMF). A fascinating property of the IMF is that there is significant evidence that it is universal, in that it does not appear to vary significantly as a function of the initial conditions of star formation, though potential sources of variation have been found (see the review by Bastian et al., 2010, and references therein). It is not immediately obvious why the IMF should be invariant. It seems plausible to assume that the different environmental conditions and varying elemental abundances in the media from which stars form might have a significant effect on the resultant stellar population and its initial distribution of masses. If the IMF is truly universal, this has wide reaching implications for many areas of astrophysics. It would mean that a star of any mass (within the potential mass limits) has some probability of forming in any stellar population, and the number of high mass stars relative to low mass stars is crucial to the energy balance and evolution of galaxies. Thus, any endeavours to develop a unifying theory of star formation must be able to replicate this apparent universality of the stellar IMF.

There are multiple formulations of the stellar IMF. Initially, Salpeter (1955) proposed a distribution of the form $dN/d\log(M) \propto M^{-1.35}$. This single power-law form describes the stellar mass function for stars greater than $\sim 1 M_{\odot}$. However, it breaks down for lower stellar masses. More recent measurements of the IMF, which are more sensitive to the lower end of the mass spectrum, find that it is better represented by a multi-component form. For example, Chabrier (2003) propose a log-normal distribution for $M \lesssim 1 M_{\odot}$ followed by a power law, and Kroupa (2001) suggest a three-component power law series that is characterised as $dN/d\log(M) \propto M^{-\alpha}$, with $\alpha = 1.3$ for $0.5 < M/M_{\odot} < 50$, $\alpha = 0.3$ for $0.08 < M/M_{\odot} < 0.5$, and $\alpha = 0.7$ for $0.01 < M/M_{\odot} < 0.08$. In these models, the mean stellar mass at birth is of order $0.1 M_{\odot}$, with a steep drop-off for stars $\gtrsim 1 M_{\odot}$.

Understanding how stars form across the mass range, and whether their formation mechanisms differ as a function of mass, is crucial in understanding the apparent universality of the IMF. The following sections present an overview of theories of low- and high-mass star formation.

1.1.3 Low-mass star formation

The form of the IMF means that in a given stellar population, the vast majority of the stars will populate the lower end of the distribution. A consequence of this is that low-mass stars and their progenitors are much more abundant in the Galaxy relative to high-mass stars. Although the stellar mass distribution is continuous, a star is considered to be ‘high-mass’ when it is $\gtrsim 8 M_{\odot}$. This separation of low- and high-mass stars is a physically motivated one. One reason for this separation is that a star of $\gtrsim 8 M_{\odot}$ is sufficiently massive to be a type II supernova progenitor (Zinnecker & Yorke, 2007). In a more direct context of star formation, this low/high mass separation is also motivated by the physical timescales involved. The Kelvin-Helmholtz timescale is the approximate time that it would take for a star to radiate away its gravitational potential energy at its current luminosity, and can be described as –

$$t_{KH} = \frac{1}{2} \frac{E_G}{L_*} \approx \frac{GM_*^2}{R_* L_*} \quad (1.6)$$

where E_G is the gravitational potential energy, G is the gravitational constant, and M_* , R_* and L_* are the mass, radius and luminosity of the star, respectively. This timescale is roughly ~ 10 Myr for a Solar-like star. For low-mass stars, the Kelvin-Helmholtz timescale is significantly longer than the accretion timescale, and they can therefore accrete all of their mass before they enter the ZAMS. For high-mass stars ($\sim 8\text{--}10 M_\odot$), however, the opposite is true – the accretion timescale is greater than t_{KH} . This means that high-mass proto-stars initiate nuclear burning and enter the main sequence whilst still accreting, which has important implications for the continued growth and evolution of the proto-star (e.g. because of the interplay between stellar feedback and accretion).

The inherent abundance of low–intermediate-mass stars in the Galaxy means that there are many of these stars much closer to us, which permits detailed studies of the different phases of their evolution, and thus their formation is relatively well understood.

Low-mass stars are understood to form due to the collapse of self-gravitating proto-stellar cores (see e.g. reviews by Larson, 2003; McKee & Ostriker, 2007). During the early stages of the collapse, the dust is optically thin, and so the temperature of the core is expected to change very little while the density of the core increases significantly, and the proto-star is therefore often treated as being isothermal at this stage. Once high enough central densities are reached, the dust becomes optically thick and the core is opaque to its own radiation and can no longer be treated as isothermal (Larson, 1969). The increasing core temperature provides internal support against the global gravitational collapse and the core becomes hydrostatic at central densities of $\sim 10^{-10} \text{ g cm}^{-3}$. Eventually, the increasing central temperature is such that molecular hydrogen will begin to dissociate ($T \sim 2000 \text{ K}$). This leads to a subsequent second collapse within the first hydrostatic core, due to the fact that any compressional heating will go into dissociating the molecular hydrogen, rather than heating the gas. The core can then contract in an almost isothermal manner, until most of the H_2 has been disso-

ciated. This collapse halts once most of the hydrogen within the core has been ionised, and a second hydrostatic core is formed. The formation of the second hydrostatic core corresponds to the birth of the proto-star, which continues to grow towards its final stellar mass via accretion of the outer core and extended envelope material. This is a broad and overly-simplistic view of the process, and more thorough treatments include the effects of turbulence, rotation and magnetic fields (see e.g. reviews by Larson, 2003; McKee & Ostriker, 2007, and references therein).

The most notable consequence of including rotation and magnetic fields is the formation of a flattened accretion disc surrounding the proto-star. Indeed, discs around low-mass proto-stars appear to be a common, and perhaps universal property (Hartmann, 1998; Hartmann et al., 2016, see Figure 1.1 for a schematic of this process) that is thought to be responsible for the growth of mass towards the formation of the eventual star. A subsequent result of this is the ubiquitous presence of proto-stellar outflows and jets (see review by Bally, 2016). This is found to be a property in all astrophysical systems that are accreting via rotating, magnetised discs, from proto-stars to galactic nuclei. Such jets are thought to be driven by rotating magnetic fields in the inner accretion disk, and serve to remove angular momentum and energy from the system.

1.1.4 High-mass star formation

The physics of star formation and stellar feedback play a leading role in shaping the evolution of galaxies, and it is the most massive stars that provide a dominant source of feedback that drives the physical and chemical evolution of galactic material. To gain a complete understanding of how galaxies form and evolve across cosmic time, it is therefore essential that we understand how massive stars form and how they deposit their energy, momentum and chemically-enriched material into the interstellar medium. Currently, the formation mechanism of high-mass stars remains unconstrained, particularly for very massive stars.

Our understanding of late-O and early-B type star formation has progressed substan-

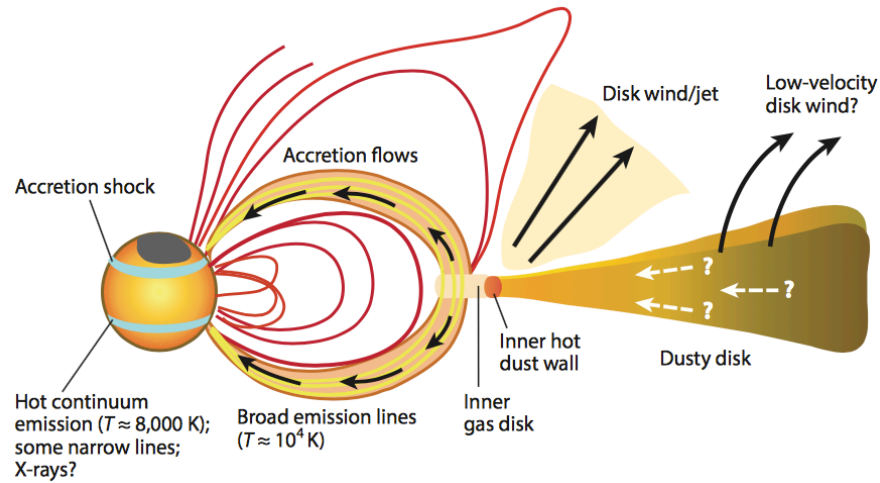


Figure 1.1: Schematic of the general view of low-mass proto-stellar accretion (Hartmann et al., 2016). The inner disc is truncated by the magnetic field. The intersection of the magnetic field and the inner disc channels the disc material on to the proto-star. The inner disc region drives bi-polar jets and proto-stellar winds.

tially over the last decade (see e.g. reviews by Zinnecker & Yorke, 2007; Tan et al., 2014). Many models seeking to explain the formation mechanism of high-mass stars exist, for example via accretion from cores (McKee & Tan, 2003; Krumholz et al., 2009; Kuiper et al., 2011), accretion from clouds/clumps (Bonnell et al., 2001), and via proto-stellar mergers (Bally & Zinnecker, 2005). The former two of these scenarios have been debated and explored extensively in the literature, and are often referred to as *core accretion* and *competitive accretion* models, respectively.

The defining feature of the *core accretion* model is that high-mass stars form within dense, massive and gravitationally bound pre-stellar cores, which themselves arise as a result of the fragmentation of their natal cloud in a scaled-up version of low-mass star formation (McKee & Tan, 2003). It is often also referred to as the *turbulent core* model, due to the work of McKee & Tan (2003), where they presented a model in which turbulent motions within the core are dominant. This high turbulence acts to provide support to the core and means that any cores that become unstable to gravitational collapse are very dense, and hence have high accretion rates. Though this model

manages to produce the high accretion rates required to form high-mass stars, it is not clear what the source of this turbulence should be. This condition also explicitly suggests that all high-mass stars must form in regions of high-turbulence. One of the other main problems with this scenario is in explaining why such massive, turbulent cores should not fragment into a sub-set of smaller pre-stellar cores. One mechanism that has been put forward to overcome this problem suggests that radiative feedback from nearby low-mass proto-stars suppresses fragmentation (Krumholz & McKee, 2008), though observations of high-mass cluster-forming regions suggest that this may require an unusually large population of low-mass stars to form initially (e.g. Longmore et al., 2011). It has also been argued that the presence strong magnetic fields (\sim mG) would be sufficient to halt fragmentation within the core (Tan et al., 2013). A key prediction of this scenario is that massive starless cores – the initial conditions of high-mass stars in this model – should exist. Despite many observations of high-mass star-forming regions, massive starless cores have not been unequivocally found, though potential candidates that warrant further investigation have been found (e.g. Cyganowski et al., 2014; Kong et al., 2017).

In contrast, the *competitive accretion* model predicts that high-mass stars begin their proto-stellar lives at more moderate masses, but continue to accrete material from the surrounding medium of the clump/cloud in which they are embedded. They would therefore never exist in a massive starless core phase. This scenario also predicts that the growing high-mass proto-star should be forming in a proto-cluster, in which it resides towards the centre and is surrounded by a population of low-mass proto-stars. This scenario reproduces the observational result that high-mass stars are often found in star clusters (e.g. Lada & Lada, 2003). However, there are also known cases of isolated high-mass stars (see e.g. Bressert et al., 2012a; Tremblay et al., 2015). It is possible that such stars may have been ejected from clusters due to N-body interactions, but if they truly formed in isolation, this presents a challenge for the *competitive accretion* scenario. Simulations show that massive stars can grow via accretion from their larger scale natal clumps, without ever existing in a massive pre-stellar phase, and that a population of lower mass stars form within the cluster simultaneously (e.g.

Smith et al., 2009). This has also been seen observationally, for example, Cyganowski et al. (2017) recently reported the detection of simultaneous low- and high-mass star formation in G11.92–0.61. However, this region also contains one of the best known massive starless core candidates (Cyganowski et al., 2014), suggesting that the reality of high-mass star formation is perhaps not so easily described by either one of these models in isolation.

Simulations of massive and compact cores suggest that in the case of *core accretion*, a core at an early evolutionary phase will be dominated by a central high-mass source and contain a few lower-mass fragments. The central source is expected to dominate the luminosity of the core and extend out to ~ 1000 AU. [See e.g. Krumholz et al. (2007a); here a simulated core of $M = 100 M_{\odot}$, $R = 0.1$ pc fragments into a central source of $M \sim 10 M_{\odot}$ and $R \sim 1000$ AU, along with 2 low-mass fragments of 0.05 and $1.2 M_{\odot}$.] Krumholz et al. (2007a) utilise mock ALMA observations to demonstrate that, in the case of ‘core accretion’, kinematic signatures of rotation can be detected and quantified on ~ 1000 AU scales using different dense gas tracers. The *competitive accretion* model, however, predicts that such a core would instead contain multiple lower-mass fragments and not be dominated by a single source. Here, the crowding of stars and competition for the surrounding material means that fragments are expected to be truncated to a few tens of AU (Bonnell et al. 2003).

Though these two ‘competing’ scenarios have been studied considerably, it is likely that the complex reality of high-mass star formation is not so clear-cut. Considerable efforts in the field are being led to further develop the theoretical and numerical frameworks, and compare these with high-resolution far-IR and (sub-)mm observations, which are effective in probing dust cores throughout the Galaxy on proto-stellar scales. However, these models remain largely untested in the most extreme mass regimes (up to and greater than $100 M_{\odot}$), and thus, despite their obvious cosmological importance, the formation mechanism of very high-mass stars remains a mystery.

One of the most challenging aspects of investigating the formation of the most massive stars is that they, and hence their progenitors, are extremely rare. Given a population of 10,000 stars sampled from a stellar IMF, we would expect to find only ~ 1 star that

is $> 100 M_{\odot}$. To better understand the initial conditions and formation mechanisms of such stars, it is essential that their precursors are discovered and studied in detail. But this inherent rarity means that it is difficult to find the progenitors to such stars.

1.1.5 Star clusters

Stars are known to commonly form in clustered environments (Lada & Lada, 2003), and stellar clusters can contribute substantially to the stellar population of a galaxy (see e.g. Goddard et al., 2010; Silva-Villa & Larsen, 2011; Kruijssen, 2012). Classically, they have been categorised into two distinct populations; globular clusters, which are old ($\gtrsim 10$ Gyr), massive ($\gtrsim 10^5 M_{\odot}$) and dense ($\gtrsim 10^3 M_{\odot} \text{ pc}^{-3}$) gravitationally bound stellar populations that formed in the early Universe, and open clusters, which are comparatively younger ($\lesssim 1$ Gyr), less massive ($\lesssim 10^3 M_{\odot}$), less dense ($\lesssim 10^3 M_{\odot} \text{ pc}^{-3}$) and not necessarily bound. More recently however, it has become apparent that young massive clusters (YMCs; defined by Portegies Zwart et al., 2010, to be gravitationally bound systems with $M \gtrsim 10^4 M_{\odot}$ and ages $\lesssim 100$ Myr), whose stellar masses and densities can reach and even exceed those of globular clusters, are still forming at the present day (e.g. Holtzman et al., 1992).

Clusters are extremely useful laboratories for testing our understanding of many astrophysical phenomena. The extreme stellar densities in massive clusters offers a unique insight into the earliest stages of star and planet formation and evolution in extremely dense environments, where feedback mechanisms and dynamical encounters are likely to affect their subsequent evolution significantly. High-mass stars are also often found in young stellar clusters. For example, Galactic clusters like the Arches and Quintuplet are seen to contain many high-mass stars, some of which even exceed $100 M_{\odot}$ (Figer et al., 1999a,b, 2002). This is likely a direct result of greater IMF sampling – in a cluster containing $> 10^4$ stars, it is statistically likely that there will be several hundred stars $> 10 M_{\odot}$ and a few extremely high-mass stars present. It may also be the case that if *competitive accretion* or *stellar collisions/mergers* are common modes of massive star formation, then this should be much more viable in dense, clustered

environments and would lead to a greater presence of high-mass stars in dense star clusters. It therefore follows that if we wish to identify and study the precursors to the most massive stars, we are more likely to find them residing in the precursors to the high-mass stellar clusters.

The most massive and dense clusters that are currently forming in the Galaxy are YMCs. Understanding how YMCs form is crucial in addressing the formation and evolution of stars, planets and clusters in the most extreme density regimes. The following section presents an overview of YMCs, their progenitors and potential formation mechanisms.

1.1.6 The formation of young massive clusters (YMCs)

The discovery that massive stellar clusters are still forming at the present day has reinvigorated the discussion of cluster formation mechanisms and spawned the idea that perhaps all clusters form in a similar way. Observations show that the cluster mass distribution is in fact continuous (Larsen, 2009; Portegies Zwart et al., 2010), extending from low-mass open clusters ($\sim 100 M_{\odot}$) to high-mass YMCs that are seen to be as massive as $\sim 10^8 M_{\odot}$ (e.g. W3 in NGC 7252, Maraston et al., 2004; Cabrera-Ziri et al., 2016). This has potentially important implications, suggesting that clusters form in a similar way across this entire mass range. Additionally, it has been proposed that high-mass YMCs may be local analogues to the old globular clusters that we see today (e.g. Elmegreen & Efremov, 1997; Kruijssen, 2014). In this scenario, only the clusters formed in the early Universe that belonged to the high-mass end of the continuum would have been able to survive for a Hubble-time, whereas the lower mass clusters would have been disrupted (e.g. Vesperini, 2001; Fall & Zhang, 2001; Kruijssen, 2015) and dissolved into the field population. If these scenarios are indeed true, this places YMCs in an important context – by understanding their formation and evolution, it may be possible to gain an insight into the formation of clusters across the full mass range, including that of globular clusters.

YMCs with ages greater than a few Myrs have been identified in significant numbers

(see the review by Portegies Zwart et al., 2010, and references therein), and particularly in galaxies with high star-formation rates (e.g. Whitmore, 2002). Several have also been identified within our own Galaxy, such as the Arches, Quintuplet, NGC 3603, Westerlund 1 and red super-giant (RSG) clusters (Figer et al., 1999c; Goss & Radhakrishnan, 1969; Clark et al., 2005; Davies et al., 2007).

The mechanism via which YMCs form is not yet entirely understood (see the review by Longmore et al. 2014b). Much of the relevant discussion in the literature debates the initial distribution of the stars in YMCs. There are two prominent theories on how stars are born in these clusters.

One scenario suggests that the stars form in a bound, centrally-condensed population in an extremely compact natal gas cloud. Feedback processes from the embedded stellar population then remove the remaining gas, decreasing the global gravitational potential and causing the cluster to expand towards its final, un-embedded phase (see e.g. Lada et al., 1984; Boily & Kroupa, 2003; Bastian & Goodwin, 2006; Baumgardt & Kroupa, 2007, and the recent review by Banerjee & Kroupa 2015). This is a *monolithic* formation scenario for YMCs.

The other scenario is one in which stars and sub-clusters form in accordance with the observed hierarchical structure of their natal gas clouds. Indeed, as outlined in section 1.1.1 of this chapter, the interstellar medium is known to be hierarchical and sub-structured (e.g. Larson, 1981; Elmegreen, 2008; Kruijssen, 2012). A heightened star formation efficiency (SFE) towards the densest peaks leads to gas exhaustion on local scales, causing stellar dynamics to eventually dominate (Kruijssen et al., 2012; Girichidis et al., 2012; Longmore et al., 2014b; Dale et al., 2015). The subsequent hierarchical merging of these stars and sub-clusters results in a centrally-concentrated, bound cluster (Fujii et al., 2012; Parker et al., 2014a). This is a *hierarchical* mode of YMC formation.

Note that the above scenarios can be confusing and can even co-exist. For example, Banerjee & Kroupa (2015) show that a cluster may form *monolithically* from an initially *hierarchical* distribution of stars, given an initial high density and prompt merg-

ing of sub-structure (< 1 Myr).

These ‘monolithic vs. hierarchical’ discussions on YMC formation also do not adequately address the density evolution of both the *gas and stars*. One main difference between these two scenarios is whether or not the stars are expanding or contracting after their immediate formation – i.e. *are the stars in YMCs born at initially higher or lower densities than their final gas-free distributions?* In order to address this, we need to study and compare the spatial distribution of the stars in YMCs with that of the gas in their gas-phase precursors. To date, there have been very few candidate YMC precursor gas clouds identified. In order to constrain possible formation mechanisms, it is essential that such clouds are found and studied in detail such that we can begin to understand the initial conditions of YMC formation.

It is expected that the gas-phase precursors to YMCs should be molecular clouds of order $10^5 M_{\odot}$, contained within several parsecs, such that a high-mass ($10^4 M_{\odot}$) and compact ($R_{core} \sim 0.1$ pc) cluster can form, given a star formation efficiency of $\lesssim 30\%$. Recent efforts to survey the Galactic plane at far-infrared and (sub)millimetre wavelengths, where these dense, cold clouds should emit brightly, have led to the identification of a growing sample of potential YMC precursor clouds throughout the Galaxy (see e.g. Longmore et al., 2013b, 2014a; Ginsburg et al., 2012, 2016a; Urquhart et al., 2013; Contreras et al., 2017). Fig. 1.2 displays the currently identified Galactic YMC precursors (Longmore et al., 2014a). All of the YMC precursor candidates that have been identified in the Galactic disc are seen to be forming stars at a high rate (e.g. W49, W51) and have therefore have lost much of their initial structure as a result of stellar feedback (note that Urquhart et al. (2013) explicitly searched for star-forming clouds). Whilst these clouds are of course important in understanding the YMC formation process, if we wish to probe the true initial conditions then we require clouds that have yet to initiate widespread star formation. Thus, in addition to the aforementioned criteria, we would then also expect such progenitor clouds to be cold ($T \sim 10 - 20$ K) and devoid of widespread star formation. Given that none of the identified progenitor clouds in the Galactic disc are quiescent, very little is known about the initial conditions from which these massive clusters form.

Longmore et al. (2012) recently identified a likely YMC precursor in the extreme molecular cloud G0.253+0.016 (see e.g. Lis et al., 1994; Lis & Menten, 1998; Longmore et al., 2012, 2013b; Kauffmann et al., 2013a; Rathborne et al., 2014a,b; Johnston et al., 2014), and determined that it is cold ($T_{dust} \sim 20 - 30$ K), high-mass ($M \sim 1.3 \times 10^5 M_{\odot}$), compact ($r \sim 2.8$ pc) and other than a single region of weak water-maser emission, exhibits little-to-no star forming activity – precisely the conditions one would expect of a dense cloud that could form a high-mass cluster. Longmore et al. (2013b) later identified three further potential YMC precursors in clouds known as ‘d’, ‘e’ and ‘f’. These clouds are all high-mass ($\sim 10^5 M_{\odot}$), compact (\sim pc-scale) and other than a region of methanol maser emission towards cloud ‘e’, are all quiescent (Immer et al., 2012). Along with G0.253+0.016, they are situated in the Central Molecular Zone (CMZ; inner ~ 500 pc of the Galaxy, Morris & Serabyn, 1996) and belong to the so-called ‘dust-ridge’ (Lis et al., 1999; Immer et al., 2012) towards the Galactic centre, which itself appears to belong to a coherent circumnuclear stream of gas that is orbiting the Galactic centre (Molinari et al., 2011; Kruijssen et al., 2015; Henshaw et al., 2016). The fact that four of the most massive, dense and quiescent molecular clouds known to exist in the Galaxy all lie at the same distance and reside within the same stream of gas is certainly very intriguing, but it also presents an opportunity to study a sample of potential YMC progenitor clouds under the same environmental conditions at similar sensitivity and resolution.

1.1.7 The environmental dependence of star formation

Star formation relations that describe the conversion of gas into stars provide the foundation for many astrophysical studies, from local to cosmological scales. As such, an end-to-end understanding of the star formation process as a function of environment is crucial if it is to be applied to the vastly differing conditions found throughout the Universe. To date, empirical star formation relations have largely been calibrated using detailed studies of star forming regions in the disc of our own and nearby galaxies. Using observations of nearby star-forming regions, Lada et al. (2010a) proposed a gas surface density threshold for star formation of $\sim 120 M_{\odot} \text{ pc}^{-2}$, above which stars

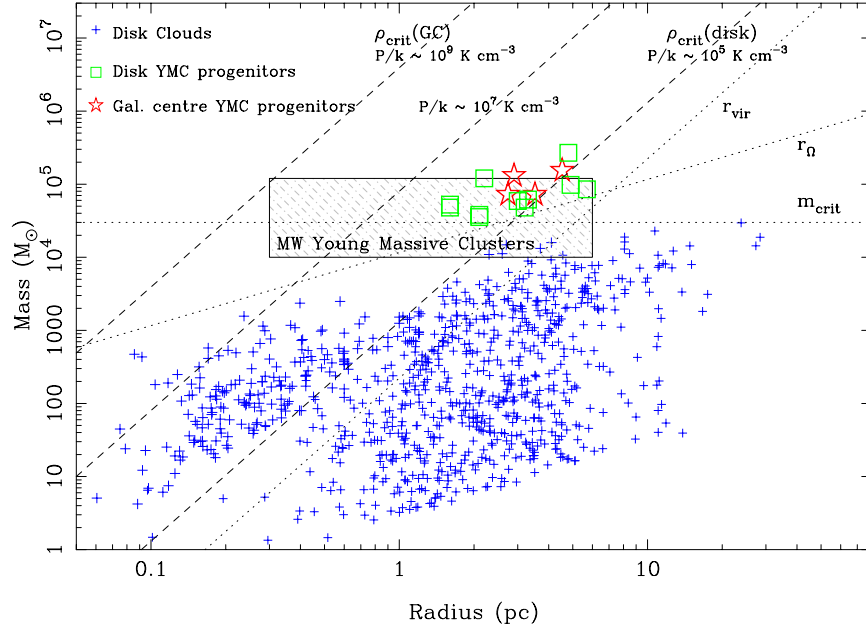


Figure 1.2: Mass vs. radius for Galactic gas clouds and YMCs. Gas clouds are shown as coloured symbols and the hatched rectangle shows the location of Galactic YMCs. Dashed lines show the predicted critical density threshold for star formation to occur under different environmental conditions. The dotted lines correspond to the criteria for YMC formation put forward by Bressert et al. (2012b) – a critical mass (m_{crit}) of $\sim 3 \times 10^4 M_{\odot}$, r_{Ω} is the radius for a given mass at which the escape velocity of the cloud is greater than the sound speed in ionised gas, and r_{vir} is the virial mass for a cloud crossing a time of 1 Myr. See Longmore et al. (2014a) for full details.

could form efficiently. This surface density threshold was argued to reflect an underlying volume density threshold of $\sim 10^4 \text{ cm}^{-3}$. This was later shown to hold true over a remarkably large range of masses (see Fig. 1.3; Lada et al., 2012). This empirical result suggests an underlying physical process, whereby the rate of star formation in molecular gas is simply determined by the amount of ‘dense gas’ that lies above the empirical threshold. Krumholz & McKee (2008) also propose a column density threshold of $\sim 1 \text{ g cm}^{-2}$ for the formation of high-mass stars. As discussed in §1.1.4, this threshold arises due to the fact that fragmentation to lower masses is predicted to become suppressed in clouds with $\Sigma > 1 \text{ g cm}^{-2}$ due to the radiative feedback from lower mass stars in the cloud that have high accretion luminosities. At these high densities (and hence, opacities), this radiation from low-mass stars will heat up the cloud, which will increase the Jeans mass (see Equation 1.5). One crucial assumption here is that low-mass stars must form before high-mass stars for this mechanism to occur. Long-

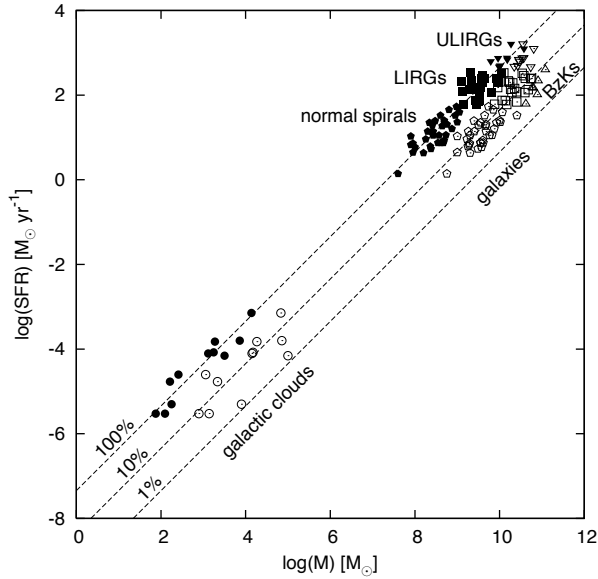


Figure 1.3: Star formation rate vs. molecular gas mass for local molecular clouds and galaxies. Solid symbols: cloud masses from extinction observations of galactic clouds and HCN observations of galaxies. Open symbols: total cloud masses of the same clouds and galaxies, from extinction measurements (clouds) and CO observations (galaxies). For the galaxies, pentagons are normal spirals, while starburst galaxies are represented by squares (LIRGs) and inverted triangles (ULIRGs). Triangles represent high- z BzK galaxies. Dashed lines indicate the percentage of gas that is above the empirical density threshold of $\sim 10^4 \text{ cm}^{-3}$. See Lada et al. (2012) for further details.

more et al. (2011) showed that, at least in the case of the proto-cluster G8.68–0.37, that this would require an unfeasibly large population of low-mass stars to have formed in order to sufficiently heat the gas and halt fragmentation.

To enable the appropriate application of relations such as these across cosmic history, it is critical that we understand how star formation is regulated by its environment down to the scales on which individual stars are forming. The most extreme conditions for star formation are in starburst galaxies at high redshift. However, it is impossible to study such sources in detail due to the technical limitations of current facilities, and regardless of future advances, we will always achieve higher resolution observations of nearby regions. Fortunately, at a comparatively close distance of $\sim 8.4 \text{ kpc}$ (Reid et al., 2009a, 2014), the Galactic centre is known to be extreme compared to the Solar neighbourhood, with densities, gas temperatures, pressures, cosmic ray ionisation rates and magnetic field strengths being several factors to orders of magnitude greater (Kruijssen & Longmore, 2013).

It has been shown that there is something different about the criteria under which stars form at the Galactic centre. Longmore et al. (2013a) showed that a significant fraction of the gas in the CMZ lies above a volume density of $\sim 10^4 \text{ cm}^{-3}$ – the threshold proposed by Lada et al. (2010a). Despite this, they found that the star formation rate

(SFR) in the CMZ is 1 – 2 orders of magnitude lower than predicted in this model. The current understanding of this discrepant SFR is that the CMZ undergoes an episodic cycle and is currently at a low point due to the high turbulent energy density there (Kruijssen et al., 2014), as evidenced by the comparatively large line-widths of $\sim 10 - 20 \text{ km s}^{-1}$ seen in the gas in the CMZ (Henshaw et al., 2016). This high turbulence will act to drive up the critical volume density threshold for star formation (Krumholz & McKee, 2005; Padoan & Nordlund, 2011). High-resolution observations of the CMZ molecular cloud G0.253+0.016 with the Submillimeter Array (SMA) and the Atacama Large Millimeter/submillimeter Array (ALMA) show that the internal density structure of the cloud is consistent with a log-normal distribution that is well described by turbulent cloud models (Johnston et al., 2014; Rathborne et al., 2014b). This difference in star-forming activity highlights that this single volume density threshold for star formation may not hold in the more extreme environment of the Galactic centre, and this has recently also been found to be true in the centres of other galaxies (Usero et al., 2015; Bigiel et al., 2016).

These results are all consistent with the idea that the process of star formation may proceed differently in environments that are significantly different from those in Milky Way-like discs. The extreme conditions therefore make the CMZ an ideal laboratory to test to what extent our understanding of star formation from the limited range of conditions seen in the Galactic disc still applies, and how it can be extended. Additionally, the conditions of the gas in the Galactic centre are similar to those in high-redshift star-forming galaxies (Kruijssen & Longmore, 2013). Given that the peak epoch of star formation in the Universe occurred at redshifts of $\sim 2-3$ (Hopkins & Beacom, 2006; Madau & Dickinson, 2014), this places studies of the Galactic centre in an important cosmological context – understanding how stars form here can provide insight into how stars may have formed in the early Universe.

1.2 The Central Molecular Zone – a laboratory for understanding extreme star formation

Despite the seemingly low SFR in the CMZ, there are regions of substantial star formation and stellar content. The star forming Sagittarius B2 complex is one of the most active sites of (high-mass) star formation in the Galaxy, hosting dense clusters of H_{II} regions and dust cores (e.g. Gaume et al., 1995; Qin et al., 2011). There are also two YMCs – the Arches and Quintuplet – which have formed in the CMZ recently, with ages of ~ 3.5 and 4.8 Myr, respectively (Schneider et al., 2014). These clusters contain $> 10^4 M_{\odot}$ of stars, making them amongst the most massive clusters to have recently formed in the Galaxy (Portegies Zwart et al., 2010), with the Arches being the most dense young cluster known in the Galaxy, with central stellar densities of $\sim 2 \times 10^5 M_{\odot} \text{pc}^{-3}$ (Espinoza et al., 2009).

Searching for the precursors to clusters like the Arches and Quintuplet, which contain tens of thousands of stars, allows us to study the how these stars form in this extreme environment. Sagittarius B2 is a likely candidate for such a precursor system. However, the intense ionising radiation from the forming high-mass stars has disrupted the initial gas conditions.

As noted in §1.1.6, the CMZ hosts several quiescent molecular clouds that have been identified as potential precursors to YMCs. These clouds are confined to a relatively small region, which is situated in a gas stream spanning ~ 37 pc in projection. This region, known as the ‘dust ridge’ (Lis et al., 1999), contains 6 prominent infrared dark clouds. These are G0.253+0.016 (aka ‘the Brick’), G0.340+0.055, G0.380+0.050, G0.412+0.052, G0.478–0.005 and G0.496+0.020. For the sake of brevity, the nomenclature of Lis et al. (1999) is adopted and these clouds are hereafter referred to as ‘a – f’, respectively. Of these, four clouds, ‘a’, ‘d’, ‘e’ and ‘f’ have been identified as potential progenitors to YMCs (Longmore et al., 2013b; Rathborne et al., 2015). Clouds ‘b’ and ‘c’, whilst not massive enough to be considered YMC precursors, still contain tens of thousands of solar masses of gas and dust within only

a few parsecs (Immer et al., 2012) and therefore still have the potential to form substantial star clusters. Given that a significant number of high-mass stars are expected to be found in massive stellar clusters (inferred statistically via IMF sampling), these dust-ridge clouds provide an excellent laboratory in which to probe the early, largely unperturbed conditions of both massive star and cluster formation in the extreme environment of the CMZ.

1.3 Goals of this work

The following chapters of this thesis present the results of the research that I have undertaken in an effort to tackle some of the outstanding unsolved problems in the field of star formation. Using the Galactic centre dust ridge clouds as a template for understanding the early stages of star and cluster formation in the CMZ, this research aims primarily to address the following questions –

- (i) Are the global properties of the dust ridge clouds consistent with those expected of a cloud with the potential to form a $> 10^4 M_{\odot}$ stellar cluster?
- (ii) If these dust ridge clouds represent the initial conditions of YMC formation, how does the distribution of mass in the clouds compare with the distribution of mass in the intermediate and final stages of YMC formation? And can this comparison inform our understanding of the mechanism(s) via which YMCs may form?
- (iii) Do the properties of YMCs and their progenitors vary as a function of Galactic environment?
- (iv) Do the dust ridge clouds currently display dense structure on small spatial scales (i.e. pre/proto-stellar cores)? And if so, are any of these cores likely to be the precursors to high-mass stars?
- (v) If the dust ridge clouds do harbour the initial conditions for high-mass star formation, how do the properties of the cores compare to those in other regions of the Galaxy?

1.4 Observing techniques: from far-IR to radio telescopes

The aforementioned goals of the work presented in this thesis are achieved through using a variety of observations. From archival to newly-acquired data, these observations consist of a combination of large-scale surveys and detailed observations of specific targets, from space- and ground-based single-dish telescopes and ground-based radio/sub-mm interferometers. Together, these observations provide a multi-wavelength, multi-scale view of molecular clouds, from giant complexes that span many 10s of parsecs, down to individual sites of star formation. This section presents a brief overview of the techniques and advantages/disadvantages of these different types of observations, with a specific focus on the technical differences between the facilities used in this thesis (e.g. Herschel, CSO, APEX, SMA and ALMA).

1.4.1 Receivers: detecting long-wavelength light

The most common types of receivers that are used to detect light in far-IR/sub-mm/radio astronomy ($\sim 30 \mu\text{m}$ to $> 1 \text{ m}$, hereafter referred to simply as ‘radio astronomy’, for brevity) are bolometer and heterodyne receivers. Each have their own specific uses and advantages, which are discussed in the following sections.

Bolometers

Bolometer receivers are incoherent detectors – their response is directly related to the intensity of incoming radiation. Incident photons generate heat in the absorbing material, which leads to a temperature increase that is directly proportional to the absorbed

radiation via $\Delta T = E/C$, where E is the energy of the radiation and C is the capacitance of the material. In practice, this is measured via a change in the voltage due to the temperature increase changing the resistance in the material. The absorber is connected via a weak thermal link (i.e. low conductance) to a heat sink. This ensures that the temperature increase of the absorber decays as it is transferred to the heat sink, with a characteristic decay time-scale of $\tau = C/G$, where G is the thermal conductance.

Bolometers have large bandwidths, resulting in very high sensitivity. Though they are broad-band receivers, it is possible to do pseudo-spectroscopy with bolometers that are fitted with filters. As they measure thermal response in the receiving material, bolometers must be cooled to very low temperatures ($\ll 1$ K). Such low temperatures are required as bolometers are often used to observe at sub-mm wavelengths, which corresponds to the peak of the SED at low temperatures of ~ 1 -50 K.

Until relatively recently, bolometers were single element detectors. This meant that imaging a single science target was very time consuming as the detector would have to mosaic single-pixel observations. Thankfully, this has since been overcome with the production of multi-element arrays. Examples of bolometer arrays that were used to take data used in this thesis are Submillimetre Common-User Bolometer Array (SCUBA 1&2) on the James Clerk Maxwell Telescope (JCMT), BOLOCAM on the Caltech Submillimeter Observatory (CSO) and the Photoconductor Array Camera and Spectrometer (PACS) and Spectral and Photometric Imaging Receiver (SPIRE) instruments on-board the Herschel Space Observatory.

Heterodyne receivers

Heterodyne receivers are relatively complicated compared to bolometers. They are coherent detectors, meaning that they preserve both the intensity and the phase of incoming radiation. The defining aspect of these receivers is that they utilise frequency mixing to convert the frequency of incoming waves to an intermediate frequency (IF), while maintaining the characteristics of the signal (i.e. heterodyning). The detected

signal is mixed with the IF which is driven by a local oscillator (LO). This is a technique that is applied widely in the radio domain, as it allows hardware to be built and optimised to handle specific frequencies rather than having to deal with a broad range of frequencies. Typically the signal frequency is down-converted, as lower frequencies are easier to handle from a hardware perspective, and so the performance of components is better and the cost is lower. The signal is also amplified in the receiver. Depending on the exact design of the receiver, this amplification may occur before or after mixing, or at multiple stages throughout the signal processing.

The mixing and processing of signals in heterodyne receivers depends on many factors, including the desired output, the performance of the hardware and the cost. One of the crucial design elements is ensuring that only the desired observing frequency is processed and output. While it is relatively simple to filter out only the chosen IF after mixing, care must be taken to also filter out specific frequencies prior to mixing that, while not at the observing frequency, can still produce signals at the IF as a result of mixing with the LO. This occurs as the mixing process creates higher-order terms, and given the right mix of input frequency and LO frequency, these higher-order products may be at the desired IF and must therefore be identified and filtered out before mixing to ensure that they don't end up contaminating the output signal.

The first-order products from the mixing of the observed frequency result in the lower and upper sidebands, which are centred on $\nu_{obs} - \nu_{LO}$ (USB) and $\nu_{LO} - \nu_{obs}$ (LSB), and will have a specific bandwidth about these central frequencies. Depending on the hardware and/or science goals, these sidebands can be handled in different ways. Single sideband modes filter out one of the sidebands, double sideband modes process both bands and superimpose them at the IF, and separate sideband modes process both bands but instead of superimposing at a single IF, the sidebands are output at separate IFs.

Heterodyne receivers are widely used in radio and sub-mm astronomy. Their ability to achieve both large bandwidth and high spectral resolution means that they are excellent detectors for continuum and spectral line observations. They are also used for interferometry, as their ability to preserve the phase of the detected radiation is crucial for

correlating signals detected by multiple antennae. Examples of telescopes used in this thesis that use heterodyne receivers are the Submillimeter Array (SMA), the Atacama Pathfinder EXperiment (APEX) and the Atacama Large Millimeter/submillimeter Array (ALMA).

Interferometry

At the long wavelengths of radio and sub-mm observations, we can peer into the cold and dense molecular clouds that harbour the initial conditions for star formation. However, observing at these long wavelengths comes with the drawback that large diameter telescopes (dishes) are required to achieve high angular resolution ($\theta \approx \lambda/D$, where θ is the angular resolution, λ is the wavelength and D is the dish diameter). Consequently, radio telescopes would have to be unfeasibly large to achieve very high angular resolution (e.g. $< 1''$) in the radio–sub-mm regime.

To overcome this limiting factor of dish diameter, the techniques of interferometry and aperture synthesis have been used extensively in radio and sub-mm astronomy to achieve extremely high angular resolution imaging. Interferometry involves using an array of multiple telescopes with coherent detectors. In the specific context of radio astronomy, this is an array of dishes/antennae with heterodyne receivers. The signals from the receivers are correlated in phase to effectively achieve the resolving power of a telescope with a diameter equal to that of the longest baseline within the array (i.e. $\theta \approx \lambda/B$, where B is the longest baseline). As the array elements will be physically separated and the incoming radiation will often be at some angle to the zenith, the radio signals will arrive at different elements with a delay. This is corrected for by an electronically-induced delay, which ensures that the signals from a given baseline are correlated in phase. This technique of correlating and combining the signals from an array of antennae is called aperture synthesis.

Interferometers therefore allow us to probe very small spatial scales at long wavelengths, without having to build extremely large dishes. However, there are significant

limitations of this technique, the most notable of which is the inherent limited recovery of flux as a function of angular scale. This is due to the fact that the interferometer can only sample angular scales that correspond to the projected distances of the baselines in the array. Longer baselines are sensitive to smaller angular scales, and shorter baselines are sensitive to larger spatial scales. The latter of these is problematic for interferometers, as the shortest baselines possible are limited by the diameter of the dishes, where it is necessary to ensure that the dishes are free to move and won't cast a shadow in front of other dishes. This ultimately means that large angular scales are not well recovered by interferometers. This problem is solved by combining interferometric data with the appropriate single-dish or compact array data. For example, ALMA has three main antenna facilities – a 12 m array, a 7 m array and a several 12 m single dishes (total power). This means that when used together, the 12 m array can be very extended and sample small angular scales, while the 7 m array can be in a compact configuration to recover intermediate angular scales, and the total power dishes can be used to recover the large scale (zero spacing) emission. The main interferometers used for the work in this thesis are the SMA and ALMA. Single-dish data from Herschel, CSO and APEX are utilised for combination with the interferometric data to recover the large-scale emission.

Chapter 2

Comparing young massive clusters and their gas-phase progenitors in the extreme environment of the Central Molecular Zone

Preface

The work presented in this chapter is based upon that of Walker et al. (2015). I led this work as first author, and all of the contents (text, analyses, figures, tables) are my own.

2.1 Introduction

The work in this chapter extends the analysis of Longmore et al. (2012) (L12, hereafter) of G0.253+0.016, in which they conclude that this dust ridge cloud is likely a precursor to a high-mass stellar cluster, to include dust ridge clouds ‘d’, ‘e’ and ‘f’.

Continuum data from the Herschel infrared Galactic Plane Survey (HiGAL, Molinari et al., 2010) are used to measure their global physical properties such as mass, radius and temperature. HiGAL is a Galactic plane survey conducted with the Herschel Space Observatory, covering the entire Galactic plane between $|b| < 1^\circ$. The survey observed the dust continuum emission of this region in five separate bands – 70 μm and 160 μm (observed with the PACS instrument, Poglitsch et al. 2010) and 250 μm , 350 μm and 500 μm (observed with the SPIRE instrument, Griffin et al. 2010). This wavelength range of 70 – 500 μm was targeted specifically to cover the peak of the spectral energy distribution (SED) of cold dust emission ($T \lesssim 50$ K). Sampling the SED in this way enables estimation of cloud temperatures and column densities, which when combined with distances estimates allows for mass determination (see next section). The angular resolution of the survey is variable as a function of wavelength, yielding beam-sizes of $\sim [6, 12, 18, 24, 35]''$ for $\lambda = [70, 160, 250, 350, 500] \mu\text{m}$.

Spectral line data from the Millimetre Astronomy Legacy Team 90 GHz Survey (MALT 90, Foster et al., 2011, 2013; Jackson et al., 2013) are used to measure the global kinematic properties of these clouds. The MALT90 survey provides spectral line data for 16 lines in the 90 GHz band. The data cubes for these transitions consist of 4096 channels with 0.11 km s^{-1} velocity resolution. Analysis of these data reveals that these clouds – the most massive and dense quiescent clouds known in our Galaxy – have the potential to form YMCs. Having shown that they are indeed candidate YMC precursors, they are then compared to more evolved (proto)-YMCs to speculate how gas is converted to stars on large scales in the early stages of YMC formation.

2.2 Results

2.2.1 Dust Column Densities & Temperatures

Figure 2.1 (*upper panel*) shows the HiGAL column density map of the ‘dust-ridge’ at the Galactic centre. The bottom panel displays the HiGAL temperature map of the same region. These maps were generated by Cara Battersby, utilising the methods

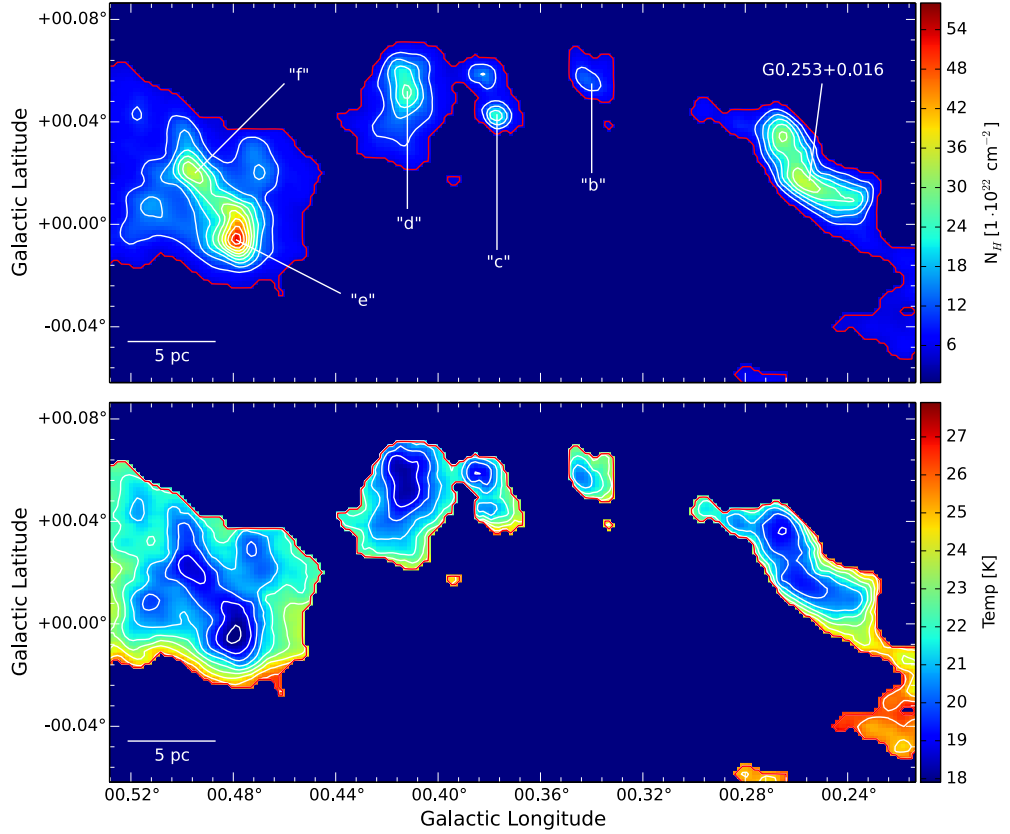


Figure 2.1: *Top*: Masked column density map of the dust ridge, derived from HiGAL far-IR continuum observations (Battersby et al., 2011). A column density threshold of $5 \times 10^{22} \text{ cm}^{-2}$ (red contours) is implemented and contours (white) are at 10, 15 ... $55 \times 10^{22} \text{ cm}^{-2}$. *Bottom*: Masked temperature map of the ‘dust-ridge’, derived from HiGAL far-IR continuum observations (for the techniques used to derive these maps, see Battersby et al., 2011). Contours (white) are at 17, 18 ... 27 K (systematic uncertainties in SED fitting are $\sim 3\text{--}4$ K). To display the correlation between dust column density and temperature, the same pixels as in the *top* image are masked here. Clearly seen in all of the clumps is an anti-correlation between column density and temperature of the dust – consistent with them being centrally condensed with cold interiors (e.g. Longmore et al., 2012).

outlined in Battersby et al. (2011) (the reader is referred to this paper for an in-depth discussion of how these maps were produced). The maps from the different wavebands are first projected on to the same grid, to ensure that they all have equivalent pixel scales and angular resolution. The maps displayed here have a pixel size of $\sim 5.5''$ and resolution of $25''$, or 0.2 pc and 1 pc, respectively, at the distance of these clouds, which is taken to be ~ 8.4 kpc (Reid et al., 2009a, 2014). Modified blackbody fits are then performed to estimate the column densities and temperatures within the map. For the production of the $25''$ map, the $500 \mu\text{m}$ data are not used, as they are lower resolution ($35''$). The $70 \mu\text{m}$ data are also not used, as the assumption that the emission is optically thin is unlikely to be justified at this wavelength. In terms of unconstrained observational parameters, the modified blackbody fits are dependent upon both the dust temperature and the optical depth, which itself depends on the column density and the dust opacity:

$$S_\nu = \frac{2h\nu^3}{c^2(e^{\frac{h\nu}{kT}} - 1)}(1 - e^{-\tau_\nu}) \quad (2.1)$$

where

$$\tau_\nu = \mu_{\text{H}_2} m_{\text{H}} \kappa_\nu N(\text{H}_2) \quad (2.2)$$

and

$$\kappa_\nu = \kappa_0 \left(\frac{\nu}{\nu_0} \right)^\beta \quad (2.3)$$

where h is the Planck constant, ν is frequency, c is the speed of light in vacuum, k is the Boltzmann constant, T is the dust temperature, τ_ν is the optical depth, μ_{H_2} is the mean molecular weight, m_{H} is the Hydrogen mass, κ_ν is the dust opacity, $N(\text{H}_2)$ is the H_2 column density and β is the spectral index.

Battersby et al. (2011) use the models of Ossenkopf & Henning (1994) to estimate $\kappa_0 \sim 0.04 \text{ cm}^2 \text{ g}^{-1}$, for $\nu_0 = 505 \text{ GHz}$ and a fixed β of 1.75. With these values fixed, the

only unknowns in the previous equations are the dust temperature (T) and the column density ($N(\text{H}_2)$). The modified blackbody fits leave the temperature and column density as free parameters, and return the best fit values on a pixel-by-pixel basis. While the parameter fits are good, there are some important limitations. A significant source of potential error is that the background emission in the radiative transfer equation ($I_\nu(0)e^{-\tau_\nu}$; see Eq. 1.1 in §1.1.1) is not accounted for. This is a more serious problem in regions of strong IR background emission, such as the Galactic centre clouds that are being studied here. The fixed value of β is also important – Battersby et al. (2011) show that ranging β from 1.5 to 2.0 can lead to temperature variations of up to ~ 4 K.

For the column density maps used in this chapter for the Galactic centre dust ridge clouds, a column density threshold has been applied such that all pixels below $5 \times 10^{22} \text{ cm}^{-2}$ are masked. This threshold is chosen as it highlights the spatial extent of the dense clumps well, whilst effectively masking the more diffuse emission across the region. G0.253+0.016, ‘d’, ‘e’ and ‘f’ have peak column densities ranging from $2.6 - 5.3 \times 10^{23} \text{ cm}^{-2}$ and central temperatures ranging 17 – 19 K. Overall, the maps clearly display an anti-correlation between the column density and temperature of the dust in every cloud – consistent with them being centrally condensed with cold interiors. The central temperature of cloud ‘c’ is slightly higher than might be expected given its central column density – at 22 K it is ~ 4 K warmer in its core than the other clouds, despite all being at similar column densities. This may be due to the fact that this cloud is likely forming high-mass stars that heat the cloud’s interior, as evidenced by water and methanol maser emission (Forster & Caswell, 1999a; Caswell et al., 2010a). It is interesting to note the discrepancy between the gas and dust temperatures at the Galactic centre. The gas temperature towards the Galactic centre has been shown to range from 50 K to in excess of 300 K (e.g. Ao et al., 2013; Johnston et al., 2014; Ginsburg et al., 2016b; Immer et al., 2016). This is significantly higher than the low dust temperatures of ~ 20 K, suggesting that the gas is being heated by some non-photon driven mechanism such as cosmic ray heating or turbulent energy dissipation (e.g. Ginsburg et al., 2016b).

2.2.2 Dust Mass

These column density maps are used to estimate the dust masses of the clouds, by assuming a mean molecular weight of $2.8m_H$ (where m_H is equivalent to the proton mass, 1.67×10^{-27} kg), multiplying each pixel by its physical area (assuming a distance of 8.4 kpc) and summing over the cloud area. For G0.253+0.016 and cloud ‘d’, this is straightforward given a visually-defined column density threshold of $5 \times 10^{22} \text{ cm}^{-2}$. However, clouds ‘e’ and ‘f’ are not entirely distinct, are embedded in a higher density region that lies above this threshold, and have two nearby distinct clumps at different velocities. Any kinematically distinct emission (identified using MALT90 data; see §2.2.4) is therefore masked to determine the masses of clouds ‘e’ and ‘f’. The masses of G0.253+0.016, ‘d’, ‘e’ and ‘f’ are estimated to be $11.9 \times 10^4 M_\odot$, $7.6 \times 10^4 M_\odot$, $11.2 \times 10^4 M_\odot$ and $7.3 \times 10^4 M_\odot$, respectively (see Table 2.1).

Note that these mass estimates are necessarily uncertain due to the ambiguity involved in defining a distinct cloud area, particularly in a contiguous region such as this. This effect is quantified in Figure 2.2, which shows how the estimated masses decrease as the column density threshold that is used to define the cloud is increased. Increasing the threshold from $5 - 10 \times 10^{22} \text{ cm}^{-2}$ decreases the mass estimates by approximately 20% for G0.253+0.016, 40% for cloud ‘d’, 10% for cloud ‘e’ and 15% for cloud ‘f’. Given the systematic uncertainties in estimating dense gas mass towards the Galactic centre of a factor of ~ 2 (Longmore et al., 2013a), any uncertainty in these mass estimates is dominated by systematics rather than the threshold used. These estimates agree well with those found by Immer et al. (2012) and L12. Note that the slight ($<10\%$) discrepancy between L12’s mass estimate for G0.253+0.016 and the one given here is simply due to a slightly different column density threshold being used to define the cloud.

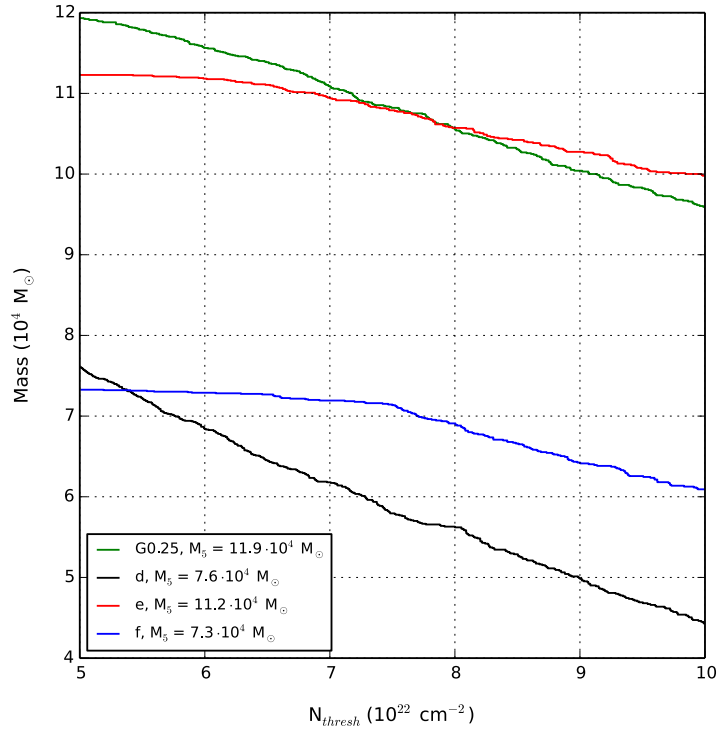


Figure 2.2: Mass as a function of column density threshold for clouds G0.253+0.016 (green), ‘d’ (black), ‘e’ (red) and ‘f’ (blue). The mass of clouds ‘d’, ‘e’, ‘f’ and G0.253+0.016 changes by $\sim 40\%$, 10% , 10% and 15% over this range, respectively.

2.2.3 Radius

Defining characteristic cloud radii is further complicated by their non-spherical geometry. The geometric mean of the minor and major axes of each cloud is measured to derive effective radii, where cloud boundaries are defined by the aforementioned column density threshold. Radii of 2.9 pc, 3.2 pc, 2.4 pc and 2.0 pc are determined for G0.253+0.016, ‘d’, ‘e’ and ‘f’, respectively.

To quantify how compact these clouds are, a characteristic radius within which $5 \times 10^4 M_{\odot}$ is enclosed is determined for each cloud. This mass is chosen as all four clouds exceed this mass and it is large enough that a $10^4 M_{\odot}$ cluster could form from it, given a star formation efficiency as low as 20%. Figure 2.3 displays this mass-radius relation for the four clouds and black dashed lines indicate their characteristic radii – 1.0 pc, 1.12 pc, 0.78 pc and 1.0 pc, respectively for G0.253+0.016, ‘d’, ‘e’ and ‘f’. This highlights the extreme nature of these clouds in that they harbour enough mass to form a YMC within a radius of ~ 1 pc and yet they do not show any signs of high-mass star

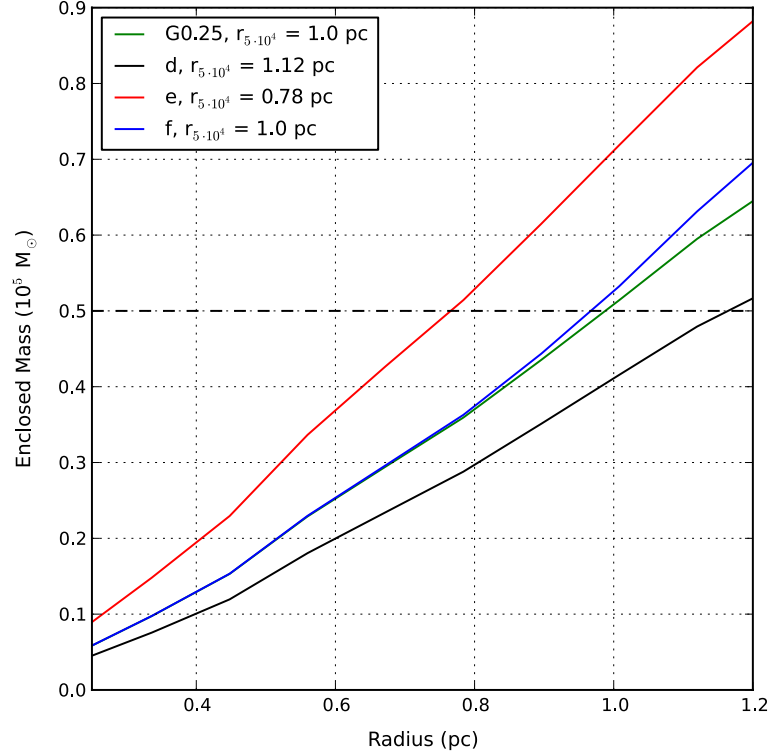


Figure 2.3: Enclosed mass as a function of radius for G0.253+0.016 (green), ‘d’ (black), ‘e’ (red) and ‘f’ (blue). The legend gives the radii within which $5 \times 10^4 M_{\odot}$ are enclosed.

formation other than that inferred by the detection of maser emission in G0.253+0.016 and cloud ‘e’.

Using the data plotted in Figure 2.3, one can determine the underlying volume density distribution that would be required to generate these mass profiles. As these profiles correspond to the projected mass, 3D models of the density distribution must first be constructed, and then projected into 2D. Under the assumption of spherical symmetry, we constructed 3D spherical distributions according to $\rho = \rho_0 R^{-a}$, where ρ is the density, ρ_0 is a constant that represents the central density, R is the radius, and a is the slope of the volume density profile. This 3D distribution is then collapsed into 2D by summing along the third axis, to generate a projected density distribution. This distribution is then summed up in increasingly large circular apertures to yield cumulative mass profiles in the same way as for the real data of the dust ridge clouds. This was performed for a range of 3D models, each with different values of the slope, a .

Through comparing the resultant mass profiles with those of the real data, we determine that the underlying volume density distributions of the clouds are best described by a slope of $a \sim 1.8$. However, at larger radii, the mass profile begins to turn over to an eventual plateau, and so the density profile of the whole cloud is not well described by a simple power-law relation. It is important to note that the assumption of spherical symmetry is likely a vast oversimplification, but a justifiable one given that the three dimensional geometries of these clouds are not known.

2.2.4 Gas Velocity Dispersion

Molecular line emission is used to characterise the global kinematics of these clouds and assess their dynamical state. Any line analysis is complicated due to their location in the CMZ, where the kinematic and chemical structure is known to be complex – with large velocity dispersions, shock-enhanced chemistry and confusion due to unrelated line-of-sight emission within the Galactic disc. It is therefore important to ensure that sensible molecular tracers are chosen to isolate the emission from each cloud.

The MALT90 survey provides data cubes for 15 different molecular tracers, probing a range of critical densities and excitation energies. Across clouds ‘d’, ‘e’ and ‘f’, emission from 11 of the 15 tracers is well detected. The same categorisation as Rathborne et al. (2014a) is adopted here, separating these detected molecular transitions as: *optically thick tracers* – HCN (1–0), HNC (1–0), HCO⁺ (1–0) and N₂H⁺ (1–0); *optically thin tracers* – HN¹³C (1–0), H¹³CO⁺ (1–0) and ¹³CS (2–1) and *‘hot core’/shock tracers* – HNCO 4(0,4)–3(0,3), SiO (1–0), HC₃N (10–9) and CH₃CN 5(0)–4(0). As might be expected of clouds in the turbulent environment of the CMZ, it is found that their kinematics are complicated. The data cubes show complex line profiles, significant velocity gradients, multiple velocity components, large line-widths and intense shock-associated emission lines. Detailed analysis of these features, along with the full suite of detected line emission, is deferred to future work. (See Rathborne et al. (2014a) for an in-depth discussion regarding the molecular line emission from G0.253+0.016).

This work requires only estimates of the line-widths for each cloud. Of the detected

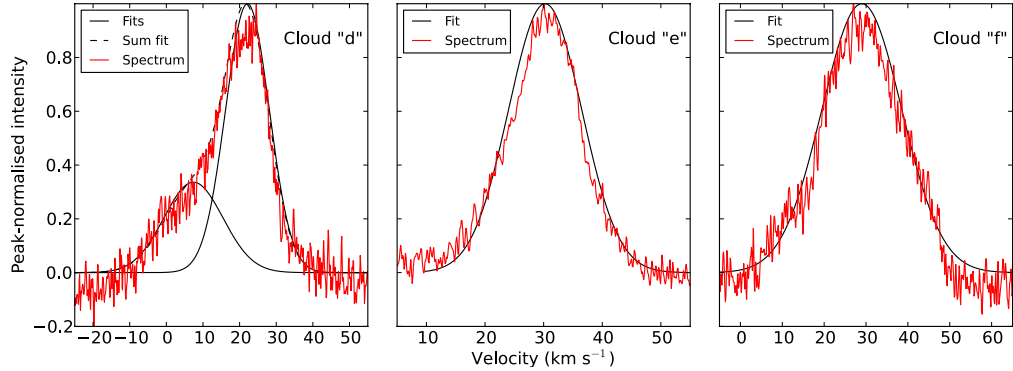


Figure 2.4: Hanning-smoothed, spatially-averaged HNC O line profiles for clouds ‘d’ [left], ‘e’ [centre] and ‘f’ [right]. Each is fitted using the multi-component Gaussian-fitting in the CASA software package. In the profile for cloud ‘d’, the component at $\sim 7 \text{ km s}^{-1}$ is attributed to emission from unrelated emission along the line of sight (see Figure 2.5). In cloud ‘f’ the line profile is very broad. This may be the true line-width in the cloud, however it is possible that it is broadened by emission from outside of what we are considering to be the cloud area (see Figure 2.5 for integrated intensity maps at different velocities). Fitting the components associated with the clouds yields the following peak velocity and line-width estimates: cloud **d**: $V_{LSR} = 22.1 \pm 0.3 \text{ km s}^{-1}$, $\Delta V = 14.1 \pm 0.5 \text{ km s}^{-1}$; cloud **e**: $V_{LSR} = 29.3 \pm 0.1 \text{ km s}^{-1}$, $\Delta V = 14.9 \pm 0.1 \text{ km s}^{-1}$; cloud **f**: $V_{LSR} = 29.0 \pm 0.1 \text{ km s}^{-1}$, $\Delta V = 22.5 \pm 0.2 \text{ km s}^{-1}$.

lines, the HNC O 4(0,4)–3(0,3) line emission is chosen to trace the underlying kinematics of the clouds. While it is not certain that this should be an optically thin line, it has been shown to reliably trace the kinematics across the entire CMZ (Henshaw et al., 2016). It is also detected with very high signal-to-noise in all of the dust-ridge clouds, and indeed the CMZ as a whole. Figure 2.4 shows Hanning-smoothed HNC O spectra that have been averaged over the spatial extent of the clouds (defined by the $5 \times 10^{22} \text{ cm}^{-2}$ column density threshold, see Figure 2.1), where each profile is fitted using the CASA software package (McMullin et al., 2007). Cloud ‘d’ (*left panel*) displays two velocity components, one at $\sim 7 \text{ km s}^{-1}$ and another at $\sim 22 \text{ km s}^{-1}$. Only the 22 km s^{-1} component is attributed to the cloud itself, as the morphology of the molecular line emission corresponds to the dust emission well. The 7 km s^{-1} component arises from an unrelated cloud along the line of sight (see Figure 2.5). The fit to the associated component yields a peak velocity and line-width (FWHM) of $V_{LSR} = 22.1 \pm 0.3 \text{ km s}^{-1}$ and $\Delta V = 14.1 \pm 0.5 \text{ km s}^{-1}$. Cloud ‘e’ (*middle panel*) shows a clear singular component with $V_{LSR} = 29.3 \pm 0.1 \text{ km s}^{-1}$ and $\Delta V = 14.9 \pm 0.1 \text{ km s}^{-1}$.

Cloud ‘f’ (*right panel*) also shows a single velocity component. This component has a peak velocity and line-width of $V_{LSR} = 29.0 \pm 0.1 \text{ km s}^{-1}$ and $\Delta V = 22.5 \pm 0.2 \text{ km s}^{-1}$. This line-width is significantly broader than in the two other clouds. Though this may well be the true line-width, it is noted that there is significant emission at lower velocities that peaks towards one of the nearby clumps in this cloud complex. It is therefore possible that this line may be broadened by this nearby emission. Coupling these results with L12’s results for G0.253+0.016: $V_{LSR} = 36.1 \pm 0.4 \text{ km s}^{-1}$, $\Delta V = 15.1 \pm 1.0 \text{ km s}^{-1}$, it is clear that all four clouds, whilst having slightly different peak velocities, have very similar line-widths of $\sim 16 \text{ km s}^{-1}$, with the possible exception of cloud ‘f’, which is a few km s^{-1} broader.

2.2.5 Virial masses

To investigate the cluster-forming potential of these clouds, it must first be determined whether they are gravitationally bound. This is done by estimating and comparing their dust and virial masses to estimate the virial ratio. Taking the radii and line-width estimates and assuming a spherical density distribution, the following equation is used to estimate the virial ratio:

$$\alpha = k \frac{\sigma^2 R}{GM} \quad (2.4)$$

where $\sigma = \Delta V/2\sqrt{2\ln(2)}$, ΔV is the line-width, R is the radius, G is the gravitational constant, M is the mass, and $k = (5 - 2a)/(3 - a)$ is a constant that relates to the volume density profile (e.g MacLaren et al., 1988), where a is the slope in the relation $\rho \propto R^{-a}$ (see § 2.2.3). $\alpha \lesssim 2$ typically indicates gravitationally bound, though note that this assumes that the clouds are in equilibrium. Under these assumptions, and using the previously determined value of $a \sim 1.8$ to obtain $k \sim 1.1\bar{6}$, virial ratios of $\alpha = \{0.28, 0.40, 0.23, 0.68\}$ are determined for clouds G0.25, ‘d’, ‘e’ and ‘f’, respectively. Given that the clouds appear to be sub-virial, it is therefore concluded that all clouds are likely gravitationally bound. Note that the effect of magnetic pressure has not been

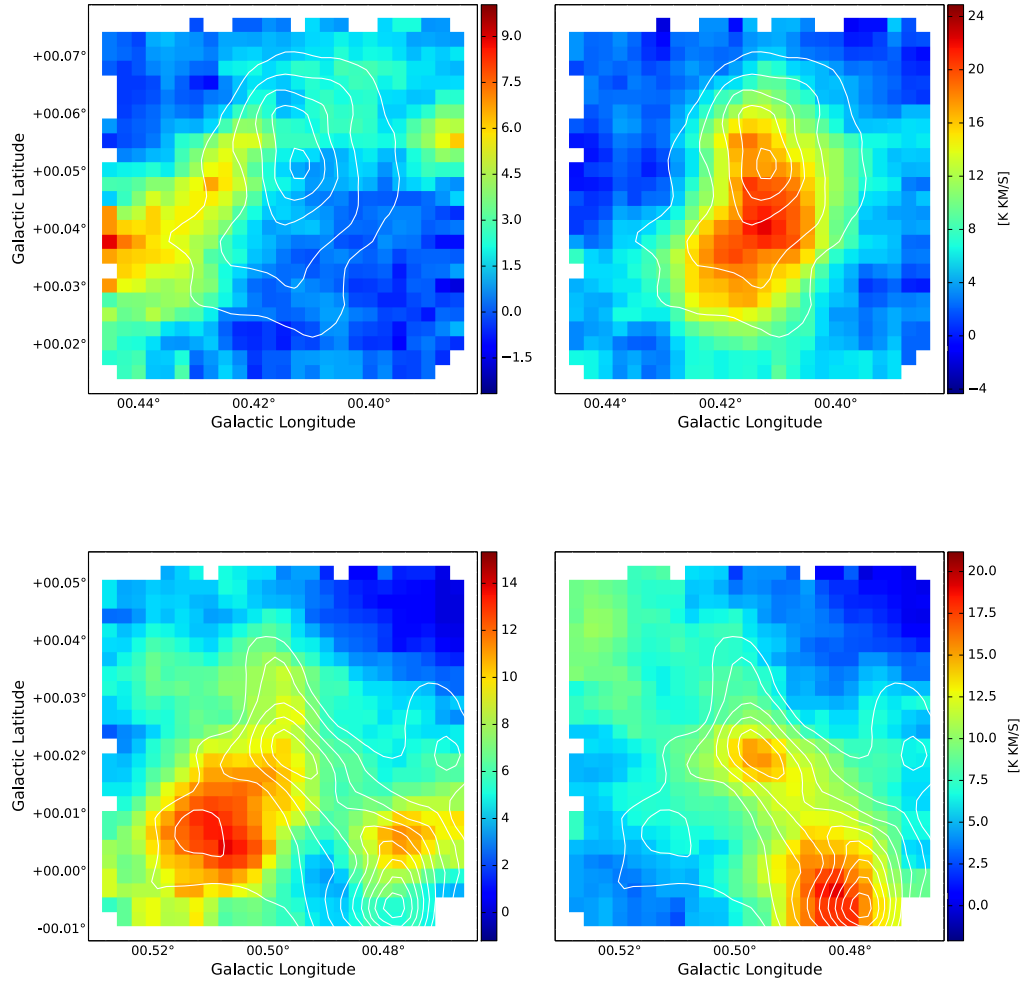


Figure 2.5: **(Top)** Integrated HNC O intensity maps of cloud ‘d’ showing emission integrated between -10 to 5 km s^{-1} (*left*) and 5 to 50 km s^{-1} (*right*). **(Bottom)** Integrated HNC O intensity maps over clouds ‘e’ and ‘f’ showing emission integrated between 5 – 25 km s^{-1} (*left*) and 25 – 50 km s^{-1} (*right*). Overlaid in white are contours from the HiGAL column density maps. These maps show that the emission over the lower velocity range does not match the morphology of the dust emission toward these clouds well. Thus, it is assumed that this emission arises from unrelated clouds along the line of sight.

accounted for in this analysis.

2.2.6 Time-scales

Using the derived masses, radii and line-widths, the sound crossing times, cloud crossing times and free-fall times are determined for these clouds (see Table 2.1). Firstly the sound speed is determined via $c_s = \sqrt{kT_g/\mu}$, where k is the Boltzmann constant, μ is the mean molecular weight (taken to be $2.8m_H$) and T_g is the gas temperature (assumed to be 70 K in all cases (Ao et al., 2013), though note that this was only measured for G0.253+0.016, and it is assumed that this is also true for the other clouds. Any associated uncertainty in the sound speed is smaller as $c_s \sim T^{0.5}$). This is then used to estimate the Mach number as $\mathcal{M} = \sigma/c_s$ (where $\sigma = \Delta V/2.355$). The sound crossing time is estimated as $t_{sc} = R/c_s$ and the cloud crossing time as $t_{cc} = R/\sigma$. Finally, the free-fall time is determined via $t_{ff} = \sqrt{3\pi/32G\rho}$, where ρ has been estimated under the assumption of a uniform spherical distribution.

2.3 Discussion

Table 1 displays the derived global properties for clouds G0.253+0.016, ‘d’, ‘e’ and ‘f’, along with characteristic densities and time-scales for each cloud. These results highlight that all of these clouds are extremely massive and compact objects, containing $\sim 10^5 M_\odot$ within only a few parsecs, resulting in correspondingly high column and volume densities and short dynamical time-scales. Coupling these results with the fact that the clouds are likely to be close to virial equilibrium, the conclusion of Longmore et al. (2013b) is confirmed; that these clouds are all excellent YMC progenitor candidates. Intriguingly, there are no clouds yet known to exist in the rest of the Galaxy that have such extreme masses and densities that are not forming stars prodigiously (Ginsburg et al., 2012; Urquhart et al., 2013). The fact that clouds as massive and dense as these currently exhibit minimal signs of active star formation may therefore have important implications. For example, it may suggest that star and cluster forma-

Cloud	M $10^4 M_{\odot}$	D [†] kpc	R pc	T _{dust} K	ΔV km/s	M _{vir} $10^4 M_{\odot}$	α –	n 10^4 cm^{-3}	N _{H₂} 10^{24} cm^{-2}	t _{cc} Myr	t _{sc} Myr	t _{ff} Myr	M	R ₅ pc
G0.25	11.9	8.4	2.9	19-27	15.1 ± 1.0*	8.3	0.28	1.7	0.6	0.44	6.2	0.24	14.1	1.0
d	7.6	8.4	3.2	19-23	14.1 ± 0.5	10.7	0.40	0.8	0.3	0.52	6.9	0.34	13.2	1.2
e	11.2	8.4	2.4	17-22	14.9 ± 0.1	7.3	0.23	2.8	0.9	0.37	5.2	0.18	13.9	0.8
f	7.3	8.4	2.0	18-22	22.5 ± 0.2	6.9	0.68	3.2	0.8	0.20	4.3	0.17	21.0	1.0

Table 2.1: Global properties of clouds G0.253+0.016, 'd', 'e' and 'f'. The columns show mass (M), distance (D), radius (R), dust temperature (T_{dust}), linewidth (ΔV), Virial mass (M_{vir}), Virial ratio (α) average volume density (n), average column density (N_{H₂}), cloud-crossing time (t_{cc}), sound-crossing time (t_{sc}), free-fall time (t_{ff}), Mach number (M) and the radius within which $5 \times 10^4 M_{\odot}$ is enclosed (R₅). *Result from Longmore et al. (2012). †Galactrocentric distance estimate from Reid et al. (2009a) – all clouds are assumed to be at this distance. Sound speed is calculated using a gas temperature of 70 K (Ao et al., 2013).

tion proceeds differently at the Galactic centre than in the disc (see Chapter 4, also Longmore et al., 2014b, and references therein), or that we have simply caught the earliest stages of YMC formation in four separate cases. Given that the environment at the Galactic centre is extreme compared to the disc (Shetty et al., 2012; Kruijssen & Longmore, 2013), it is plausible that star formation may be inhibited in some way (Longmore et al., 2013a; Kruijssen et al., 2014). However, it is known that YMCs can and do form near the Galactic centre since at least two YMCs, the Arches and Quintuplet clusters, have formed there. The existence of YMCs at the Galactic centre therefore adds further weight to the conclusion that these extreme clouds have the capacity to form YMCs. The following section explores how these clouds can be used to gain insight in to the process of YMC formation.

2.3.1 Comparing Clouds & Clusters

Having derived the global properties of G0.253+0.016, ‘d’ ‘e’ and ‘f’ and confirming that they are sufficiently massive and dense to potentially form YMCs, their properties are now compared to the observed properties of the intermediate and final stages of YMC evolution. The reasoning here is that comparing YMCs in their initial, intermediate, and final stages serves to build up a coherent picture of how these different stages connect to one-another and ultimately determine whether the process of YMC formation is fundamentally different from that which forms low-mass clusters. Two common cluster formation scenarios are discussed here, which can be distinguished by comparing the initial gas sizes and densities ($R_{init}^{gas}, \rho_{init}^{gas}$) with those of the resultant stellar population (R_{fin}^*, ρ_{fin}^*) (see Longmore et al., 2014b, and references therein for a more detailed discussion):

- (i) A bound, centrally-condensed stellar population forms in an extremely compact natal gas cloud (i.e. $R_{init}^{gas} < R_{fin}^*$; $\rho_{init}^{gas} > \rho_{fin}^*$). Feedback processes gradually remove the remaining gas, diluting the global potential and causing the cluster to expand towards its final, un-embedded phase (see e.g. Lada et al., 1984; Boily & Kroupa, 2003; Bastian & Goodwin, 2006; Baumgardt & Kroupa, 2007). This

results in a bound, spherical cluster with $R_{fin}^* > R_{init}^{gas}$.

- (ii) Stars and sub-clusters form in a gas cloud with $R_{init}^{gas} > R_{fin}^*$, $\rho_{init}^{gas} < \rho_{fin}^*$. They form throughout the spatial extent of their natal gas clouds, following the hierarchical structure of the interstellar medium (Larson, 1981). A heightened star formation efficiency (SFE) in the densest peaks leads to gas exhaustion on local scales, causing stellar dynamics to eventually dominate (Kruijssen et al., 2012; Girichidis et al., 2012). The subsequent hierarchical merging of these condensations results in a centrally concentrated, bound cluster (Fujii et al., 2012; Parker et al., 2014a).

In essence, these two scenarios should be distinguishable by studying the most likely progenitor systems – massive and compact molecular clouds. If scenario (i) is a common mode of YMC formation, it would require that there are $\gtrsim 10^5 M_{\odot}$ clouds that are *more or equally as compact* as Galactic YMCs. If instead scenario (ii) is favoured, then one might expect to only find clouds with sizes larger than those of YMCs that show fragmented sub-structure on small spatial scales that is distributed throughout the spatial extent of the cloud (i.e. not strongly centrally-concentrated). Given that G0.253+0.016, ‘d’ ‘e’ and ‘f’ represent the most extreme quiescent molecular clouds known in the Galaxy, they offer an ideal sample of progenitor systems with which the validity of these two scenarios can be examined, prior to the loss of initial structure due to feedback from high-mass star formation. One can begin to distinguish between these scenarios simply by looking at their mass distributions, to compare how the mass is distributed in YMCs and their precursors.

The HiGAL column density maps are used to obtain mass surface density profiles for clouds ‘d’ ‘e’ and ‘f’ by calculating the enclosed mass (see §2.2) within increasing circular apertures (centred on column density peaks) and dividing by the area of the corresponding aperture. For G0.253+0.016, ALMA Cycle 0 + single-dish data are used (Rathborne et al., 2014b). These data consist of ALMA observations at 3 mm, with an angular resolution of 1.7'' (0.07 pc at a distance of 8.4 kpc). These data were combined with Herschel 500 μm to recover the flux that is filtered out by the interferometric ob-

ervation. The resolution of the ALMA data allows us to investigate the surface density profile of this cloud down to much smaller radii. Rathborne et al. (2014a) find evidence for fragmentation and hierarchical small-scale structure in G0.253+0.016. Furthermore, the ALMA data (Rathborne et al., 2014b) directly reveals such sub-structure within this cloud, showing that the gas is highly fragmented and contains a number of dense cores distributed throughout the cloud (see Rathborne et al. 2015 for detailed analysis of the cloud’s sub-structure). This suggests that if G0.253+0.016 truly is a proto-YMC cloud, then the combination of its internal structure, lack of central concentration and radius of several parsecs are more consistent with a hierarchical view of massive cluster formation. However, fragmented sub-structure alone does not mean that this is necessarily true, as this is a known property of the ISM in general. Higher resolution data for the other dust ridge clouds show similar sub-structure (see Chapter 4).

In all following plots, a multiplicative factor of 1/3 is applied to the data for G0.253+0.016, ‘d’ ‘e’ and ‘f’ such that it can be inferred what a resultant stellar population would look like if it were to form with a star formation efficiency (SFE, ϵ) of 1/3 at the current mass distribution of the clouds. In reality, SFE will of course vary throughout the cloud, where it will be enhanced towards local density peaks – this factor is chosen to represent a global SFE.

Identifying the Intermediate Phase

To investigate the active star-forming phase of YMC formation, the gas and stellar content of the well-known star-forming Sagittarius B2 complex (Sgr B2, e.g. Qin et al., 2011) is studied. Both Sgr B2 Main and North are studied, as these are potential proto-YMCs in a deeply embedded phase and lie in roughly the same region as G0.253+0.016, ‘d’ ‘e’ and ‘f’. Qin et al. (2011) use data from the Submillimeter Array (SMA) to investigate the dense sub-structure within Sgr B2 Main and North. Interestingly, they find that Sgr B2 Main contains many sub-mm sources that appear to have a fragmented spatial distribution, whereas Sgr B2 North only contains two sub-

mm sources. They propose that this may suggest that the main cluster is more evolved and that northern cluster is less evolved and characterised by monolithic high-mass star formation.

The emission from the gas and dust in Sgr B2 is saturated in the HiGAL data. To obtain surface density profiles for the gas in Sgr B2 Main & North, data from the Bolocam Galactic Plane Survey (BGPS, Rosolowsky et al., 2010; Aguirre et al., 2011; Ginsburg et al., 2013) are used. These data are at a wavelength of 1.1 mm and provide an angular resolution of $\sim 33''$ (~ 1.3 pc at a distance of 8.4 kpc).

As these data are being used to generate mass surface density profiles for the clouds, the data must be converted from units of intensity to units of mass. This is done via the following relation (Kauffmann et al., 2008) –

$$M = \frac{d^2}{\kappa_\nu B_\nu(T)} \int I_\nu d\Omega = \frac{d^2 F_\nu}{\kappa_\nu B_\nu(T)} \quad (2.5)$$

which can be written in the more-readily useable form –

$$M = 0.12 M_\odot \left(e^{1.439(\lambda/\text{mm})^{-1}(T/10 \text{ K})^{-1}} - 1 \right) \times \left(\frac{\kappa_\nu}{0.01 \text{ cm}^2 \text{ g}^{-1}} \right)^{-1} \left(\frac{F_\nu}{\text{Jy}} \right) \left(\frac{d}{100 \text{ pc}} \right)^2 \left(\frac{\lambda}{\text{mm}} \right)^3 \quad (2.6)$$

where M is the mass, λ is the wavelength, T is the dust temperature, κ_ν is the dust opacity, F_ν is the integrated flux and d is the distance. The distance to all sources is taken to be 8.4 kpc (Reid et al., 2009a, 2014). The dust temperature is assumed to be 20 K, though in a star-forming complex like Sgr B2, the dust temperature will not be isothermal due to heating from the embedded HII regions and stellar population. Additionally, it is known that the kinematic structure of Sgr B2 is complex, with multiple velocity components towards the region. As a result, any mass and density estimates for the gas in this region will be upper limits. Schmiedeke et al. (2016) model the

region in more detail. The dust opacity (κ_ν) is not observationally constrained towards these clouds. This is estimated using the following relation (Battersby et al., 2011) –

$$\kappa_\nu = 0.04 \text{ cm}^2 \text{ g}^{-1} \left(\frac{\nu}{505 \text{ GHz}} \right)^{1.75} \quad (2.7)$$

where ν is the frequency. Note that this contains the explicit assumption that the gas-to-dust ratio is 100, which may not be valid in the CMZ (Longmore et al., 2013a). Kauffmann et al. (2008) note that the uncertainties in both the dust temperature and opacity mean that the systematic uncertainties in mass estimates obtained via Equation 2.6 are a factor of ~ 2 . See Longmore et al. (2013a) for a more in-depth discussion regarding the systematic uncertainties in obtaining mass estimates from dust emission in this environment.

Obtaining a mass surface density profile of the proto-cluster(s) within Sgr B2 is difficult due to the high column densities and hence extinction towards the region. To overcome this, an indirect method is employed to estimate the embedded stellar mass via observations of Ultra-Compact HII (UCHII) regions in Sgr B2. The positions and zero age main-sequence (ZAMS) spectral classifications of the stellar sources embedded in the UCHII regions are taken from Tables 2 and 3 in Gaume et al. (1995). Here, the number of Lyman continuum photons are used to estimate the ZAMS spectral type of the star that is powering the UCHII region. Lyman continuum photons are those with sufficient energy to ionise neutral hydrogen ($h\nu > 13.6 \text{ eV}$), and are abundant in the radiation output from high-mass stars ($\gtrsim 8 M_\odot$). Under the assumption that the continuum emission is optically thin, and assuming some form for the geometry and density distribution, the number of Lyman continuum photons is calculated based upon the size of the source, the recombination rate, and the electron temperature and density. Gaume et al. (1995) calculate this following the equations given in Turner & Matthews (1984), and assume a distance of 8.5 kpc and an electron temperature of 10,000 K. This is then used to take an estimate for the spectral type from Panagia (1973), in which a number of expected parameters (including Lyman continuum flux) were calculated for a range of O and B stars. The spectral type of each source is then converted to a representative

mass using the spectroscopic masses of ZAMS OB stars given in Table 5 (column 8) of Vacca et al. (1996). These masses are derived from spectroscopic models of OB stars, and it must be noted that these are systematically lower than the masses derived from evolutionary track models (Table 5, column 9). This difference in mass estimates can be as large as a factor of 2, and any mass estimates in the following analyses are considered to be lower-limits.

Knowing the spatial distribution and masses of the OB stars within Sgr B2 and assuming a distance of 8.4 kpc, the *total* stellar mass enclosed within increasing circular apertures is estimated to generate mass surface density profiles. Given that the observations in Gaume et al. (1995) are sensitive only to stars $\gtrsim 10 M_{\odot}$, the total mass is estimated by applying a Kroupa-type IMF (Kroupa, 2001), for which the fraction of mass $>10 M_{\odot}$ is ~ 0.16 . The total mass is therefore estimated by applying a multiplicative factor of $1/0.16$ and normalising by the mean stellar mass of $\sim 0.5 M_{\odot}$. Taking all 25 sources in Gaume et al. (1995), a total stellar mass of $\sim 3.5 \times 10^3 M_{\odot}$ is estimated.

Comparison to Galactic YMCs

For comparison with Galactic YMCs, the Arches cluster is discussed here as it is massive ($M \sim 2 \times 10^4 M_{\odot}$), compact ($R_{eff} \sim 0.4$ pc), young (Age $\sim 2 - 3$ Myr) and is situated towards the Galactic centre and therefore a similar environment to Sgr B2, G0.253+0.016, ‘d’ ‘e’ and ‘f’ (Portegies Zwart et al., 2010; Schneider et al., 2014). If YMC radii and central densities are related to the tidal radius, such that more compact YMCs are most likely to survive in stronger tidal fields, it is important that we compare clouds and clusters within the Galactic centre so as to eliminate any environmental variations. The Quintuplet cluster is also situated towards the Galactic centre. However, it is an older system than the Arches and it has been suggested that the disruption time-scale of clusters at the Galactic centre is short, occurring over ~ 10 Myr (Kim et al., 1999; Portegies Zwart et al., 2002; Kruijssen et al., 2014). As such, only the Arches is considered for comparison here as it is more likely representative of an

initial YMC distribution. The observed surface density profile is taken from Figure 16 of Espinoza et al. (2009), along with the given best-fit King density profile and parameters, correcting for the number and masses of stars below $10 M_{\odot}$ with a Kroupa-type IMF. The observed cumulative mass profile given in Figure 3 of Harfst et al. (2010) is also used, again IMF-corrected for stars below $10 M_{\odot}$.

Figure 2.6 displays the enclosed mass as a function of radius for G0.253+0.016, ‘d’, ‘e’ and ‘f’ (solid lines) given $\epsilon = 1/3$, the gas in Sagittarius B2 Main and North (dashed lines) and the Arches cluster from Espinoza et al. (2009) (black, dash/dot) and Harfst et al. (2010) (red, dash/dot). The plot shows that G0.253+ 0.016, ‘d’ ‘e’ and ‘f’ all contain enough mass such that they can form a YMC of $M > 10^4 M_{\odot}$ given a SFE of $1/3$. However, it is clear in *all* cases that the distribution of mass is much less centrally concentrated than in the Arches, leading to the conclusion that these clouds cannot form an Arches-like YMC at their current densities. Unless they were to condense rapidly on global scales within a free-fall time (~ 0.5 Myr) before the onset of any widespread star formation, it seems implausible that these clouds will form clusters monolithically. This is also true of the gas content of Sgr B2 Main and North. Despite the high mass and density of these regions, the gas is too extended on global scales.

Figure 2.7 shows the resultant mass surface density profiles as a function of radius for G0.253+0.016, ‘d’, ‘e’ and ‘f’ given $\epsilon = 1/3$ (solid lines), the gas in Sagittarius B2 Main and North (dashed lines), the proto-cluster(s) embedded within Sagittarius B2 Main and North as calculated from the UCH_{II} region distribution (blue and red dash/dot, respectively) and the Arches cluster overlaid with the fit from Espinoza et al. (2009) (black open circles, dash/dot). G0.253+0.016, ‘d’ ‘e’ and ‘f’ are less centrally concentrated than the Arches’ stellar distribution, and further dynamical evolution would be required to condense any resultant stellar populations if they were to form at the current densities of the clouds. This is also true for the gas content of Sgr B2 Main and North. Even though they are significantly more massive, dense and evolved than the other clouds, the gas has a fairly shallow distribution on global scales. This is in contrast to the inferred stellar content in Sgr B2, where the H_{II} regions of both Sgr B2 Main and North are concentrated in a small volume (< 0.1 pc). This shows that

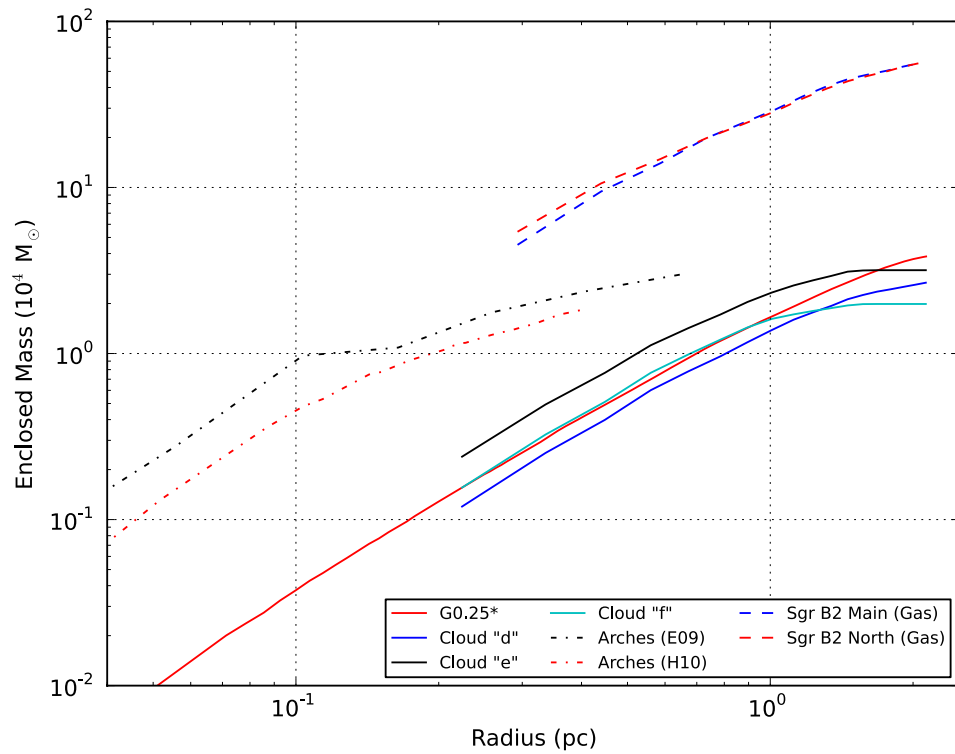


Figure 2.6: Enclosed mass as a function of radius for G0.253+0.016, ‘d’, ‘e’, ‘f’ given $\epsilon = 1/3$ (solid lines), the gas in Sagittarius B2 Main and North (dashed lines) and the Arches cluster from Espinoza et al. (2009) (E09; black, dash/dot) and Harfst et al. (2010) (H10; red, dash/dot). G0.253+0.016* (red) ALMA cycle 0 + single-dish data (Rathborne et al., 2014b). This shows that in all cases, the gas in the proto-cluster clouds has a more extended distribution of mass, whereas the stellar population of the Arches is more centrally concentrated.

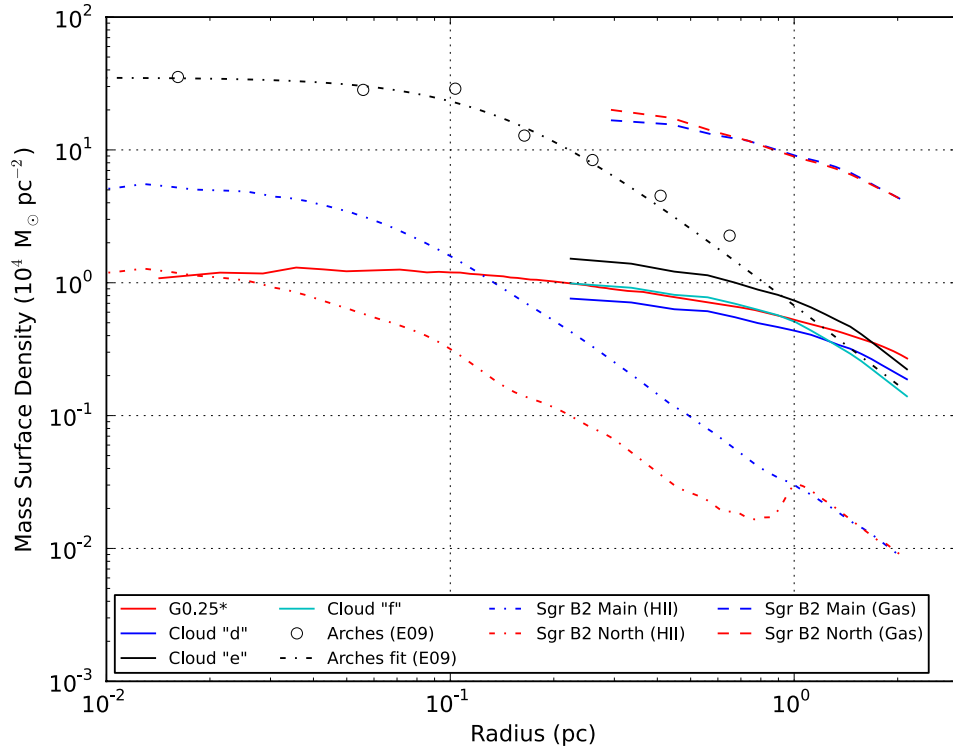


Figure 2.7: Mass surface density profiles as a function of radius for G0.253+0.016, ‘d’, ‘e’, ‘f’ given $\epsilon = 1/3$ (solid lines), the gas in Sagittarius B2 Main and North (dashed lines), the proto-cluster(s) embedded within Sagittarius B2 Main and North as calculated from the UCHII region distribution (blue and red dash/dot, respectively) and Arches cluster overlaid with fit from Espinoza et al. (2009) (E09; black open circles, dash/dot). These profiles show that the final stellar distribution of the YMC is *more compact* than the global distribution of stars and gas at any prior stage of the formation process. Note that the variation of the profiles for the HII region distribution in Sgr B2 at small radii is a result of the small number of sources detected there. The bump at $R \sim 1.0$ pc is due to Sgr B2 Main entering the aperture at that radius. G0.253+0.016* (red) ALMA cycle 0 + single-dish data (Rathborne et al., 2014b).

dense, centrally concentrated proto-clusters are able to form in clouds that are not very centrally concentrated, as predicted by hydrodynamical cluster formation simulations (Kruijssen et al., 2012). Furthermore, it is found that, at least for this sample of clouds towards the Galactic centre, the final stellar distribution of an Arches-like YMC is more compact than the global distribution of stars *and* gas at any prior stage of the formation process. Given that these are the most massive and dense quiescent clouds yet found in the Galaxy, this leads to the conclusion that scenario (i) – a monolithic formation event – is disfavoured as a likely mode of YMC formation.

Having investigated the absolute mass and surface density profiles, the *shape* of the

radial mass distribution is now considered. Figure 2.8 displays the normalised mass surface density profiles for G0.253+0.016, ‘d’, ‘e’ and ‘f’ (solid lines), the gas in Sagittarius B2 Main and North (dashed lines), the Sagittarius B2 Main and North proto-clusters (blue and red dash/dot, respectively) and the Arches cluster (black, dash/dot), where all profiles have been normalised to unity at a radius of ~ 0.3 pc (the resolution of the BGPS data at a distance of 8.4 kpc). This plot shows that in *all* cases, the gas in the YMC progenitors is over-dense at large radii and under-dense at small radii, compared to the stellar components in both the Arches cluster and the Sgr B2 proto-clusters. This suggests that if these clouds are to form YMCs, the resultant stellar population would have to dynamically interact such that it would relax into a much more centrally-condensed distribution. It is interesting that the gas distribution in both Sagittarius B2 Main and North on global scales is very similar to that in the quiescent ‘dust-ridge’ clouds. It is well known that clustered massive star formation is underway in Sgr B2, yet the global gas content looks similarly distributed to that in the quiescent dust ridge clouds. This is in conflict with scenario (i), which requires the gas to be more centrally concentrated prior to the formation of a YMC.

It is also interesting to note the high mass surface density of Sgr B2 proto-clusters on scales smaller than ~ 0.1 pc. The bulk of the stellar mass, though roughly an order of magnitude lower than the Arches, is highly concentrated within a small core region. It is difficult to determine whether this is consistent with scenario (i), in which case the stars may have formed in a centrally-condensed distribution, or whether it is consistent with scenario (ii), where the stars may be distributed in this way as a result of rapid dynamical interaction. N-body simulations show that dynamical mass segregation due to violent relaxation can occur in less than 1 Myr for clusters $\sim 10^3 M_{\odot}$ (Parker et al., 2014b). It is therefore possible that the high-mass stars powering the UCHII regions in Sgr B2 need not have formed at their present locations. However, more thorough analyses would be required to determine this.

The main result of this section is that none of the Galactic centre YMC-precursor candidates could form an Arches-like cluster without further dynamical evolution, if a stellar population formed at the current mass distributions within the clouds. However,

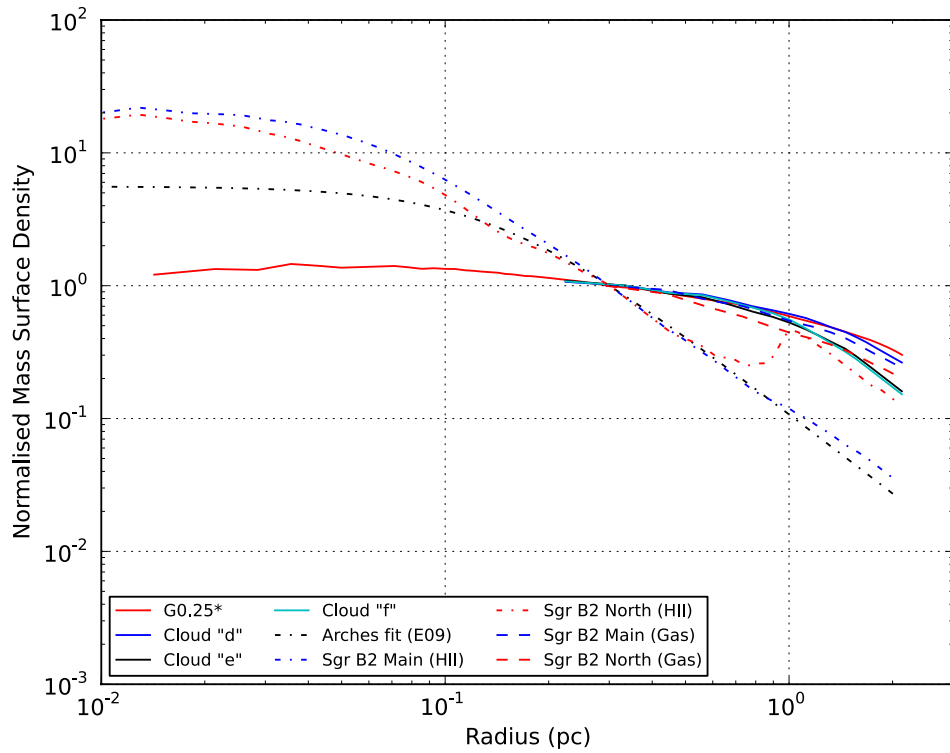


Figure 2.8: Normalised mass surface density profiles as a function of radius for the gas in G0.253+0.016, ‘d’, ‘e’, ‘f’ (solid lines), the gas in Sagittarius B2 Main and North (dashed lines), the proto-cluster(s) embedded within Sagittarius B2 Main and North as calculated from the UCHII region distribution (blue and red dash/dot, respectively) and the Arches cluster from Espinoza et al. (2009) (E09; black dash/dot). Each profile has been normalised to unity at a radius of ~ 0.3 pc, as this is the resolution of the BGPS data. G0.253+0.016* (red) ALMA cycle 0 + single-dish data (Rathborne et al., 2014b). The shapes of the profiles at larger radii suggests an evolutionary progression on global scales from a dispersed natal gas cloud to a centrally condensed stellar cluster as a function of star formation activity.

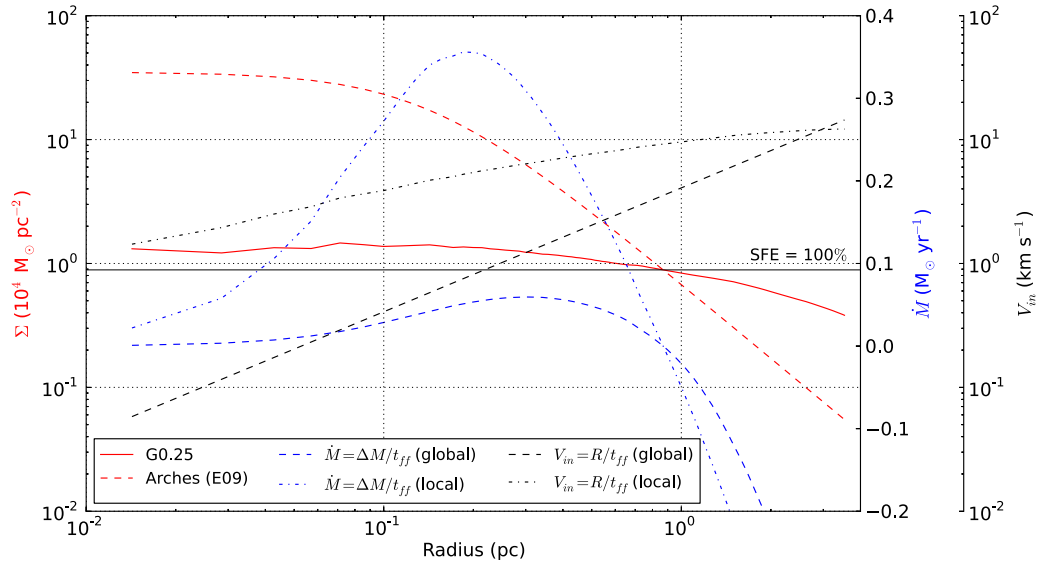


Figure 2.9: Mass surface density profiles as a function of radius for G0.253+0.016 (Rathborne et al., 2014b, solid red line, ALMA cycle 0 + single-dish data), and the stellar content of the Arches cluster (Espinoza et al., 2009, (E09), dashed red line). The solid black horizontal line shows the limit above which a star formation efficiency greater than 100% would be required for G0.253+0.016 to form an Arches-like cluster at its current mass distribution. The blue dashed curve displays the mass-flow-rate that would be required for a cloud like G0.253+0.016 to collapse to the mass distribution of an Arches-like cluster within a global free-fall time (0.24 Myr, see Table 2.1). The blue dash-dot curve shows the same, but for a local free-fall time, which is evaluated as a function of radius. The corresponding values for these blue curves are given on the inner right-hand y-axis. The black dashed curves show the infall velocity that would be required to fall to the centre within a free-fall time. These are again calculated using a global free-fall time (dashed) and a local free-fall time as a function of radius (dash-dot), and the corresponding values are given on the outer right-hand y-axis.

it is unlikely that stars will form with the exact distribution of the clouds. To test whether this could affect our conclusions, Figure 2.9 shows a comparison between the mass-surface density profiles of G0.253+0.016 and the Arches. To test whether a radially-varying star formation efficiency (SFE) could enable G0.253 to form an Arches-like cluster at its present distribution, a ratio of the two profiles is taken. As the solid black horizontal line shows, below radii of ~ 0.8 pc, the required SFE would have to be greater than 100%. This is of course unphysical, and so it is concluded that a radially-varying SFE alone would not be sufficient. The blue dashed curves in Figure 2.9 show the rate at which mass would be required to inflow such that the mass distribution of G0.253 would look like that of the Arches. This is calculated given a global free-fall time (blue dashed line) and a local free-fall time that is estimated as a function of radius (blue dash-dot line). This shows that mass-flow rates of up to $\sim 0.36 M_{\odot} \text{ yr}^{-1}$ would be required. However, this assumes 100% SFE, and would require that global mass flows were convergent. Also plotted is the inflow velocity that would be required for the gas to fall to the centre of the cloud in a free-fall time. This is again calculated for the global (black dashed line) and local (black dash-dot line) free-fall times. The maximum infall velocities required are $\sim 15 \text{ km s}^{-1}$. Given the large velocity dispersions in these clouds ($10\text{-}20 \text{ km s}^{-1}$), this does not seem unreasonable. However, this assumes global infall, and the actual kinematics in G0.253 are much more complex (e.g. Rathborne et al., 2015). In summary, this shows that while a radially-varying SFE alone could not transform the mass distribution of these clouds to look like that of the Arches, it seems plausible that the observed bulk motions of the clouds would be sufficient to accumulate enough mass towards the centre of the clouds within a free-fall time. However, without knowledge of the 3D motions of the gas in the clouds it is not possible to say anything more definitive than this, and detailed analyses of the global kinematics would be required to do so.

2.4 Conclusions from Walker et al. (2015)

Using HiGAL far-IR continuum data and MALT90 millimetre spectral line data, the global properties of four likely YMC precursors towards the Galactic centre are derived. These clouds, G0.253+0.016, ‘d’ ‘e’ and ‘f’, are all found to be high mass ($M \sim 10^5 M_{\odot}$), cold ($T_{dust} \sim 20$ K) and dense ($n \sim 10^4 \text{ cm}^{-3}$). They are all likely close to virial equilibrium and are therefore likely to be gravitationally bound. These results confirm that they are excellent YMC progenitor candidates – they are amongst the most massive and dense molecular clouds known to exist in the Galaxy, yet they are devoid of any widespread star formation.

Comparison of the mass surface density distributions of these clouds with the Sagittarius B2 proto-YMC and the Arches YMC shows that these clouds are not compact or centrally concentrated enough to form an Arches-like YMC in their current state. If they are to form YMCs, dynamical evolution during the early formation must further condense the resultant stellar population. Furthermore, we find that the stellar content of both Sagittarius B2 Main and North is significantly more centrally concentrated than the global gas content. This shows that dense, centrally concentrated stellar clusters can form from gas that is not very centrally condensed, thus disfavouring a monolithic mode of YMC formation in which gas expulsion causes the YMC to end up less compact than the progenitor gas cloud.

Chapter 3

Comparing young massive clusters and their progenitors throughout the Milky Way

Preface

The work presented in this chapter is based upon that of Walker et al. (2016). I led this work as first author, and all of the contents (text, analyses, figures, tables) are my own.

3.1 Introduction

In the previous chapter, the properties of the quiescent dust ridge clouds were compared with those of (proto)-YMCs at the Galactic centre in an effort to assess the validity of cluster formation scenarios that are often discussed in the literature (Walker et al., 2015). It is found that the YMC progenitors there are not dense enough nor are they centrally-concentrated enough to form an Arches-like ($M = 2 \times 10^4 M_{\odot}$, R_{eff}

= 0.4 pc; Espinoza et al., 2009) YMC without further dynamical evolution, despite them being the most massive and dense quiescent clouds found in the Galaxy. This result suggested that, at the Galactic centre, a monolithic mode of YMC formation is not viable given the present-day mass distribution within these clouds. Instead, a hierarchical build up and merging of stellar mass is suggested to be more likely.

Given that the Galactic centre is an extreme environment – with density, temperature, pressure, cosmic ray ionisation rate and magnetic field strength ranging from a factor of a few to orders of magnitude greater than in the Galactic disc (Kruijssen & Longmore, 2013) – it seems plausible that our previous result may be one that is specific to such an environment. Observing and characterising any environmental dependence of YMC formation is crucial if a complete understanding of how they form and evolve as a function of environment is to be obtained, and may also have implications for the formation of *all* stellar clusters across the full mass range. Here, this study is therefore extended out into the more benign environment of the Galactic disc, combining the previous sample with the known YMCs and their likely progenitors in the disc.

In this chapter, revised potential formation scenarios for YMCs are discussed. Whilst the discussion on monolithic vs. hierarchical formation may describe the initial stellar distribution, it doesn't sufficiently explain the concurrent density evolution of both the gas and stars during the formation of a YMC. Instead, the work in this chapter considers the following three general scenarios for YMC formation –

'Conveyor-belt': Gas and stars have initial density distributions that are lower than that of an un-embedded YMC. Evolution is defined by the concurrent collapse of the molecular cloud and on-going star formation.

'In-situ': Gas is initially at a similar density as the final YMC stellar distribution. Stars can form at this density with little-to-no expansion or contraction.

'Popping': Gas is initially at a higher density than the un-embedded YMC. Once the stellar population has formed, the cluster expels its gas content and expands towards its final density distribution.

	Before significant star formation ($t_{gas,initial}$)	Embedded cluster ($t_{*,initial}$)	Un-embedded cluster ($t_{*,final}$)
<i>‘Conveyor-belt’</i>	$R_{gas,initial} > R_{*,final}$	$R_{*,initial} > R_{*,final}$	$R_{*,final}$
<i>‘In-situ’</i>	$R_{gas,initial} \approx R_{*,final}$	$R_{*,initial} \approx R_{*,final}$	$R_{*,final}$
<i>‘Popping’</i>	$R_{gas,initial} < R_{*,final}$	$R_{*,initial} < R_{*,final}$	$R_{*,final}$

Table 3.1: Summary of the global properties of the gas and stellar content at three distinct phases in three different proposed formation scenarios for YMCs. $t_{gas,initial}$ denotes the stage at which the YMC precursor cloud has not yet formed the majority of its stellar population. $R_{gas,initial}$ is the radius at this stage. The subscript (*, initial) refers to these properties at the stage at which most of the stars in the cluster have been formed, but the cluster is still embedded in the remaining gas. (*, final) indicates the final stage of YMC formation, where the cluster is completely free of gas.

Table 3.1 summarises the relevant general properties of the stellar and gas distributions in these different scenarios.

3.2 Data

For the Galactic YMC sample, all YMCs that are given in Portegies Zwart et al. (2010) with $M \gtrsim 10^4 M_{\odot}$ that have their surface density profiles published are selected. The sample of Galactic YMC precursor clouds is taken from those currently reported in the literature that satisfy the Bressert et al. (2012b) criterion – that the clouds have escape speeds larger than the sound speed in ionised gas. (Ginsburg et al., 2012; Urquhart et al., 2013; Longmore et al., 2013b).

3.2.1 Galactic Centre

Clouds

Following from the previous chapter, the four quiescent Galactic centre dust ridge clouds – G0.253+0.016, ‘d’, ‘e’ and ‘f’ – are included, along with the gas content surrounding the Sagittarius B2 Main and North proto-clusters. The analysis of these clouds is given in the previous chapter. Data utilised are continuum data from the Herschel infrared Galactic Plane Survey (HiGAL, Molinari et al., 2010), Bolocam

Galactic Plane Survey (BGPS, Rosolowsky et al., 2010; Aguirre et al., 2011; Ginsburg et al., 2013) and ALMA project: ADS/JAO.ALMA#2011.0. 00217.S (Rathborne et al., 2014b, 2015).

Clusters

The Galactic centre is known to host at least two YMCs (Arches and Quintuplet) and two possible proto-YMCs (Sagittarius B2 Main and North). The cluster disruption time-scale in this environment is very short, occurring over only a few to 10 Myr as a result of the strong tidal field and, most importantly, the disruptive tidal interactions with the dense gas (e.g. Kim et al., 1999; Portegies Zwart et al., 2002; Kruijssen et al., 2014). To compare YMC progenitor clouds with the initial conditions of the stellar content of YMCs, the Quintuplet cluster is not included in the sample, as it is already $\sim 4\text{--}5$ Myr old (Figer et al., 1999c; Schneider et al., 2014) and tidal disruption may have influenced the stellar surface density distribution.

The global properties and observed mass surface density profile for the Arches stellar cluster were obtained from Espinoza et al. (2009, Table 8 and Figure 16). Data for the stellar population of Sagittarius B2 proto-clusters (Main & North) were extrapolated from the Gaume et al. (1995) radio observations of the embedded ultra-compact HII (UCHII) regions. See the previous chapter for a detailed explanation of how these data were used to generate mass surface density profiles.

3.2.2 Galactic disc

Clouds

Ginsburg et al. (2012) and Urquhart et al. (2013) report a sample of potential YMC precursor clouds in the Galactic disc. Of these, all clouds with $M \gtrsim 3 \times 10^4 M_{\odot}$ are selected, as they could potentially form a $10^4 M_{\odot}$ YMC with a global star formation efficiency of $\sim 1/3$. The clouds that meet these criteria are G043.169+00.009 (W49),

G049.489+00.386 (W51), G010.472+00.026, G350.111+0.089, G351.774−00.537 and G352.622−01.077.

To assess the distribution of mass in these clouds and in particular whether they contain enough mass on small spatial scales to form a YMC at their present distributions, data with the highest possible angular resolution are required. For W49, high spatial-resolution (2'') observations taken with the Submillimeter Array (SMA) are utilised. These data were taken with the SMA at 230 GHz using the subcompact, compact, extended and very extended array configurations. This combination of configurations achieves good uv -coverage, and effectively probes angular scales from 0.5'' – 31'' (Galván-Madrid et al., 2013). Despite using all of the available configurations, the interferometric observations inherently filter out the larger scale emission due to lack of zero-spacing information in the uv -plane. To account for this, Galván-Madrid et al. (2013) combined the SMA 230 GHz (1.3 mm) continuum data with 1.1 mm continuum data from the BGPS (Rosolowsky et al., 2010; Aguirre et al., 2011; Ginsburg et al., 2013). This combination followed the commonly applied technique of taking the Fourier transform of the BGPS data and then combining the visibilities in the uv -plane prior to cleaning. The full details of these observations and combination with single-dish data are discussed in Galván-Madrid et al. (2013).

For both W51 and G010.472+00.026, 450 μm SCUBA observations of these clouds are taken from the JCMT data archive. These data provide an angular resolution of $\sim 7''$. For the full details of these data, please refer to Di Francesco et al. (2008). Note that the effect of spatial filtering with SCUBA is not a concern here, as the primary interest is in the gas and dust distribution on small spatial scales, where such filtering is not an issue.

For the remainder of the clouds in the sample, (sub-)mm continuum data for G350.111+0.089, G351.774-00.537 and G352.622-01.077 are acquired from the archive for the APEX Telescope Large Area Survey of the Galaxy (ATLASGAL, Schuller et al., 2009). These data provide an angular resolution of $\sim 19''$.

As these data will be used to generate mass surface density profiles for the clouds,

they are converted from units of flux to units of mass. This is done in the same way as in the previous chapter (see Equations 2.5 – 2.7). The dust temperature is not fully constrained observationally for these clouds. As such, certain assumptions are made regarding this parameter. These assumptions are as follows –

- (i) The gas is isothermal throughout the extent of the cloud. This is a reasonable assumption for the Galactic centre clouds G0.253+0.016, ‘d’, ‘e’ and ‘f’, as they are quiescent. However the potential disc YMC precursors and Sagittarius B2 Main and North are all highly star-forming, and so it is expected that there will be significant temperature gradients throughout the clouds.
- (ii) This single dust temperature is assumed to be 20 K in all of the quiescent Galactic centre clouds. This is consistent with those measured from Herschel data (Battersby et al., 2011; Walker et al., 2015). In all of the star forming clouds, heightened dust temperatures of 40 K are assumed. The actual dust temperature will be much higher towards sites of star formation. Hence, any masses quoted are upper limits.
- (iii) A constant gas-to-dust ratio of 100 is assumed. Though this may be lower by a factor of ~ 2 towards the Galactic centre (Longmore et al., 2013a).

Table 3.2 displays the general properties of the YMC precursor gas clouds in the sample presented here. This shows that all of the clouds have similar global characteristics, with masses in the range of $10^4 - 10^5 M_{\odot}$, radii of $\sim 2 - 5$ pc and volume densities of $\sim 10^4 \text{ cm}^{-3}$.

Clusters

Any YMCs in the Galactic disc given in Table 2 of Portegies Zwart et al. (2010), for which surface profiles are already published, are selected. These are NGC 3603, Westerlund 1 and Trumpler 14.

The data for NGC 3603 are taken from Figure 14 of Harayama et al. (2008). The data and fit for the surface density profile are taken, and a distance of 6.0 kpc is used to obtain their results in units of $M_{\odot} \text{ pc}^{-2}$. Given that their observations are sensitive to the mass range $0.5 - 2.5 M_{\odot}$, an IMF correction is made to extrapolate down to $0.1 M_{\odot}$ and up to $120 M_{\odot}$. Assuming a Kroupa IMF, a corrective multiplicative factor of ~ 2.8 is estimated. The observed stellar mass surface density profile is then multiplied by this factor to retrieve the underlying total stellar mass surface density profile. Note that the effect of mass segregation has not been accounted for when applying IMF corrections to NGC 3603. Harayama et al. (2008) do report evidence for mass segregation in the very inner regions of the cluster, as indicated by a steepening of the IMF. As this only applies to the very centre of the cluster, they conclude that a single representative IMF for the cluster is justified.

Trumpler 14 data are taken from Figure 10 of Sana et al. (2010). Their observations cover a mass range $0.1 - 120 M_{\odot}$ and so no IMF correction is applied, as the observations should sample the IMF well.

Westerlund 1 data are taken from Figure 8 of Brandner et al. (2008). The data are sampled from a mass range of $3.5 - 32 M_{\odot}$ – extrapolating using a Kroupa IMF yields a multiplicative factor of ~ 4.4 . The observed stellar mass surface density profile is multiplied by this factor to retrieve the underlying total stellar mass surface density profile.

3.3 Results

Figure 3.1 displays the enclosed mass-surface-density profiles of the clouds. These profiles are obtained by using CASA (McMullin et al., 2007) to take cumulative mass measurements within apertures of increasing radii, which are centred on the dust peaks, then dividing by the corresponding aperture area at each increment. As discussed in the previous chapter, the Galactic centre clouds (solid lines) are similar in terms of their surface distributions – flat (down to $r \sim 0.2 - 0.3 \text{ pc}$), with no prominent central

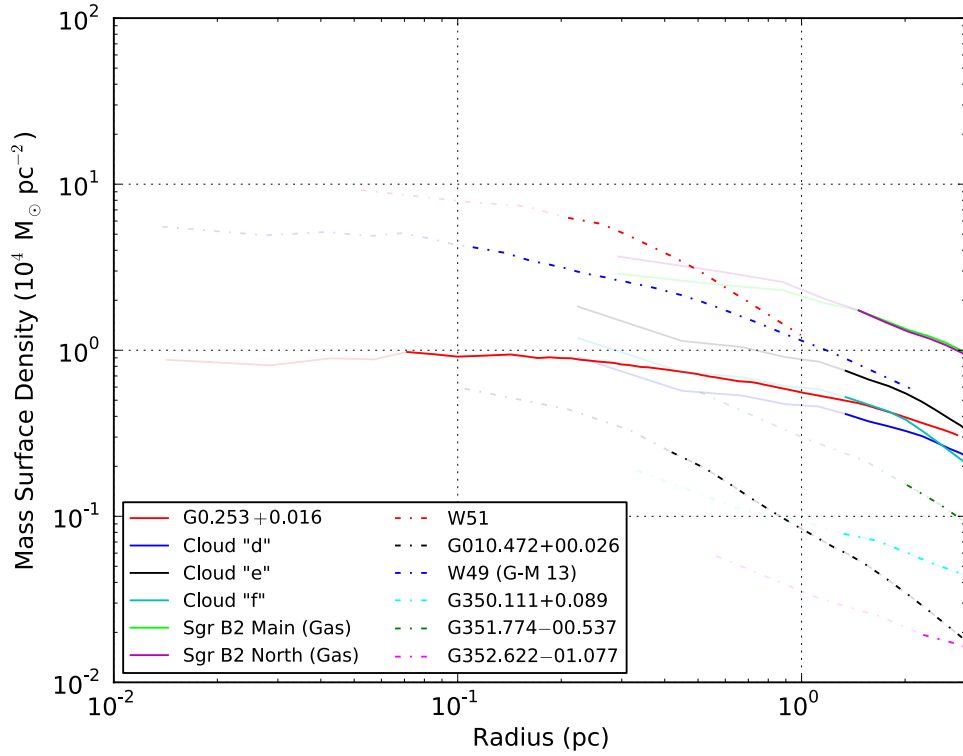


Figure 3.1: Enclosed mass surface density profiles as a function of radius for the YMC precursor clouds in the CMZ (solid lines) and in the Galactic disc (dashed lines). The transition point from solid to lower opacity indicates the beam resolution of the data.

high-density region in the profile. ALMA data show that this continues down to ~ 0.015 pc for the cloud G0.253+0.016 (Rathborne et al., 2014b). Observations using the Submillimeter Array (SMA) show a similar trend for clouds d, e and f (see the data presented in Chapter 4).

Figure 3.1 also shows the YMC progenitor candidate clouds in the Galactic disc (dashed lines). The enclosed mass surface density profiles of these clouds are similar to those of the Galactic centre clouds, in that they are relatively shallow across all spatial scales. Note that the profiles generated using the BGPS and APEX data may be affected by the angular resolution ($33''$ and $19''$, respectively). However, there are no considerable differences in the shapes of the profiles when compared to those taken with higher resolution data.

In analysing the mass distributions in these clouds, it is important to reiterate the assumptions that have gone in to estimating their masses. The assumption that the gas

Cloud	M $10^4 M_\odot$	D kpc	R pc	n 10^4 cm^{-3}	N_{H_2} 10^{24} cm^{-2}	Reference –
G0.253+0.016	11.9	8.4 [†]	2.9	1.7	0.6	1
d	7.6	8.4 [†]	3.2	0.8	0.3	1
e	11.2	8.4 [†]	2.4	2.8	0.9	1
f	7.3	8.4 [†]	2.0	3.2	0.8	1
W49	12.0	11.4	2.2	4.2	1.2	2
W51	5.2	5.4	1.6	4.6	0.9	2
G010.472+00.026	3.8	10.8	2.1	1.5	0.4	2
G350.111+0.089	3.6	11.4	2.1	1.4	0.4	3
G351.774–00.537	27	17.4	4.8	0.9	0.6	3
G352.622–01.077	6.2	19.4	3.3	0.6	0.3	3

Table 3.2: Global properties of the sample of likely YMC progenitor gas clouds used in this work. The columns show mass (M), distance (D), radius (R), average volume number density (n), average column density (N_{H_2}) and the corresponding reference. [†]*Galactrocentric distance estimate from Reid et al. (2009a) – all Galactic centre clouds are assumed to be at this distance.* References: [1] Walker et al. (2015), [2] Ginsburg et al. (2012) and [3] Urquhart et al. (2013).

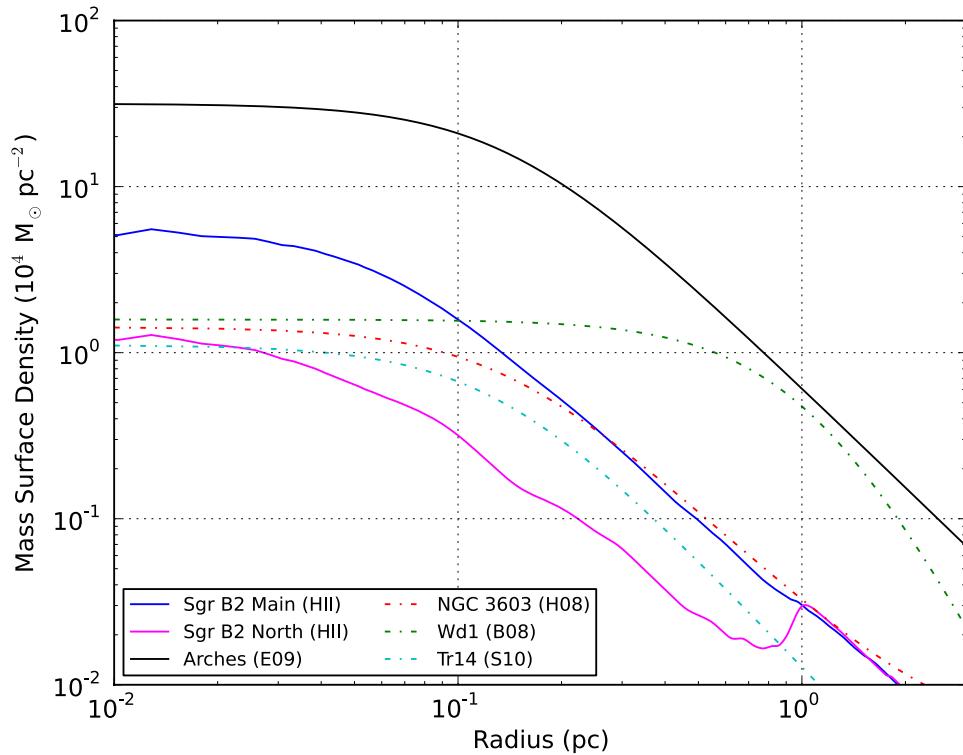


Figure 3.2: Enclosed mass surface density profiles as a function of radius for the (proto-)YMCs in the CMZ (solid lines) and in the Galactic disc (dashed lines). Note that the bump in the profile for Sagittarius B2 North at $R \sim 1$ pc is due to Sagittarius B2 Main entering the aperture.

Cluster	Age Myr	M $10^4 M_{\odot}$	D kpc	R_{core} pc	Σ_0 $10^5 M_{\odot} \text{pc}^{-2}$	Reference –
Sgr B2 Main	< 0.5	< 0.4	8.4	< 0.1	0.5	1
Sgr B2 North	< 0.5	< 0.4	8.4	< 0.1	0.12	1
Arches	2.0	2.0	8.4	0.14	3.5	2
NGC 3603	2.0	1.0 – 1.6	6.0	0.14	0.15	3
Trumpler 14	> 0.3	0.4 – 1.1	2.8	0.14	0.12	4, 5
Westerlund 1	3.0 – 5.0	2.0 – 4.5	3.6	1.1	0.17	6

Table 3.3: Global properties of the sample of Galactic YMCs used in this work. The columns show cluster age, mass (M), distance (D), core radius (R_{core}), central mass surface density (Σ_0) and the corresponding reference. References: [1] Walker et al. (2015), [2] Espinoza et al. (2009), [3] Harayama et al. (2008), [4] Sana et al. (2010), [5] Ascenso et al. (2007) and [6] Brandner et al. (2008).

is isothermal is unlikely to be valid in the highly star-forming clouds in the sample presented here. The energy injected into the gas via on-going star formation will cause these clouds to be internally heated. The effect of this will be to steepen their surface density profiles. The assumption of a single dust temperature is reasonable for the quiescent clouds in our sample, but less so for the star-forming clouds, where temperatures will be higher towards star-forming sites. Hence, any masses quoted are upper limits. The assumption of a constant gas-to-dust ratio of 100 may not be correct, and may be lower by a factor of ~ 2 towards the Galactic centre (Longmore et al., 2013a).

The result of these assumptions is that the steepness and mass-scaling of the profiles shown in Figure 3.1 are likely over-estimated. For example, assuming that the dust temperatures towards the star forming molecular cores are as high as 50 – 200 K (e.g. Cesaroni et al., 1994), this would result in a mass estimate that is $\sim 2.5 - 10$ times lower towards these small regions. Note that the uncertainties in the W49 mass profile are different from the dust derived measurements, since this measurement comes from the ratios of CO isotopologues. Galván-Madrid et al. (2013) found that the effect of a radially decreasing gas temperature acts opposite to the effect of saturation in the innermost pixels (see their appendix D).

Table 3.3 shows the general properties of the YMCs in the sample. They all have similar properties, in that they are all young ($\lesssim 2$ Myr), $\sim 10^4 M_{\odot}$ and have core radii of order 0.1 pc. Westerlund 1 is the exception here (see §3.4 for discussion).

These similarities are seen clearly in Figure 3.2, which displays their enclosed mass-surface-density profiles. Other than the differences in density and mass, all of the clusters (except Westerlund 1) have near-identical profile shapes, characterised by a prominent, compact central core region out to $R \sim 0.1$ pc.

Taking Figs. 3.1 and 3.2 and comparing them at face-value, it appears as though many of the clouds have equal or greater central mass surface densities when compared with the YMCs. This seems to suggest that perhaps some of these clouds could form a YMC at their current densities. However, note that the aforementioned assumptions regarding mass estimates place these as upper limits. Both the central surface densities and the slope of the gas profiles will likely be lower.

Comparing the *shape* of the profiles displays a general difference in the way that mass is distributed in YMCs and the clouds. Except in the case of Westerlund 1, the stars in the YMCs follow a comparatively simple, spherical Plummer-like distribution (Plummer, 1911). They have very compact central regions that are surrounded by much larger envelopes, which display a clear power-law drop-off in surface density beyond the core scale (~ 0.1 pc). In contrast, the molecular clouds have a much more uniform density over larger scales (i.e. no distinct central regions of high density). Their mass distribution is much more flat, with significant fall-off at radii approaching 1 pc. This flat profile does not imply a lack of sub-structure on smaller spatial scales. High spatial-resolution ALMA and SMA continuum data reveal that clouds like those in the dust ridge are highly sub-structured (e.g see Chapter 4 and Rathborne et al., 2015).

Figure 3.3 displays the enclosed mass as a function of radius for all of the clouds in the sample. Solid and dashed lines correspond to Galactic centre and disc clouds, respectively. To compare the data to simulations of monolithic, or ‘popping’ YMC formation, also plotted are the initial conditions from several simulations in the literature. The triangle markers correspond to the initial conditions used by Banerjee & Kroupa (2013) to simulate the monolithic formation of the R136 YMC. The circular markers correspond to the initial conditions used by Banerjee & Kroupa (2014) to simulate the monolithic formation of the NGC 3603 YMC. The star markers correspond to the initial conditions given in the fifth row of Table 1 in Assmann et al. (2011), in

which they simulate the ‘popping’ formation of massive clusters from very dense initial conditions. This particular set of initial conditions is chosen as they are quoted to be sufficient to form a $10^4 M_{\odot}$ cluster with a SFE $< 20\%$.

The N-body simulations of Banerjee & Kroupa (2013, 2014) assume a global cluster SFE of $\sim 33\%$, and so their initial conditions require that the gas mass once all of the stars in the cluster have formed ($t = 0$ in their simulations) is twice that of the initial stellar mass. They then evolve the system, and after a delay time (τ_d), the gas is then effectively removed from the system via an asymptotic fall in the gas mass, which occurs on a specific timescale (τ_g). This gas dispersal timescale is given by $\tau_g = R_h(0)/v_g$, where $R_h(0)$ is the initial half-mass radius and v_g is the average radial velocity of the gas. This velocity is taken to be the approximate sound speed in ionised hydrogen, which is $\sim 10 \text{ km s}^{-1}$ for a temperature of $\sim 10,000 \text{ K}$. The delay time is chosen to be 0.6 Myr . They reason that the typical initial half-mass radii of clusters are small – only a factor of a few larger than that typical of UCHII regions. Assuming that UCHII regions survive for $\sim 10^5$ years, then it would take a factor of a few times this lifetime to ionise the gas within $R_h(0)$. Both choices for τ_d and τ_g are fairly simplistic, and do not incorporate more thorough treatment of stellar feedback and its interaction with the gas. Nonetheless, they find that when they evolve the systems to roughly match the ages of the observed clusters, they are able to reproduce their present-day mass-surface-density profiles very closely.

While these models are able to reproduce the mass profiles of real clusters, this does not necessarily mean that their initial conditions are representative of the true initial conditions for YMC formation. Of particular interest for the comparison being made here are the initial compactness and radial distribution of the gas in these models, and how these compare to the known properties of Galactic YMC precursor clouds.

As these simulations are 3D models and the data are 2D projections, care must be taken to ensure that a fair comparison is being made. In Banerjee & Kroupa (2013, 2014), they present their initial conditions as initial cluster mass, initial gas mass and half-mass radius. They prescribe an equivalent half-mass radius to both the gas and the stars, which is calculated via the empirical relation given in Marks & Kroupa (2012), in

which $R_h(0) \propto M_{cl}^{0.13 \pm 0.04}$, where the mass of the cluster is prescribed to be consistent with the observationally-measured masses of the clusters. Using their assumed $\sim 33\%$ star-formation efficiency, these masses are combined to obtain the total gas mass prior to star formation. The following relation is used to convert the half-mass radius to the Plummer radius (Heggie & Hut, 2003) –

$$R_H = \frac{R_{pl}}{\sqrt{2^{2/3} - 1}}, \quad (3.1)$$

Assmann et al. (2011) already provide the Plummer radius. The total 3D gas mass for all of the models is then converted to a projected mass (Heggie & Hut, 2003) –

$$M(d) = M \left(1 + \frac{R_{pl}^2}{d^2} \right)^{-1}, \quad (3.2)$$

Fig. 3.3 shows that the initial projected masses within a given radius for these various models is generally too high, particularly at smaller radii. The Banerjee & Kroupa (2014) model for NGC 3603 appears consistent with observations at radii > 0.5 pc. However, it is over-dense on smaller spatial scales. Whilst the models generally predict mass surface densities that are greater than the observed clouds, this is not unambiguously the case. The highly star-forming clouds such as Sagittarius B2, W49 and W51 all lie very close to these models. Though it is worth reiterating that the mass estimates, particularly in the highly star-forming clouds, are upper limits. Accounting for temperature effects would create an even larger disparity between the observations and simulations. The simulated models also assume that both the gas and stars are initially distributed according to a spherical Plummer-like distribution, which is not globally true for the gas in the clouds in our sample (see §3.4). This is a critical difference between the true conditions in the ISM and those assumed in these models. The gravitational potential of the gas is dominant until a significant number of stars have

formed within the gas, and it is clear that the initial global gravitational potential does not arise from a Plummer-sphere distribution.

This comparison shows that while these N-body simulations of monolithically-formed clusters can broadly reproduce the observed properties of real YMCs, the initial conditions of the gas in such models are not consistent with the population of known Galactic YMC precursor clouds. However, it must be stated that this does not mean that a monolithic formation scenario can be ruled out, due to the small number of these simulations, their limited physics (i.e. feedback) and the limited range of parameters that they explore. More detailed simulations that explore a larger range of initial conditions, incorporate more realistic feedback physics and its interaction with the gas, and treat the gas in a more realistic manner (i.e. hierarchical in structure rather than a Plummer sphere), would permit comparisons that allow for stronger conclusions to be drawn. Though it is important to acknowledge that such a thorough treatment of massive cluster formation with detailed feedback physics is currently very expensive computationally.

3.4 Discussion

The previous chapter compared a sample of YMCs and possible YMC precursor clouds at the Galactic centre to attempt to distinguish between two commonly discussed modes of YMC formation – *popping* (monolithic) or *conveyor-belt* (hierarchical) modes. Through comparing the surface mass distributions of the clouds and YMCs, it should be possible to begin to distinguish between these two potential modes of YMC formation. If *popping* cluster formation is a common mode, we should expect to see YMC precursor gas clouds that are highly centrally-concentrated, more-so than the YMCs, such that once formed they may expand out to the observed YMC stellar densities as a result of residual gas expulsion. If the *conveyor-belt* route is instead a viable mode of YMC formation, we should expect to see gas clouds that are more extended than YMCs and that show evidence for sub-structure on smaller scales.

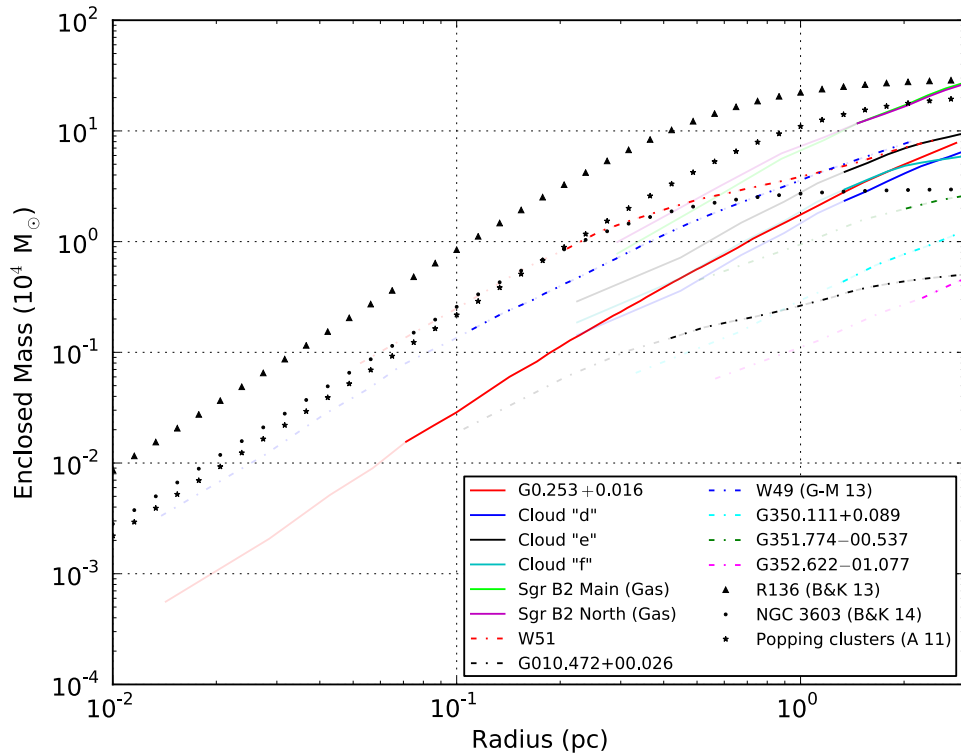


Figure 3.3: Enclosed gas mass profiles as a function of radius for the known potential Galactic YMCs precursors. The transition point from solid to lower opacity indicates the beam resolution of the data. The triangle markers correspond to the initial conditions used by Banerjee & Kroupa (2013) to simulate the monolithic formation of the R136 YMC. The circular markers correspond to the initial conditions used by Banerjee & Kroupa (2014) to simulate the monolithic formation of the NGC 3603 YMC. The star markers correspond to the initial conditions given in the fifth row of Table 1 in Assmann et al. (2011) to simulate a monolithically forming star cluster.

Cloud	$M_{R=0.1}$	30% SFE
	$10^3 M_{\odot}$	$10^3 M_{\odot}$
G0.253+0.016	0.29	0.09
W49	1.28	0.43
W51	2.71	0.90
Cluster		
Arches	6.6	–
NGC 3603	0.3	–
Trumpler 14	0.2	–
Westerlund 1	0.5	–

Table 3.4: Mass contained within a radius of 0.1 pc for the clouds (upper) and clusters (lower). The right column shows this with an assumed 30% global star formation efficiency (SFE) for the clouds.

In this previous work, it was found that in the Galactic centre, all of the candidate precursor clouds were more extended and less centrally-concentrated than the YMCs – seemingly consistent with a *conveyor-belt* formation mode being more likely. Now that this has been extended to include YMCs and potential YMC precursor clouds in the Galactic disc, the following sections discuss whether this conclusion holds true outside of the Galactic centre.

3.4.1 ‘Popping’ and ‘in-situ’ clusters – can Galactic clouds form a YMC at a high initial density?

Using the clouds for which high spatial-resolution data are available ($\lesssim 0.1$ pc), the mass contained within a radius of 0.1 pc – the typical core radius of the YMCs in the Galaxy – is estimated for both the clouds and the YMCs. This serves to assess whether these progenitor clouds contain enough mass on this scale to form a typical YMC stellar core at their present density distributions. The cluster core is by far the most dense region in these clusters, and so it follows that if they form in-situ, then the progenitors to such clusters should contain at least enough mass on the typical core scale such that they could form a stellar population that is at least as dense as the present-day populations in the central regions of Galactic YMCs.

The results are presented in Table 3.4. For the clouds, this mass is also adjusted for an assumed upper limit of 30% for the global star formation efficiency. Both W49 and W51 have comparable or greater central mass surface densities than NGC 3603, Trumpler 14 and Westerlund 1 at the typical core radius scale. This is also true for the highly star-forming Sagittarius B2 Main and North regions (Lu et al., in prep). In the largely-quiescent G0.253+0.016, the cloud does not yet contain enough mass on this scale to form even the least centrally-dense YMC in our sample (Trumpler 14). A similar result is also found for the quiescent Galactic centre clouds ‘d’, ‘e’ and ‘f’, which are also quiescent (Walker et al., submitted; see Chapter 4). It is also interesting to highlight that the core of the Arches cluster is considerably more dense than anything else in our sample. There are no known clouds in the Galaxy that would be capable of forming such a core in-situ.

These results suggest that in the *evolved, star-forming* clouds, within $\sim 10^5$ years since the onset of star formation, sufficient mass has accumulated such that they could form a typical YMC stellar core in-situ. In contrast, the quiescent clouds have not yet had time to build up a dense enough mass reservoir in their central regions. It must be cautioned that in the Galactic disc, there is over an order of magnitude scatter in the central mass concentrations in the gas clouds. The same is true for the YMCs across all environments. This, coupled with the limited sample size of Galactic YMCs and their potential progenitors, as well as the lack of high-resolution observations towards many of the clouds, makes it difficult to infer any significant evolutionary trends. Nonetheless, it can be stated unequivocally that for the known sample there are no clouds that contain *significantly* more mass than any known YMC in the central 0.1 pc. This is not compatible with a ‘*popping*’ formation scenario for YMCs, in which clusters form at initially higher densities, followed by a period of expansion due to gas expulsion. Instead, the apparent evolutionary trend from quiescent and less dense, to star-forming and more dense, suggests that we may be seeing evidence for a ‘*conveyor-belt*’ mode of YMC formation.

3.4.2 On the clumpy sub-structure of molecular clouds

As noted in §3.3, the simulations of monolithic cluster formation by Assmann et al. (2011) and Banerjee & Kroupa (2013, 2014) invoke Plummer-sphere initial morphologies for distribution of both the gas and the stars in the simulated clusters. Indeed, it is well established that the stars in YMCs are well described by Plummer models (or more generally, EFF-models; Elson et al. 1987). Whether the stars were *formed* according to this distribution, as per the ‘*popping*’ or ‘*in-situ*’ scenarios, is much less certain. Furthermore, the assumption that the gas follows a Plummer-like distribution is questionable, and inconsistent with what is typically seen in the interstellar medium (ISM), which is observed to have a hierarchical structure (e.g. Larson, 1981). Indeed, much of the data used in the sample for this chapter shows this. The ALMA observations of G0.253+0.016 reveal that it is highly sub-structured on small spatial scales (spatial resolution ~ 0.07 pc, Rathborne et al., 2015) and not at all Plummer-like. The same holds true for clouds in the solar neighbourhood, which are highly filamentary. Note that the radial surface density profiles of filaments within clouds have been shown to be well described by Plummer-like model (e.g. Arzoumanian et al., 2011), but this is only true locally ($R \sim 0.1$ pc), and does not apply to the larger scale clumps taken as a whole, as is the case with the profiles presented in this chapter.

Figure 3.4 shows the same mass surface density profile as given in Figure 3.1 for G0.253+0.016. Also plotted is a range of Plummer spheres, with core radii in the range of 0.5 – 2.0 pc. It is clear that, no matter the core radius, a Plummer sphere does not represent the distribution of gas in this cloud. SMA observations (resolution ~ 0.15 pc) of clouds ‘d’, ‘e’ and ‘f’ also reveal complex sub-structure (see next chapter; Walker et al., submitted). SMA observations of W49 (resolution ~ 0.1 pc) show that this region is also complex, with hierarchical structures and filaments (Galván-Madrid et al., 2013). Given a spatially-varying star-formation efficiency, it is possible that a Plummer-like stellar distribution could form from gas with a different distribution. Nonetheless, the models for monolithic cluster formation use Plummer-like profiles for the gas, and this is not seen in the observations.

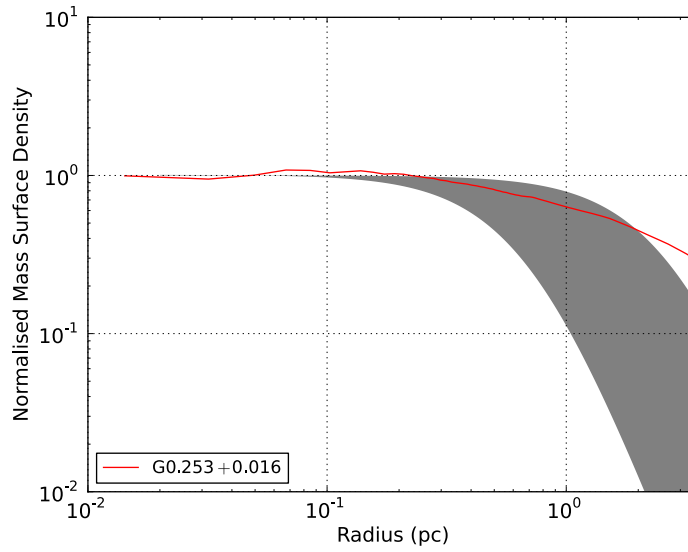


Figure 3.4: Mass surface density profile of G0.253+0.016. Shaded area corresponds to a range of Plummer spheres with core radii ranging from 0.5 – 2 pc.

It is not known what the nature of the small-scale structure is for the remainder of the clouds in this sample, and data with higher spatial resolution are required to address this. However, given that the structure of the aforementioned clouds, and the structure of the ISM is well-established, it is expected that they will follow a similarly complex, sub-structured distribution (i.e. not Plummer-like).

3.4.3 The peculiar shape of Westerlund 1

The stellar mass surface density profiles of the (proto-)YMCs displayed in Figure 3.2 are all extremely similar in shape. They are well characterised by a Plummer-like profile with a core radius of ~ 0.1 pc. It is clear, however, that Westerlund 1 does not fit this description. The cluster is much more extended than the others in our sample, with a core radius of ~ 1.0 pc, almost an order of magnitude larger than the core radii of the other YMCs. This ‘bloated’ appearance is further complicated by a reported elongation that is characterised by an axial ratio of 3:2 (Gennaro et al., 2011). The source of this extended morphology is not known. However, Gennaro et al. (2011) propose that it may be a result of merging of two or more stellar sub-clusters that formed in the same natal gas cloud. They reason that if this happened recently, the cluster may not yet have had time to dynamically relax and that eventually, this elongated cluster will settle into a more typical spherical distribution. If true, this may support the idea that a spherical,

centrally-condensed cluster results through the merging of sub-clusters, as proposed in *hierarchical merging* scenarios for YMC formation. A corollary of this scenario is that all other YMCs in this sample have undergone violent relaxation. Irrespective of the core radius, all YMCs including Westerlund 1 display central surface densities similar to the proposed universal maximum surface density of $\Sigma_* \sim 10^5 \text{ M}_\odot \text{ pc}^{-2}$ observed in dense stellar systems over 7 orders of magnitude in stellar mass (Hopkins et al., 2010).

3.5 Conclusions from Walker et al. (2016)

A comparison of the enclosed mass as a function of radius and the internal structure of the sample of known Galactic YMCs and their likely progenitor gas clouds is made. It is found that there are no known clouds with significantly more mass in their central regions than the known Galactic YMCs. The observations also show that the quiescent, less evolved clouds contain less mass in their central regions than the highly star-forming regions. This suggests an evolutionary trend in which clouds continue to accumulate mass towards their centres after the onset of star formation – consistent with a ‘*conveyor-belt*’ mode of YMC formation.

When compared with simulations for monolithic ‘*popping*’ formation of YMCs, it is found that the initial conditions for the cluster-forming clouds are not wholly consistent with the observations – in general, they require more mass at a given radius than is observed in the known YMC precursor clouds. Furthermore, the initial morphology of the gas in both these simulations and the general model for monolithic formation for YMCs is inconsistent with the observed morphology of YMC precursor clouds. They require initially Plummer-like, highly centrally-concentrated clouds – whereas the clouds in the sample presented here (for which high spatial resolution data are available) display complex, hierarchical sub-structure and do not display the prominent cores and power-law tails of Plummer profiles. It is therefore concluded that a ‘*popping*’ formation scenario for YMCs is not consistent with the data that is currently available for Galactic YMCs and their likely precursor gas clouds. Instead, the data suggest that for the highly star-forming clouds, an ‘*in-situ*’ formation mode

seems plausible. Coupled with the lower central densities of the quiescent clouds, this suggests a ‘*conveyor-belt*’-like mode of YMC formation, whereby clouds contract and accumulate more mass in their central regions along with concurrent star formation.

Chapter 4

Star formation in a high-pressure environment: An SMA view of the Galactic Centre dust-ridge

Preface

The work presented in this chapter is based upon that of Walker et al., (submitted). I led this work as first author, and all of the contents (text, analyses, figures, tables) are my own. I reduced, imaged and analysed all of the SMA data presented in this chapter. The data that were used for this work were taken as part of a larger survey with the SMA (*CMZoom*). I also spent considerable time reducing data for the wider survey as part of the team responsible for data calibration. At the request of the survey PIs, I also developed an imaging pipeline that is being used to obtain data products from the entire survey, as well as to prepare the data for eventual public release. A more detailed overview of the data calibration and imaging is given in Appendix A of this thesis.

4.1 Introduction

This chapter presents high angular resolution observations of the Galactic centre dust ridge clouds from the Submillimeter Array Legacy Survey of the Central Molecular Zone (*CMZoom*¹, PIs: Eric Keto and Cara Battersby, see Battersby et al. 2017), the details of which are discussed in section § 4.2, along with a discussion of the complementary single-dish data that is used to recover the large scale emission that is filtered out by the interferometer. Section § 4.3 presents the analysis of the dust continuum and a select few molecular lines, which are used to determine the number of dense cores embedded within the clouds along with their general properties such as masses, radii, gas temperatures, line-widths and virial ratios. The results of this analysis are presented in Table 4.3. Section § 4.4 compares the properties of the dense cores that have been identified in the CMZ with those of cores in the less extreme environment of the Galactic disc to investigate any potential effects these differing environmental conditions may have on the embedded core populations of molecular clouds. The conclusions and implications of this study are presented in sections § 4.4 and § 4.5. The analysis of the molecular line data and methodology of the gas temperature modelling are given in an appendix.

4.2 Observations & Data

4.2.1 *CMZoom* – An SMA Legacy Survey of the Central Molecular Zone

In an effort to understand the physical, chemical and kinematic properties of the dense structure in the CMZ, a large legacy survey (*CMZoom*, Battersby et al. 2017) of the region has been performed with the Submillimeter Array (SMA). The survey consists of ~ 500 hours worth of mapping, corresponding to ~ 240 arcmin² of the CMZ at 230 GHz (1.3 mm). The survey was designed to target all regions within the CMZ that lie

¹More details of this survey can be found at <https://www.cfa.harvard.edu/sma/LargeScale/CMZ/>

Cloud	Mass $10^4 M_{\odot}$	Radius pc	n 10^4 cm^{-3}	Reference
b	1.3	1.9	0.7	2
c	1.8	1.9	0.9	2
d	7.6, 7.2	3.2, 3.4	0.8	1, 2
e	11.2, 15.3	2.4, 4.5	2.8	1, 2
f	7.3, 7.2	2.0, 2.7	3.2	1, 2

Table 4.1: Masses, radii and mean number densities (assuming spherical geometry) of the dust ridge clouds that have been observed with the SMA as part of the larger survey. The relevant references for these quantities are also given. References: (1) Walker et al. (2015) and (2) Immer et al. (2012).

above a column density threshold of $\gtrsim 10^{23} \text{ cm}^{-2}$. The typical spatial resolution of this survey is $\sim 4''$ (0.16 pc at a distance of 8.4 kpc) and the spectral resolution is $\sim 1.1 \text{ km s}^{-1}$.

The dust-ridge clouds from ‘b – f’ (see Table 4.1 for cloud properties) were observed in the compact array configuration between the 24th May – 6th June 2014, and in the subcompact configuration between the 25th – 27th July 2014 (see Table 4.2 for more details of the observations). Cloud ‘a’ (G0.253+0.016) was not observed, as it is well-studied and high-resolution data already exist (Kauffmann et al., 2013a; Johnston et al., 2014; Rathborne et al., 2014b, 2015). Typical RMS continuum sensitivity achieved is $\sim 3 - 5 \text{ mJy beam}^{-1}$. Figure 4.1 shows a 3-colour image of the dust-ridge, where white circles correspond to the primary beam coverage of the SMA observations.

Data calibration was performed using MIR², edge channel flagging and continuum and line separation was done using MIRIAD (Sault et al., 1995) and all subsequent imaging and analysis was performed using CASA (McMullin et al., 2007). See Appendix A of this thesis for more details regarding these steps.

Once calibrated and prepared for imaging, the relevant compact and subcompact tracks for each dust ridge cloud were concatenated in CASA and both the continuum and line data were imaged using the CLEAN algorithm, which is the most common deconvolution algorithm employed in radio astronomy. CLEAN works in an iterative manner

²MIR is an IDL-based package that has been developed to calibrate SMA data. The MIR package and cookbook can be found at <https://www.cfa.harvard.edu/~cqi/mircook.html>.

to locate the maximum intensity pixel in the dirty image, the location of which is assigned as a clean component and is added to the model. This is then convolved with the dirty beam and subtracted from the dirty image. This is repeated until some defined threshold criteria are reached (e.g. number of iterations, RMS-based flux threshold). A final cleaned image is generated via the convolution of the model image and the clean beam (typically Gaussian with dimensions of the synthesised beam), which is added to the residual noise map.

Although the clouds were observed in both compact and subcompact configurations, the data still suffer from the inherent limited flux recovery due to the incomplete uv -coverage of the interferometer. To account for this, the most appropriate single-dish data have been obtained for combination with the interferometric data.

To recover the continuum emission from these clouds, data from the Bolocam Galactic Plane Survey (BGPS, Rosolowsky et al., 2010; Aguirre et al., 2011; Ginsburg et al., 2013) are used. These data are at a wavelength of 1.1 mm and provide an angular resolution of $33''$ (~ 1.3 pc at a distance of 8.4 kpc) and resolve a largest angular scale of $\sim 120''$ (Ginsburg et al., 2013). Ideally, single-dish observations that were taken at 1.3 mm (the wavelength of the SMA data) would be used. Given that the single-dish observations are at 1.1 mm, the data must be scaled to estimate the flux that would be observed at 1.3 mm, which is determined by taking the ratio of the fluxes (S_ν) at each wavelength, with an assumed emissivity index of $\beta = 1.75$. The *feather* task in CASA is used when combining the BGPS data with the cleaned SMA data. Any discussion regarding the dust continuum hereafter refers to results obtained using fully combined maps of compact, subcompact and single-dish data.

For the molecular lines, data from a recent survey of the CMZ performed using the Atacama Pathfinder EXperiment (APEX) telescope are used (Ginsburg et al., 2016b). The method³ used to combine the single-dish and interferometer line data are somewhat more involved than for the case of the continuum. First the APEX data are formatted correctly such that they are gridded to the same axes as the SMA data. A first iteration of CLEAN is performed with the APEX data as a model, the output of which is then

³<http://tinyurl.com/zero-spacing>

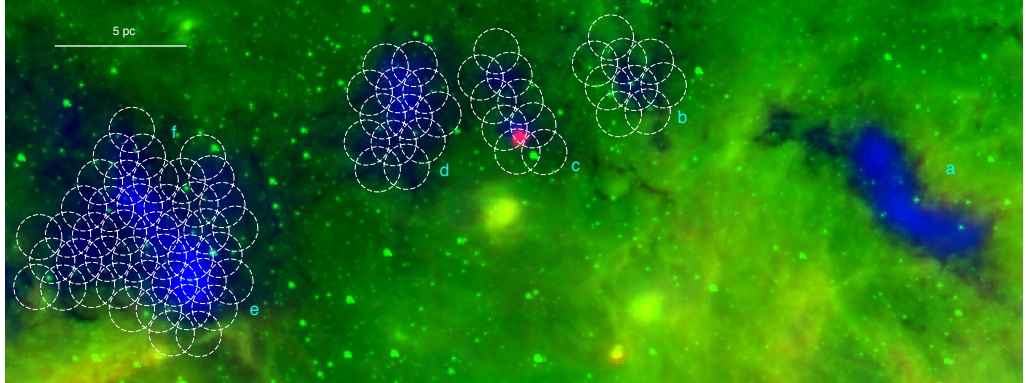


Figure 4.1: Three-colour image of the ‘dust-ridge’ at the Galactic centre. Green: $8\ \mu\text{m}$ data from the Spitzer/GLIMPSE survey (Churchwell et al., 2009). Blue: the column density map from the HiGAL survey (Molinari et al., 2010; Battersby et al., 2011, range displayed is $\sim 5 - 55 \times 10^{22}\ \text{cm}^{-2}$). Red: Herschel $70\ \mu\text{m}$ emission. White circles correspond to the primary beam coverage of the SMA observations.

Cloud	Central coordinates	Resolution (")	N_{pntg}	N_{ant}	T_{obs} (hours)	RMS (mJy beam^{-1})
b	G0.340+0.055	3.18×3.13	9	7	2.36	2–3
c	G0.380+0.050	3.15×3.10	9	7	2.30	2–5
d	G0.412+0.052	3.19×3.08	13	7	3.04	3–5
e/f	G0.489+0.010	3.04×2.93	44	7	11.35	2–6

Table 4.2: Details of the SMA observations of dust ridge clouds b – f. All clouds were observed using the ASIC correlator with a total bandwidth of 8 GHz, between 217.05 – 232.83 GHz. Spectral resolution is $1.1\ \text{km s}^{-1}$ in all cases.

used to create an updated model image. This updated model image is then used in a final iteration of CLEAN to produce the combined data cube.

4.3 Results

4.3.1 1.3mm Continuum Emission

Figure 4.2 displays the individual 1.3 mm continuum maps for each of the clouds, overlaid as black contours on top of Herschel column density maps (blue). Dense substructure is clearly detected in each of these clouds. In order to describe this substructure in a systematic way, dendrograms are produced (see e.g. Rosolowsky et al.,

2008) for each of the clouds using the ASTRODENDRO⁴ software package. To do this, a threshold of 5σ and an increment of at least 2σ between structures are used (see Table 4.2 for RMS estimates). The minimum number of pixels required is specified as –

$$N_{pix}(min) = \frac{2\pi\theta_{maj}\theta_{min}}{8\ln(2)A_{pix}} \quad (4.1)$$

where θ_{maj} and θ_{min} are the major and minor axes of the synthesised beam and A_{pix} is the pixel area. For example, for respective values of $3.2''$, $3.1''$ and $1''^2$, we obtain $N_{pix}(min) \sim 11$ pixels for the observation of dust ridge cloud ‘c’.

A total of 15 independent cores are detected throughout clouds ‘b – f’. These are shown as red contours in Figure 4.2. These cores, along with their estimated fluxes, effective radii (R_{eff}), positions and masses are given in Table 4.3. ASTRODENDRO calculates the radius by taking the geometric mean of the major and minor axes of the projection onto the position-position plane, computed from the intensity-weighted second moment in the direction of elongation. However, the ellipses that are fitted to the cores often appear to underestimate the radius. Instead, the total area of each core is used here to calculate the effective radius of a circular source with an area equal to that of the core. The difference between these radii can be as large as 30 – 40%. Any radius estimates are therefore upper limits.

The masses of the cores are determined in the same way as for the clouds in the previous chapters (see Equations 2.1 – 2.3). Besides the uncertainty of the gas-to-dust ratio in the CMZ, the only other parameter in Equation 2.3 that remains unconstrained is the dust temperature towards these cores. At present, the temperature of the dust on the scales that we are probing with our SMA observations ($\sim 4''$) is not known. The best measure of the dust temperature is from the HiGAL survey (Molinari et al., 2010, temperature estimates by Battersby et al. 2011). This provides dust temperatures that are typically ~ 20 K in these clouds on $33''$ scales. This dust temperature is assumed

⁴ASTRODENDRO is a Python package designed to compute dendrograms of astronomical data and can be found at <http://www.dendrograms.org/>.

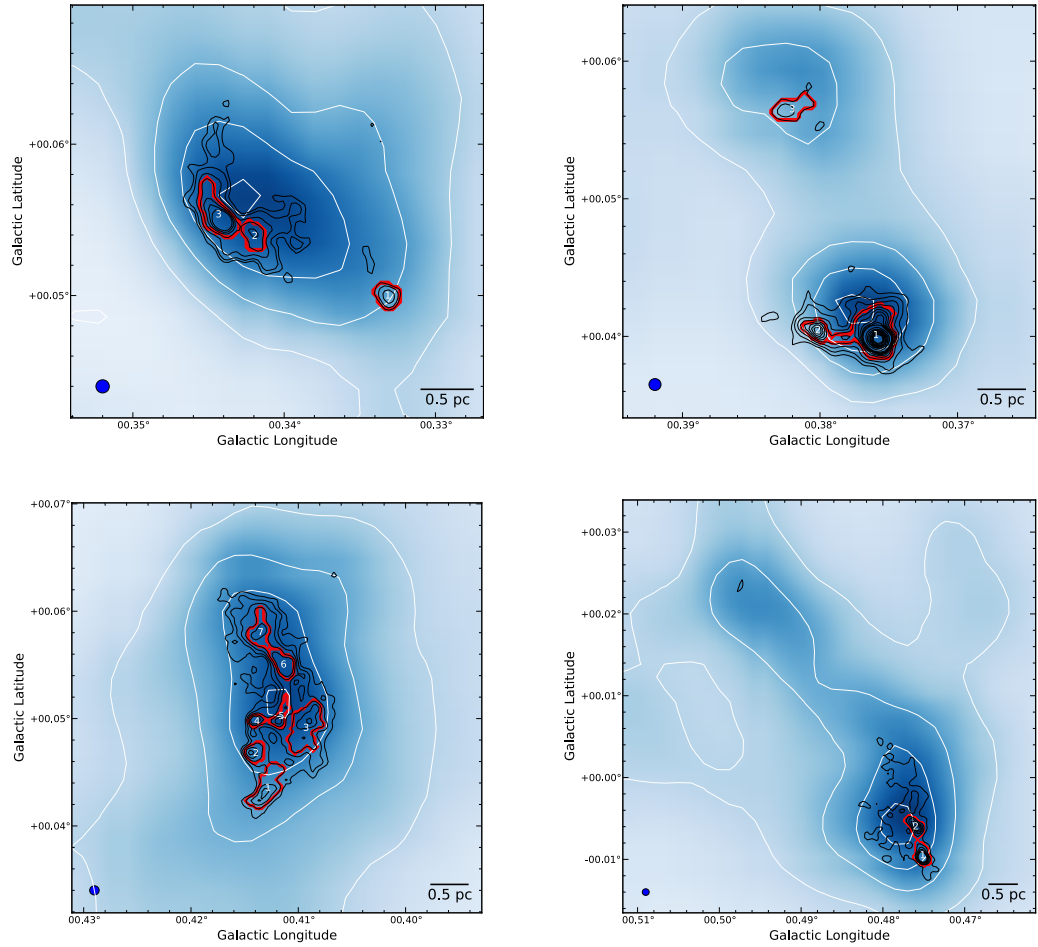


Figure 4.2: *Top*: dust ridge clouds ‘b’ (*left*) and ‘c’ (*right*). *Bottom*: dust ridge clouds ‘d’ (*left*) and ‘e/f’ (*right*). Background image is a Herschel column density map, shown with corresponding white contours. Black contours show the 230 GHz continuum emission as seen with the SMA at the $5\text{-}\sigma$ level. They are $10 - 32$, $16 - 32$, $16 - 460$ and $20 - 72$ mJy beam^{-1} for clouds b, c, d and e/f, respectively. The synthesised beam is shown in the lower left of each panel. Red contours highlight the cores as determined via dendrogram analysis.

to provide an upper limit to the masses of these cores. This is an upper mass limit due to the fact that a decrease in temperature results in an increase in the measured mass, as can be seen in Equation 2.3. It is expected that the gas and dust may be internally heated towards some of these cores, which would consequently drive the mass estimates down. Though it is also possible that a quiescent embedded core with no internal heating may be even colder than the gas on larger scales due to being heavily shielded from external heating sources.

Assuming this dust temperature of 20 K, the cores have upper mass limits ranging from $\sim 50 - 2150 M_{\odot}$ within radii of $\sim 0.1 - 0.25$ pc (see Table 4.3) and have volume densities $\sim 10^6 \text{ cm}^{-3}$. As previously discussed, these are likely upper mass limits. The following section discusses the molecular line emission, and how this is used to determine gas temperatures and infer lower mass limits for the cores.

4.3.2 Molecular Line Emission

Currently, only a lower limit is known for the dust temperature from Herschel observations (~ 20 K on $33''$ scales). It is known that on these larger scales, the gas and dust temperatures in the CMZ are not thermalised and that the gas temperatures are typically higher (see e.g. Ao et al., 2013; Johnston et al., 2014; Ginsburg et al., 2016b; Immer et al., 2016). However, it is possible that the gas and dust may begin to thermalise at high volume densities. Clark et al. (2013) show this in Figure 4.3 of their paper, in which they model the temperature of the gas and dust as a function of volume density, showing that they begin to couple at densities $> 10^6 \text{ cm}^{-3}$ and converge at $> 10^7 \text{ cm}^{-3}$. Their models assume cosmic ray ionisation rates and interstellar radiation fields in the CMZ that are much higher than those measured in the local interstellar medium. For more typical, local conditions, the gas and dust would be expected to couple at lower densities, $\sim 10^4 \text{ cm}^{-3}$ (e.g. Goldsmith & Langer, 1978; Galli et al., 2002).

The cores that are presented here are at volume densities of $\sim 10^5 - 10^6 \text{ cm}^{-3}$, based on their upper-limit mass estimates. It therefore follows that by estimating the temper-

Source	Enclosed Flux (Jy)	R_{eff} (pc)	Δl (")	Δb (")	$M_{T_{20}}$ (M_{\odot})	$\langle T_{gas} \rangle$ (K)	$M_{T_{gas}}$ (M_{\odot})	ΔV (km s^{-1})	α_{vir}
G0.340+0.055									
b1	0.03	0.12	23.53	-18.92	51	-	-	-	-
b2	0.05	0.12	-8.15	-4.80	78	-	-	-	-
b3	0.17	0.19	-16.75	0.46	251	-	-	-	-
G0.380+0.050									
c1	1.45	0.26	13.56	-36.73	2143	243.7 ± 18.2	136^{+11}_{-10}	5.1 ± 0.2	$0.7 - 10.5$
c2	0.16	0.12	-1.95	-35.12	236	< 56.7	> 68	$5.4 \pm 0.6 - 6.0 \pm 0.5$	$3.1 - 13.3$
c3	0.09	0.15	-7.92	22.97	135	-	-	-	-
G0.412+0.052									
d1	0.19	0.22	-5.24	-32.10	285	-	-	-	-
d2	0.08	0.13	-8.67	-19.62	119	86.3 ± 20.4	22^{+7}_{-4}	$4.2 \pm 0.3 - 5.0 \pm 0.3$	$4.0 - 30.9$
d3	0.31	0.26	8.51	-11.39	455	-	-	-	-
d4	0.05	0.09	-8.03	-8.94	71	-	-	-	-
d5	0.07	0.12	-0.70	-9.05	109	-	-	-	-
d6	0.16	0.16	1.05	10.16	239	< 56.7	> 69	$5.4 \pm 0.5 - 6.3 \pm 0.4$	$4.1 - 19.0$
d7	0.15	0.17	-6.74	21.30	225	-	-	-	-
G0.489+0.010									
e1	0.30	0.16	48.55	-71.03	445	> 150	< 46	$5.4 \pm 0.6 - 7.8 \pm 0.6$	$2.1 - 44.1$
e2	0.22	0.15	45.57	-58.27	325	-	-	-	-

Table 4.3: The above table displays the dust cores that have been identified using the dendrogram analysis. For each cloud, the table lists the cores identified, along with the enclosed flux, effective radius (R_{eff}), central co-ordinates as offsets (Δl , Δb , with respect to central coordinates given in the first column) and the core mass assuming a dust temperature of 20 K ($M_{T_{20}}$). Where possible, we also provide the spatially-averaged gas temperature (see §3.2), core mass assuming a dust temperature equal to the gas temperature ($M_{T_{gas}}$), line-width of H_2CO (ΔV) and the virial ratio (α_{vir}). Provided are two measures of the line-width – one with and one without the inclusion of single-dish data. All calculations assume a gas-to-dust ratio of 100 and a distance of 8.4 kpc (Reid et al., 2009a, 2014).

ature of the *gas*, this can be used to provide strong upper limits for the *dust* temperature and hence lower limits for the core masses. However, note that based upon the models of Clark et al. (2013), there may still be a difference between the gas and dust temperatures at these densities of several factors. Thus, any mass estimates made this way are likely extreme lower limits.

For the purposes of this work, the following molecular lines that were covered in the SMA bands are studied – the triplet of lines from the para-H₂CO (Formaldehyde) transitions at 218.22219 (3_{0,3}-2_{0,2}), 218.47563 (3_{2,2}-2_{2,1}) and 218.76007 (3_{2,1}-2_{2,0}) GHz as well as the J=12-11 k-ladder of CH₃CN (Methyl Cyanide). These transitions are chosen as their emission lines can be used as a thermometer to estimate the temperature of the gas from which they are emitted (see e.g. Ao et al. 2013; Johnston et al. 2014; Ginsburg et al. 2016b; Immer et al. 2016 for H₂CO temperature measurements in the CMZ and Longmore et al. 2011 for CH₃CN temperature measurements towards a high-mass star forming region). A more detailed description of how these transitions are used for estimating temperatures is presented in the appendix of this chapter.

Of the 15 cores detected with the SMA, measurement of the gas temperature was possible for five of them. The remainder either had poor signal-to-noise or non-detection. Table 4.2 gives the estimated gas temperatures ($\langle T_{gas} \rangle$), which has been averaged over the spatial extent of each core, as specified by their measured radii. This is then assumed to act as a proxy for the average dust temperature, and core masses are recalculated in the same way as in the previous section ($M_{T_{gas}}$). A varying degree of gas temperatures is found in the cores, from ~ 57 K up to > 240 K. Assuming equivalent dust temperatures has a substantial effect on the mass estimates, decreasing by as much as 94% in the most extreme case.

Though this provides strong lower-mass estimates for the cores, the significant variation in estimated mass highlights the need for accurate estimates of the dust temperature on these small spatial scales. The de-coupled nature of the gas and dust temperatures in the CMZ makes this difficult observationally. Radiative transfer modelling of the dust and line emission is required such that the volume densities of these cores can be accurately determined. The density can then be compared with numerical models

of the thermal coupling of the gas and dust in the CMZ as a function of volume density (see e.g. Figure 3 of Clark et al. 2013). However, the necessary line data to do this are not currently available for these cores. The ratio of the $(3_{2,1}-2_{2,0})/(3_{0,3}-2_{0,2})$ lines of H_2CO , which are used as a primary temperature diagnostic here, often exceeds that which can be reliably fit by any models at high volume density (see appendix). Thus, only lower limits for the gas temperature can be quoted in such cases.

The line-widths obtained from the line-fitting are used to investigate whether the cores are likely to be gravitationally bound. To do this the virial parameter is calculated via $\alpha = 5R\sigma^2/GM$, (where $\sigma = \Delta V/2\sqrt{2\ln(2)}$, ΔV is the line-width and $\alpha \lesssim 2$ typically indicates gravitationally bound) for both the upper and lower mass estimates. Two values for the line-width (ΔV) are used. These two values come from fitting the H_2CO lines with and without single-dish data added. The single-dish APEX data are sensitive to the larger scale emission in these clouds, which is known to display very broad line-widths ($10 - 20 \text{ km s}^{-1}$). This means that in general, the single-dish combination tends to broaden the lines. For the purposes of estimating whether or not the cores may be gravitationally bound, it is not clear that including the single-dish data makes sense. Both values for ΔV are therefore given, and used to estimate upper and lower limits for α .

Of the five cores for which H_2CO is well detected, only two of them, ‘c1’ and ‘e1’, have $\alpha \lesssim 2$ based on their upper mass limits. The other three cores have $\alpha \sim 3 - 4$, suggesting that they may neither be strongly bound or unbound. Though the cores are of high-mass and compact, they do not appear to be strongly sub-virial as a result of their large line-widths of $\sim 5 \text{ km s}^{-1}$. Re-calculating α with the lower mass and larger line-width estimates puts it at much higher values, up to as large as 44, suggesting that they are unbound. However, these are extreme lower limits for the mass and upper limits for the line-width. This further reinforces the need for more accurate dust temperatures on the scale of these cores.

Kauffmann et al. (2016a,b) present a survey of molecular clouds in the CMZ, and conclude that objects on the scale of the cores presented in this chapter ($\sim 0.1 \text{ pc}$) in their sample have typical virial ratios of $\lesssim 2 - 3$, and should therefore be close to being

gravitationally bound. This is broadly consistent with the lower values presented here, based upon upper mass limits. The line-widths that are estimated here are typically larger than those in the Kauffmann et al. (2016a,b) sample, though this may be a result of the choice of molecular line tracer, as they use N_2H^+ , not H_2CO . Further studies of the line emission from all of these cores, as well as those discovered in the wider *CMZoom* survey, will provide a more detailed insight as to whether this difference is a real one, or whether it is dependent upon the choice of tracer.

4.4 Discussion

4.4.1 Young precursors to high-mass stars?

As explained in the introduction to this thesis (§1), these dust-ridge clouds are intriguing in that their density lies at or above the threshold of density-dependent star formation relations ($\sim 10^4 \text{ cm}^{-3}$, Lada et al. 2010a), yet they are devoid of widespread star formation (Longmore et al., 2013a). Clouds with similar global properties in the less extreme environment of the Galactic disc are all forming stars prodigiously (see e.g. Ginsburg et al., 2012; Urquhart et al., 2013). This raises the question – if star formation is being inhibited at these densities in the CMZ and pushing the critical density for star formation up to higher values, will these clouds ever form stars/clusters? Indeed, this has already been a subject of debate regarding G0.253+0.016 (cloud ‘a’, see e.g. Longmore et al., 2012; Kauffmann et al., 2013a; Johnston et al., 2014; Rathborne et al., 2014b).

Whether or not these clouds will form stellar clusters is still uncertain, but it is known that star clusters have recently formed in the CMZ (e.g. the Arches and Quintuplet) and that clusters are currently forming there (e.g. Sagittarius B2). It is also predicted that the environmental conditions in the CMZ should lead to a higher fraction of stars forming in bound clusters (Kruijssen, 2012). These (proto-)clusters must have an earlier, quiescent phase, prior to the onset of widespread star formation. To date, these

dust-ridge clouds are some of the best candidates for such a phase in the CMZ. If these clouds are precursors to such clusters, then they are also expected to contain the precursors to high-mass stars. The SMA observations presented here reveal 15 dense, high-mass cores within these clouds that may be the potential formation sites of high-mass stars and sub-clusters.

Of these 15 detected cores, 13 are quiescent (i.e. they do not coincide with any known star formation tracers). This was determined by searching the literature and data archives for water and methanol masers, $24\ \mu\text{m}$ and $70\ \mu\text{m}$ emission and HII region detection. Detailed analysis of the molecular line data is required to determine the fate of these cores. Based on the analysis presented here, the properties of the star-forming and the quiescent cores derived from the SMA continuum and line data are similar in terms of their masses, sizes, densities and line-widths, suggesting that they all have the capacity to form stars. In this case, they could represent different evolutionary phases of the same type of object. The estimated ranges of the virial ratio (see Table 4.3) would suggest that some of the cores are unbound and will therefore not form stars. However, these are highly uncertain due to the lack of constraints on the dust temperature. It is also possible that some of the cores may be unbound on the scales probed by the SMA observations, but that smaller scale structure (i.e. on which individual stars form) within the cores could be gravitationally bound.

The two other cores – ‘c1’ and ‘e1’ – show signs of star formation activity. ‘e1’, situated towards the south of cloud ‘e’, has the second highest peak brightness of all 15 cores ($\sim 0.12\ \text{Jy beam}^{-1}$) and has a mass in the range of $\sim 46 - 445\ M_{\odot}$ within a radius of 0.16 pc. This source coincides with weak $70\ \mu\text{m}$ emission as seen with Herschel and both H_2O and CH_3OH Class II maser emission (Caswell et al., 2010a).

‘c1’, situated towards the south of cloud ‘c’, has the highest peak brightness in the sample ($\sim 0.6\ \text{Jy beam}^{-1}$) and has a mass in the range of $\sim 136 - 2143\ M_{\odot}$ within a radius of 0.26 pc. This source also coincides with strong $70\ \mu\text{m}$ emission as seen with Herschel and both H_2O and CH_3OH Class II maser emission (Caswell et al., 2010a). Additionally, this core coincides with H_2CO and SiO maser emission – both of which are extremely rare in star-forming regions in the Galaxy (Ginsburg et al., 2015).

Thus far, only eight H₂CO masers have been identified in the Galaxy, all of which are associated with high-mass star formation. Even more rare are SiO masers. They are commonly detected towards evolved stars, but only rarely towards star-forming regions, and then only in regions of known high-mass star formation (Zapata et al., 2009a). Thus far, only five SiO masers have been identified towards such regions in the Galaxy. Furthermore, H₂CO and SiO masers have only been detected together towards two regions – Sagittarius B2 and ‘c1’ – both of which are in the CMZ. This may also suggest something different about the star formation and/or chemistry in the CMZ.

Given the spatial coincidence of a number of star formation tracers towards both cores ‘c1’ and ‘e1’, it is concluded that they are very likely to be sites of active high-mass star formation. Furthermore, there have been no UCH_{III} regions detected towards them, as revealed by deep VLA observations (Immer et al., 2012). Any star formation must therefore be at a very early stage, before the high-mass star has ‘switched on’. Thus, embedded within these cores may be the initial, largely-unperturbed conditions from which high-mass stars form. Targeting these sources at higher spatial resolution and with line surveys will provide valuable insight into how high-mass stars form in the CMZ. I am currently leading multiple on-going ALMA projects to follow-up these cores along with others presented in this paper at much higher spatial resolution (< 0.1'', PI: D. Walker, see Chapter 5).

4.4.2 Do the properties of high-mass cores vary with environment?

In §1 it was highlighted that these high-mass CMZ clouds are vastly under-producing stars when compared to clouds with similar properties in the less extreme environment of the Galactic disc. Recent theoretical models indicate that the CMZ environment drives high turbulent pressure in CMZ clouds. These models predict that the CMZ is undergoing episodic cycles of bursty star formation and quiescence (Kruijssen et al., 2014; Krumholz & Kruijssen, 2015; Krumholz et al., 2016). This heightened turbulent energy density can be seen observationally, evidenced by the comparatively large

line-widths of $\sim 10 - 20 \text{ km s}^{-1}$ seen towards these clouds on parsec scales (Oka et al., 2001; Walker et al., 2015; Henshaw et al., 2016). So it is known that on large spatial scales, the gas in the CMZ looks different to that in the Galactic disc in that it is generally orders of magnitude more dense and typical line-widths are an order of magnitude larger – similar to the conditions seen in high-redshift galaxies (Kruijssen & Longmore, 2013). But how do the properties of the small-scale, dense structures (i.e. cores) compare to those in the disc of the Galaxy?

To compare the properties of cores in the Galactic disc and centre, the sample of high-mass proto-stellar cores in Peretto et al. (2013) are taken, where they compiled a list of masses and radii for a sample of high-mass proto-stellar cores in the Galactic disc (Figure 6 in Peretto et al. 2013). Also used are the sample of high-mass proto-stellar cores given in Table 2 of Louvet et al. (2014) for their data on the W43–MM1 ridge, which is a likely precursor to a ‘starburst cluster’, along with those for several other regions present in the literature. The masses of the cores are scaled such that they are consistent with the spectral index of $\beta = 1.75$ that has used for mass estimates in the analysis of the SMA cores.

Fig. 4.3 displays the data from the SMA dust ridge cores and the cores from disc clouds. The plot shows that the high-mass cores in the CMZ fit within the mass-radius relation of those in the disc reasonably well – i.e. they are not distinctly separated. However, the cores in the SMA sample are best described by lower volume densities of a few $\times 10^5 - 10^6 \text{ cm}^{-3}$, while many of the disc sources are at higher volume densities. This is likely an effect of the spatial resolution of the SMA data, and more compact fragments in these cores could approach the densities seen in regions of high mass star formation. Initial inspection of on-going ALMA observations of some of these dust ridge cores indicate that this is indeed the case (see Chapter 5). The grey shaded region in Fig. 4.3 corresponds to the empirical massive star formation threshold that was proposed by Kauffmann & Pillai (2010). Based upon a study of a sample of Galactic molecular clouds, they determine an approximate threshold for massive star formation to occur as $-M(R) \gtrsim 870M_{\odot} \times (R/\text{pc})^{1.33}$. All of the sources are at or above this threshold, which in the context the proposed scenario would suggest that

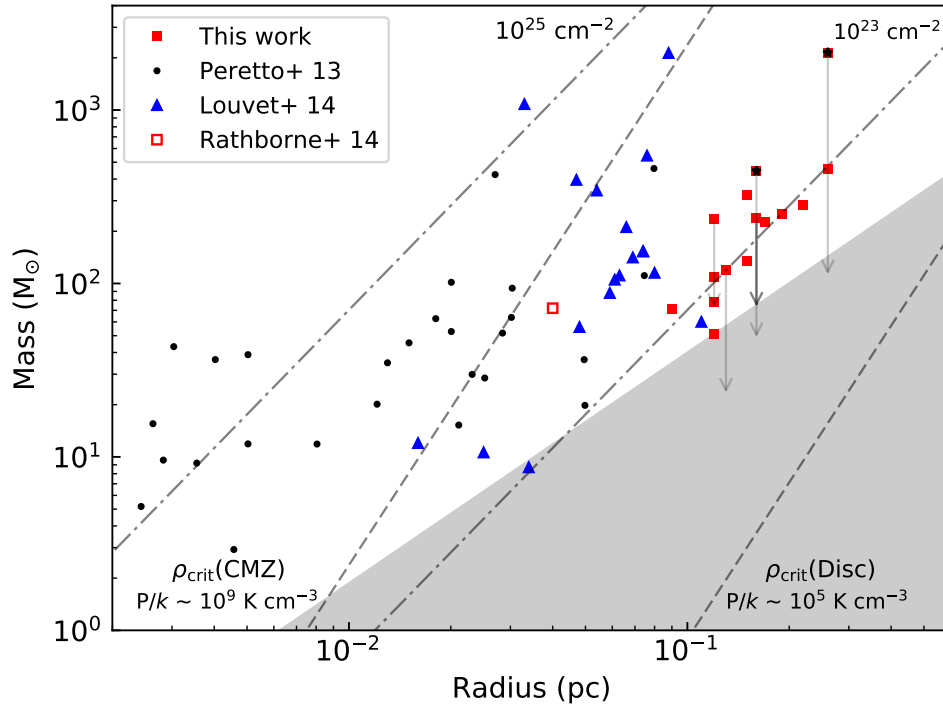


Figure 4.3: Mass-radius plot for all of the SMA cores. Solid red squares correspond to masses estimated assuming a dust temperature of 20 K and arrows indicate the possible range of mass given strong lower limits assuming that the dust temperature is the same as the measured gas temperature. Red points with black star markers indicate that these cores are star-forming. Black points are high-mass proto-stellar cores in the Galactic disc from Peretto et al. (2013) and blue triangles are from Louvet et al. (2014). The open red square is the star-forming core in cloud ‘a’ as seen with ALMA (Rathborne et al., 2014b). Dash/dot lines are constant column density. Dashed lines are predicted critical volume density thresholds for both the CMZ and the Galactic disc. The grey shaded region corresponds to the empirical massive star formation threshold proposed by Kauffmann & Pillai (2010).

they are all likely to form high-mass stars. This is certainly true of the Peretto et al. (2013) and Louvet et al. (2014) samples, but it is currently unclear as to whether this is true for the CMZ cores. As previously discussed, only two of the cores (‘c1’ and ‘e1’) show signs of massive star formation. This difference in the star forming potential of the cores in the disc and the CMZ may be linked to an environmental dependency of the star formation process.

To further investigate the effect of the different environmental conditions, the CMZ cores are considered in the context of pressure confinement. To do this, the analysis of Field et al. (2011) is replicated, where they take the sample of clouds from the Galactic Ring Survey (GRS, Jackson et al. 2006) and study them in the context of

the virial theorem for a self-gravitating isothermal spherical cloud that is subjected to a uniform external pressure, P_e . They note that based upon analysis by Heyer et al. (2009), the clouds are not consistent with simple virial equilibrium. They conclude that this is corrected when accounting for external pressures ranging from $P_e/k \sim 10^4 - 10^6 \text{ K cm}^{-3}$. Note that Heyer et al. (2009) calculated the properties of the GRS sample using rough boxes. Analysis of the GRS clouds by Roman-Duval et al. (2010) uses defined contours. This more defined approach results in the estimated virial ratios being < 1 for most of the clouds, suggesting that they may be gravitationally bound without the need for external pressure.

In Fig. 4.4 the plot given in Figure 3 of Field et al. (2011) is replicated, and both the dust ridge clouds and their embedded cores that have been detected with the SMA are plotted. The relevant parameters for plotting the dust ridge clouds can be found in Table 4.1, and those for the cores in Table 4.3. The GRS data points (Heyer et al., 2009) are shown as black crosses. The dust ridge clouds are shown as solid markers, and the cores are shown as open markers, with their colours corresponding to the clouds in which they are embedded. Note that there are fewer SMA cores displayed in this figure as it requires a measure of the line-width, which was not possible towards all of the dust cores. The dashed black line represents simple virial equilibrium, with no external pressure. The curved lines represent pressure-bounded equilibrium. These lines are described by the following equation, which is a reformulation of the pressure-bounded virial equation –

$$V_0^2 = \frac{\sigma^2}{R} = \frac{1}{3} \left(\pi \Gamma G \Sigma + \frac{4P_e}{\Sigma} \right) \quad (4.2)$$

where V_0 is the size-linewidth scaling coefficient, σ is the velocity dispersion, R is the radius, Γ is related to the density structure, Σ is the mass surface density and P_e is the external pressure. Here we assume $\Gamma = 0.73$, which corresponds to a centrally-concentrated density structure. This is likely valid for the SMA dust cores, but less so for the dust ridge clouds on larger scales, as these clouds display relatively flat

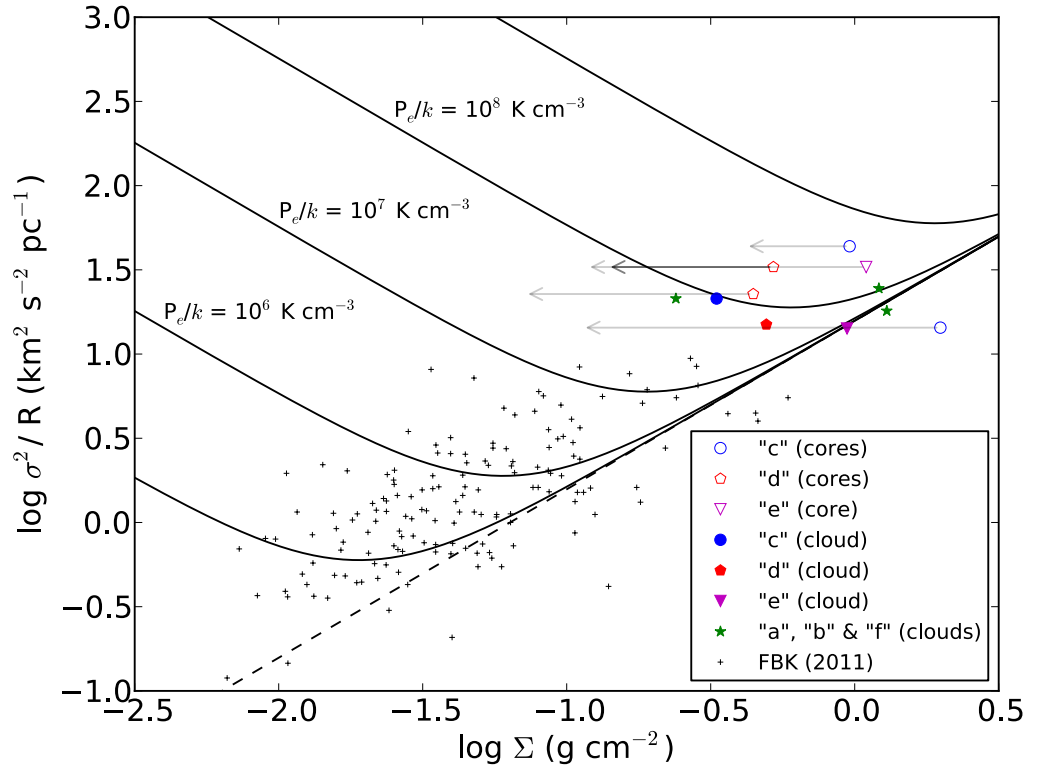


Figure 4.4: Comparison of the dust-ridge clouds and their embedded cores with the GRS cloud sample. Black crosses show the GRS clouds as reported in Field et al. (2011) (original data are from Heyer et al. 2009). Solid markers indicate the different dust ridge clouds, while the open markers represent the core(s) associated with the solid markers (i.e. their parent clouds). Arrows represent the range in surface densities given our upper and lower mass limits. Curved black lines are those of constant external pressure, while the dashed line is for $P_e = 0$.

surface density profiles as a result of their hierarchical internal structure (see previous chapters).

Fig. 4.4 shows that, under the assumption that these cores and clouds are in pressure equilibrium, the external pressures in the CMZ would have to be of order $P_e/k \sim 10^8 \text{ K cm}^{-3}$, which is 2–3 orders of magnitude greater than necessary for the GRS clouds in the Galactic disc. This is consistent with the observed difference in large-scale turbulent pressure between the disc and the CMZ, which for typical conditions in these environments is $P/k \sim 10^5 \text{ K cm}^{-3}$ and $10^{7-9} \text{ K cm}^{-3}$, respectively (Kruijssen & Longmore, 2013; Rathborne et al., 2014b; Longmore et al., 2014a). The turbulent pressure in the CMZ is therefore sufficiently high that the cores may be in equilibrium.

Comparing Figs. 4.3 and 4.4 shows that despite such high external pressures, the embedded cores in the CMZ have comparatively low densities, relative to the high-mass proto-stellar cores in the Galactic disc. Also recall the previous discussion highlighting that these cores generally lack signs of on-going star formation. Out of 15 detected sources, only 2 show signs of ongoing star formation, despite being two orders of magnitude more dense than the volume density threshold proposed by Lada et al. (2010a) and under pressures that are several orders of magnitude greater than in the disc. This leads to the conclusion that this is further evidence for star formation being inhibited in the CMZ as a result of the high turbulent energy density, which drives up the critical volume density threshold for star formation in this environment.

The role of the high turbulent pressure in driving the low star formation rate in the CMZ is illustrated by the critical density lines in Figure 4.3 (dashed lines), which indicate the density thresholds for star formation in the models of Krumholz & McKee (2005) and Padoan & Nordlund (2011) under the pressures seen in the Galactic disc and in the CMZ. These critical density thresholds in the context of these models are estimated as (see Longmore et al. 2014a) –

$$\rho_{\text{crit}} = \frac{4\pi}{3} \frac{\alpha_{\text{vir}} P_{\text{turb}} \mu m_{\text{H}}}{k_{\text{B}} T} \quad (4.3)$$

where α_{vir} is the virial ratio, P_{turb} is the turbulent pressure, μ is the molecular weight, m_{H} is the Hydrogen mass, k_{B} is the Boltzmann constant and T is the gas temperature.

To estimate ρ_{crit} in the CMZ and the disc, it is assumed that $P_{\text{turb}}/k = 10^9$ & 10^5 K cm⁻³ and $T = 75$ & 20 K, respectively. In both cases it is assumed that $\alpha_{\text{vir}} = 1$.

The resultant critical density thresholds differ by several orders of magnitude. While the solar neighbourhood cores are all above their corresponding threshold for star formation, all of the CMZ cores in our sample are currently below the threshold appropriate for CMZ conditions. This suggests that these cores are indeed still coupled to the turbulent flow and have not been able to become self-gravitating (as found in Figure

4.4), thus inhibiting star formation (as concluded by Kruijssen et al. 2014 and Rathborne et al. 2014b). However, the high-mass core in dust ridge cloud G0.253+0.016 (as seen with ALMA, Rathborne et al. 2014b) is the only CMZ core that lies close to the critical density threshold. This may indicate that the comparatively low densities estimated with the SMA data may be partially due to the limited spatial resolution. Also note that, at least in the case of G0.253+0.016, the magnetic field across the cloud has been shown to display little perturbation (i.e. it is highly ordered, Pillai et al., 2015). If the same is true for all of the dust ridge clouds, then it is possible that the magnetic pressure could be of the same order as that due to turbulence and may therefore be important in supporting the clouds against collapse and hence driving up the critical density threshold for star formation. Though, given the expected short lifetimes of clouds in the CMZ of $\sim 1 - 2$ Myr ($1 - 3$ dynamical times; Kruijssen et al., 2015, Barnes et al., submitted), it is not clear the magnetic field would have a significant effect on such short timescales.

4.5 Conclusions from Walker et al. (submitted)

High-resolution observations of the Galactic centre dust ridge clouds ‘b – f’ with the SMA at 1.3 mm are presented. A total of 15 individual dust cores are detected above the 5σ level, many of which are new detections. The masses of these cores are substantial – ranging $\sim 50 - 2150 M_{\odot}$ within radii of $\sim 0.1 - 0.25$ pc, with volume densities $\sim 10^6 \text{ cm}^{-3}$. 13 of these cores do not coincide with known star formation tracers and may represent a sample of potential pre-stellar cores that are possible precursors to high-mass stars. Line emission is detected towards only 3 of these quiescent cores, and virial analysis suggests that they are unbound. However, under the high external pressures in the CMZ, it is possible that they may be in pressure equilibrium.

Two newly-discovered young, high-mass-star-forming cores are reported – ‘c1’ and ‘e1’. These are two excellent candidates for representing the early stages of high-mass star formation in the CMZ, prior to the emission of ionising radiation.

The emission of H_2CO and CH_3CN is used to estimate the temperature of the gas in the cores, which ranges from $\sim 57 - 240$ K. The higher gas temperatures correspond to the cores in which we detect signs of high-mass star formation, indicating internal heating. This gas temperature is used to assume upper limits for the dust temperature and recalculate the core masses. This results in the mass estimates changing by an average of 67%. However, it is cautioned that these masses are very strong lower limits, as the gas is likely to be significantly warmer than the dust at these densities. This highlights the necessity of accurate dust temperature measurements on these small spatial scales in the CMZ.

The dust ridge clouds and the embedded cores are subjected to substantially higher external pressures ($\sim 10^8 \text{ K cm}^{-3}$) – 2–3 orders of magnitude greater than typically found in the Galactic disc. Yet despite their location in such a high-pressure environment, the cores are relatively low density and only two of them show any clear signs of embedded star formation. Comparing the densities of the cores to the predicted critical density thresholds for star formation under the high pressures in the CMZ shows that they fall below this threshold. It is concluded that this is further evidence that the critical density for star formation is indeed higher in the turbulent environment of the CMZ.

4.6 Appendix: Gas Temperature Modelling

Section §4.3.2 highlighted the fact that the dust temperatures on the spatial scales of the SMA observations ($\lesssim 4''$) are not constrained observationally. The best constraints that are available are from Herschel observations (~ 20 K on $33''$ scales). It is known that the gas and dust in the CMZ are not thermalised on these larger scales and that the gas temperatures are significantly higher (see e.g. Ao et al., 2013; Johnston et al., 2014; Ginsburg et al., 2016b; Immer et al., 2016). However, it is possible that the gas and dust may begin to thermalise at high volume densities. Clark et al. (2013) show this in Figure 3 of their paper, in which they model the temperature of the gas and dust as a function of volume density, showing that they begin to couple at densities $>$

10^6 cm^{-3} and seem to converge at $> 10^7 \text{ cm}^{-3}$.

Since the cores that are presented in this chapter are at densities of $\sim 10^5 - 10^6 \text{ cm}^{-3}$, the molecular line emission is used to determine the gas temperature, and it is reasoned that it may begin to couple to the dust temperature at these densities. However, the densities of the cores are below those at which convergence occurs in the model of Clark et al. (2013) and thus there may still be a significant difference between the gas and dust temperatures of up to several factors. Any masses and subsequent calculations are therefore strong lower limits. It is more likely that the actual dust temperature lies somewhere between these limits. In this appendix, the fitting routines that are used to fit line data to estimate gas temperatures and line-widths are described.

4.6.1 Line fitting

To estimate the gas temperature via the H_2CO emission, the lines are fitted under assumed LTE conditions, and best-fit parameters are estimated. Under the assumption of LTE, the routine constructs line profiles with a range of input parameters including peak velocities, temperatures, line-widths, and column densities, following the equations in Mangum & Shirley (2015). The peak velocities of the lines can be selected manually and are fixed according to their known rest frequencies. It then minimises the differences between the constructed lines and the observed line, using the non-linear least-square fitting procedure *lmfit*⁵. The best fit is returned, along with the estimated temperature, line-width, and column density and associated errors, which are taken as the optimised fitting results⁶.

The primary diagnostic here is the ratio of $3_{2,1}-2_{2,0}/3_{0,3}-2_{0,2}$ lines of H_2CO , where a higher fraction indicates a greater population of higher energy states and hence a higher gas temperature. The upper energy levels of the three states of para- H_2CO at $\sim 218 \text{ GHz}$ are 20.9566 K, 68.0945 K and 68.1115 K, respectively (LAMDA database, Schöier et al., 2005). Figure 4.5 shows a plot of gas temperature vs. $3_{2,1}-2_{2,0}/3_{0,3}-$

⁵<http://cars9.uchicago.edu/software/python/lmfit/index.html>

⁶Python code for fitting 218 GHz para- H_2CO lines can be found at <https://github.com/xinglunju/FFTL>.

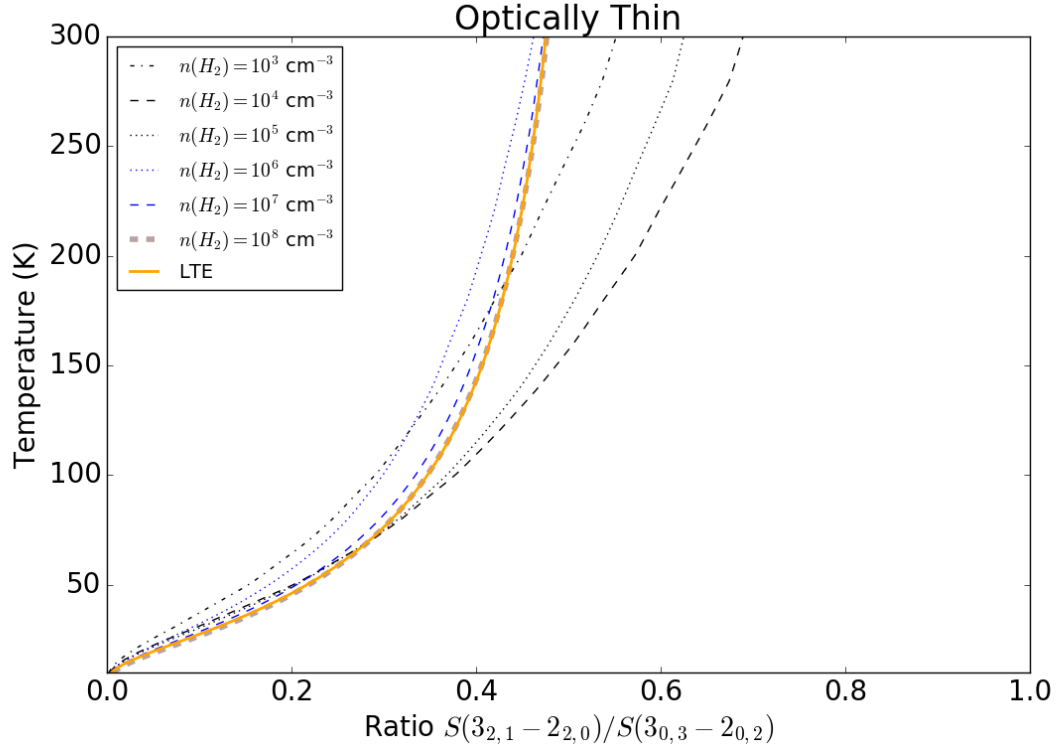


Figure 4.5: Gas temperature estimation as a function of the ratio of $3_{2,1}-2_{2,0}/3_{0,3}-2_{0,2}$ lines of para- H_2CO for different models. The dashed/dotted lines correspond to RADEX models for different volume densities and the solid line corresponds to an LTE model.

$2_{0,2}$. Plotted here (dotted/dashed lines) are several non-LTE models generated using RADEX (van der Tak et al., 2007) for different volume densities. Also plotted (solid line) is an LTE model⁷. This highlights the fact that temperature determination can vary significantly depending on the assumed models and volume densities. Beyond certain line ratios, the models become very sensitive to small changes and are thus uncertain above certain ratios, particularly given the observational uncertainties. This is a caveat of using an LTE approximation as has been done here. Figure 4.5 shows that under LTE, the model becomes asymptotic beyond ratios of ~ 0.4 .

Of the 15 cores that have been detected with the SMA, H_2CO was detected above 3σ in only five of them. In the remainder of the sources, there was only very weak emission

⁷The code used to generate this plot can be found at https://github.com/keflavich/h2co_modeling/blob/master/examples/h2co_j%3D3_lte_vs_radex.py

or complete non-detection. For those with line detection, the core mass is re-calculated, this time using the derived gas temperature as an upper limit to the dust temperature. Using the estimated masses (both lower and upper limits) and line-widths, the virial parameter of each core is estimated ($\alpha = 5R\sigma^2/GM$). All of these quantities are reported in Table 4.3. The line fitting of each of these five cores is discussed in the following sections.

Core ‘c1’

The observations of dust ridge cloud ‘c’ reveal a dust core that is concluded to contain embedded high-mass star formation. This is due to its high brightness in both the continuum and many different molecular lines, as well as its coincidence with $70 \mu\text{m}$ emission and being one of the most rich sites of rare maser emission known in the Galaxy, showing SiO, CH₃OH, H₂CO and H₂O maser emission (Ginsburg et al., 2015). It displays strong emission in the para-H₂CO $3_{0,3}-2_{0,2}$ lines at ~ 218 GHz.

Figure 4.6 (top) shows an integrated intensity map of the para-H₂CO $3_{0,3}-2_{0,2}$ line. Black contours correspond to the SMA 1.3 mm dust continuum. There is good spatial coincidence between the gas and dust towards this core.

Figure 4.6 (bottom) shows the para-H₂CO spectrum averaged over the spatial extent of the core, along with the best-fit and resultant temperature and line-width. While a good fit to the H₂CO emission is obtained for this source, it is not strongly-constraining due to the large line ratio (~ 0.6 , see Fig. 4.5). A lower limit of ~ 150 K is therefore provided, above which this temperature diagnostic is uncertain. This source has strong emission in all three p-H₂CO lines and in its central regions, the ratio of the $3_{2,1}-2_{2,0}/3_{0,3}-2_{0,2}$ lines reaches ~ 0.8 . At these ratios, there are no models that can reliably estimate the gas temperature. However, given that the core is high density ($\gtrsim 10^6 \text{ cm}^{-3}$), the gas temperature must be high.

The J=12–11 k-ladder of CH₃CN is also well detected towards this core, which can also be used to estimate gas temperatures. The $k = 0 - 8$ components of the ladder are detected, the upper energy levels of which are 69, 76, 97, 133, 183, 247, 326, 419

and 526 K, respectively. It therefore traces higher temperatures more reliably than the para-H₂CO transitions. Using a similar LTE fitting routine⁸, the CH₃CN spectrum is fitted (see Figure 4.7) and a spatially-averaged gas temperature of 243.7 K (\pm 18.2 K) is estimated. The fit isn't ideal, primarily due to the heavy blending of the $k = 0$ & 1 components, resulting from the large line-widths. It is also likely that this emission, particularly the higher k -components, is tracing the material closer to the forming star, where the temperatures are higher and can evaporate the molecule off the dust grains and excite them to high energy states. Thus, a beam-averaged spectrum may be averaging over different components that trace different temperatures, densities and line-widths. Despite this, the fit is reasonable and demonstrates that the gas is hot and likely internally heated.

Core 'c2'

This core is situated \sim 0.6 pc away from 'c1' and appears to be connected to it by a filamentary structure in the dust continuum. It is significantly less bright, with an integrated flux almost an order of magnitude smaller (see Table 4.3). It also does not appear to coincide with any star formation tracers and displays very little molecular line emission. It does however have H₂CO emission (Figure 4.8), though the only line that is detected with any significance is the $3_{0,3}$ - $2_{0,2}$ line, indicating that the temperature of the gas is relatively low. Given that this is the only line detected, an upper limit on the gas temperature of 57.6 K is given, as this corresponds to the lower energy level of the $3_{2,2}$ - $2_{2,1}$ line.

Cores 'd2' & 'd6'

The SMA observations of dust ridge cloud 'd' reveal significant dense substructure in the dust continuum, which spans the major axis of the cloud along a filamentary structure containing at least seven cores. None of these cores display any signs of star

⁸Python code for fitting CH₃CN J=12-11 k-ladder can be found at <https://github.com/xinglunju/emanon>

forming activity and have very weak line emission. Only cores ‘d2’ and ‘d6’ coincide with significant H₂CO emission (Figures 4.9 and 4.10).

‘d2’ shows clear emission in all three para-H₂CO transitions at ~ 218 GHz, with a $3_{2,1}-2_{2,0}/3_{0,3}-2_{0,2}$ ratio of ~ 0.3 , which yields a corresponding fit of 86.3 K (± 20.4 K).

‘d6’ has clear emission in the $3_{0,3}-2_{0,2}$ transition, with signs of very weak emission from the other two transitions. Given that these other transitions are around the noise level, a constraining fit is not possible, and so again an upper limit on the gas temperature of 57.6 K is given.

Core ‘e1’

Cloud ‘e’ is the most massive ($1.1 - 1.5 \times 10^5 M_{\odot}$) cloud along the dust ridge and is seen to contain two dense dust cores in the SMA data. One of these, ‘e1’, stands out as it coincides with both H₂O and CH₃OH Class II maser emission, as well as a $70 \mu\text{m}$ source. It is therefore believed to be a potential site of young high-mass star formation. The H₂CO emission traces the dust core well (Figure 4.11). A reliable fit to the H₂CO lines is not possible, as the large line ratio of $3_{2,1}-2_{2,0}/3_{0,3}-2_{0,2}$ cannot be fit by any models. A lower limit of 150 K is assumed, since the LTE method cannot reliably discern between temperatures beyond this. However, given that this core is dense, this large line ratio means that the gas must be hot. There appears to be a slight excess in the emission of the $3_{2,1}-2_{2,0}$ line. The exact cause of this is not known, but it may suggest that there are multiple components present and/or that there are significant temperature/density gradients within the core.

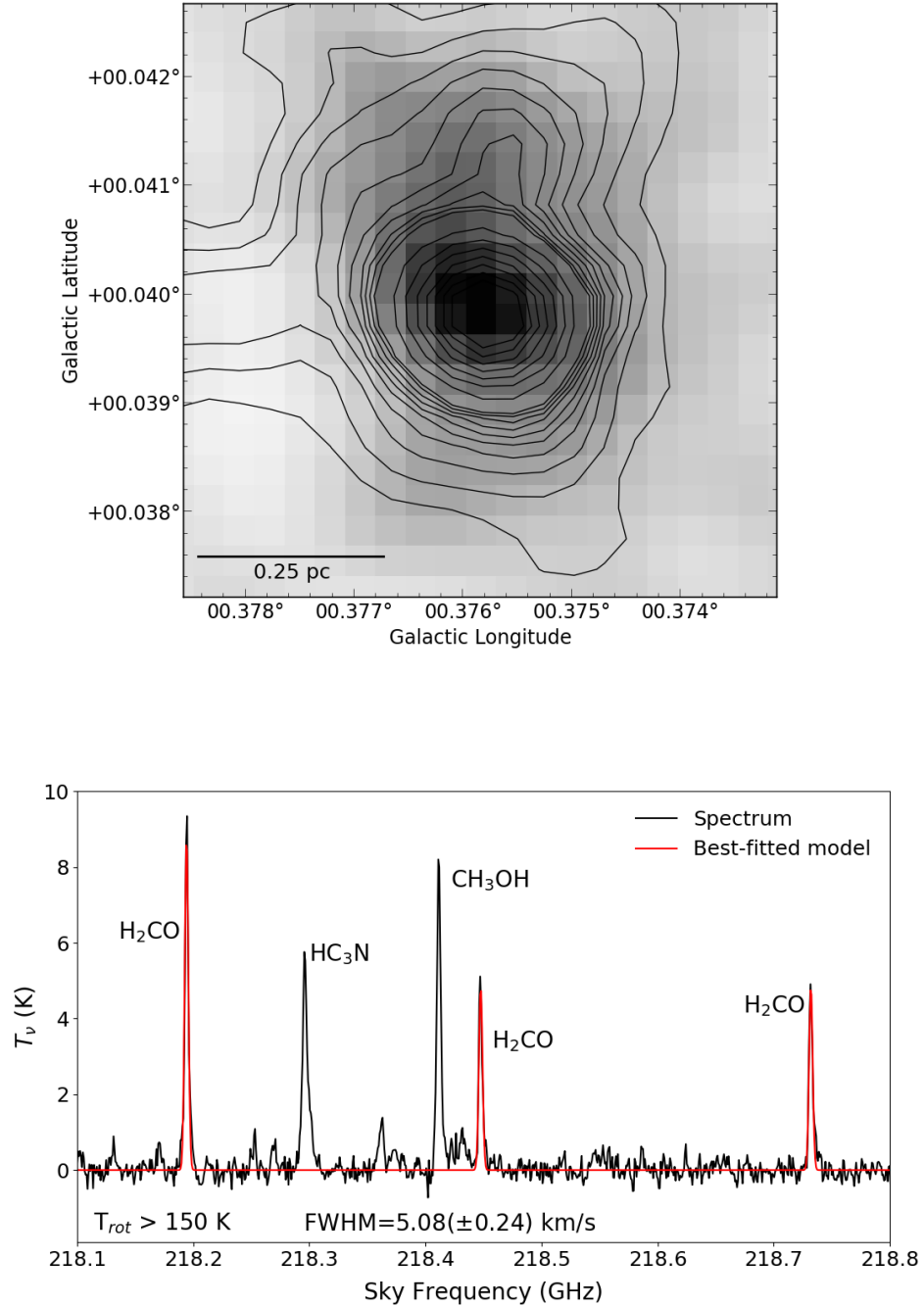


Figure 4.6: *Top*: Integrated intensity map of the para-H₂CO 3_{0,3}-2_{0,2} transition towards ‘c1’. Black contours are SMA dust continuum. *Bottom*: Spatially-averaged spectrum of the para-H₂CO lines (plus HC₃N and CH₃OH). Using an LTE line-fitting routine, the H₂CO lines are fitted. Due to the large line ratios, a constraining gas temperature estimate is not possible (see Fig. 4.5). A lower limit of 150 K is provided, above which our temperature diagnostic is uncertain.

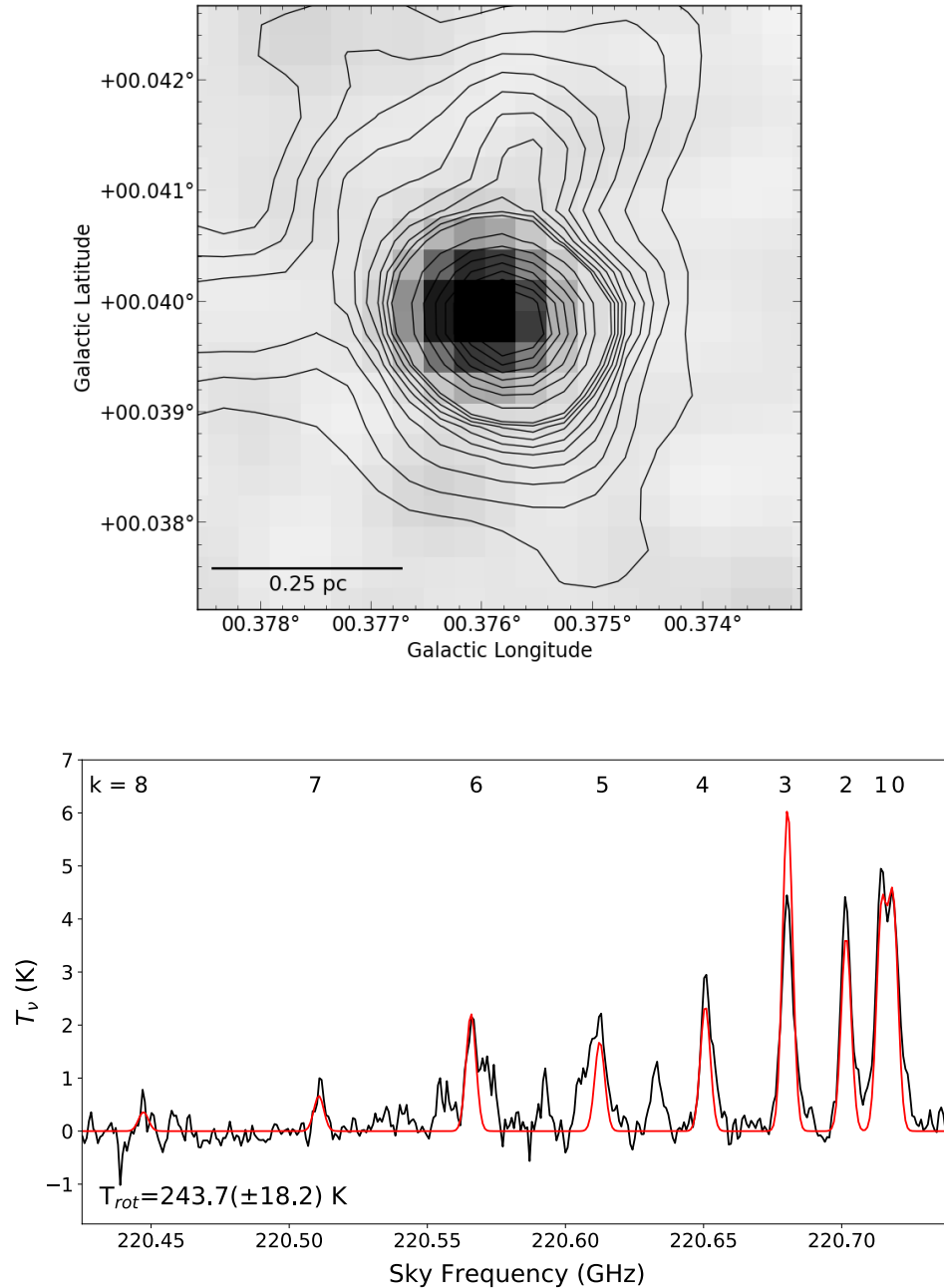


Figure 4.7: *Top*: Integrated intensity map of the CH_3CN $J=12-11$ k-ladder towards ‘c1’. Black contours are SMA dust continuum. *Bottom*: Spatially averaged spectrum of the CH_3CN $J=12-11$ k-ladder. The $k = 0 - 8$ components are clearly detected, the upper energy levels of which are 69, 76, 97, 133, 183, 247, 326, 419 and 526 K, respectively. This suggests significant internal heating, with high gas temperatures likely occurring close to the embedded proto-star(s). Using an LTE line-fitting routine, a beam-averaged gas temperature of 243.7 K (± 18.2 K) is estimated.

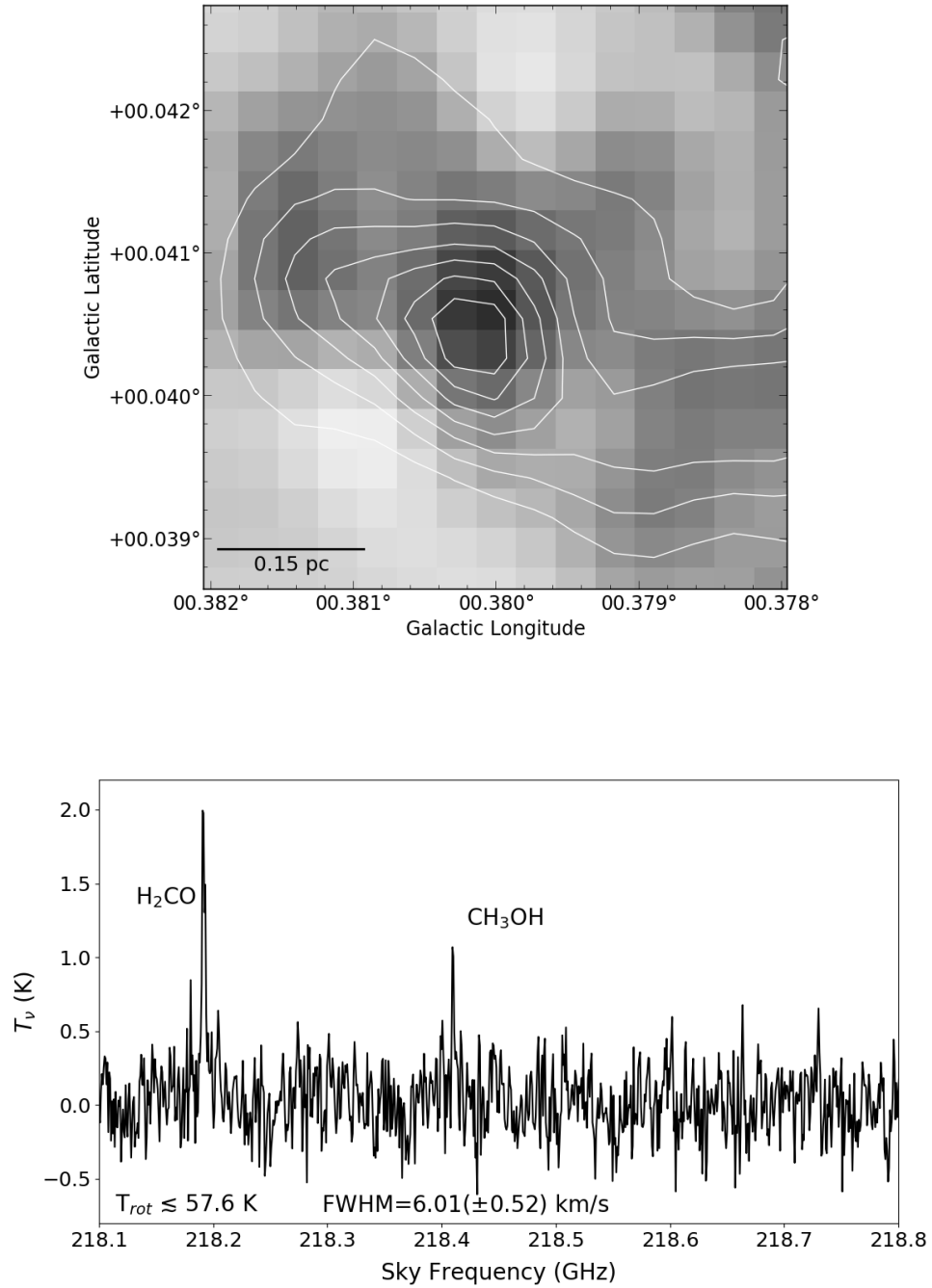


Figure 4.8: *Top*: Integrated intensity map of the para-H₂CO 3_{0,3}-2_{0,2} transition towards ‘c2’. White contours are SMA dust continuum. *Bottom*: Spatially-averaged spectrum of the para-H₂CO lines. Given that only the 3_{0,3}-2_{0,2} line is well detected, an upper limit on the gas temperature of 57.6 K is placed, as this corresponds to the lower energy level of the 3_{2,2}-2_{2,1} line.

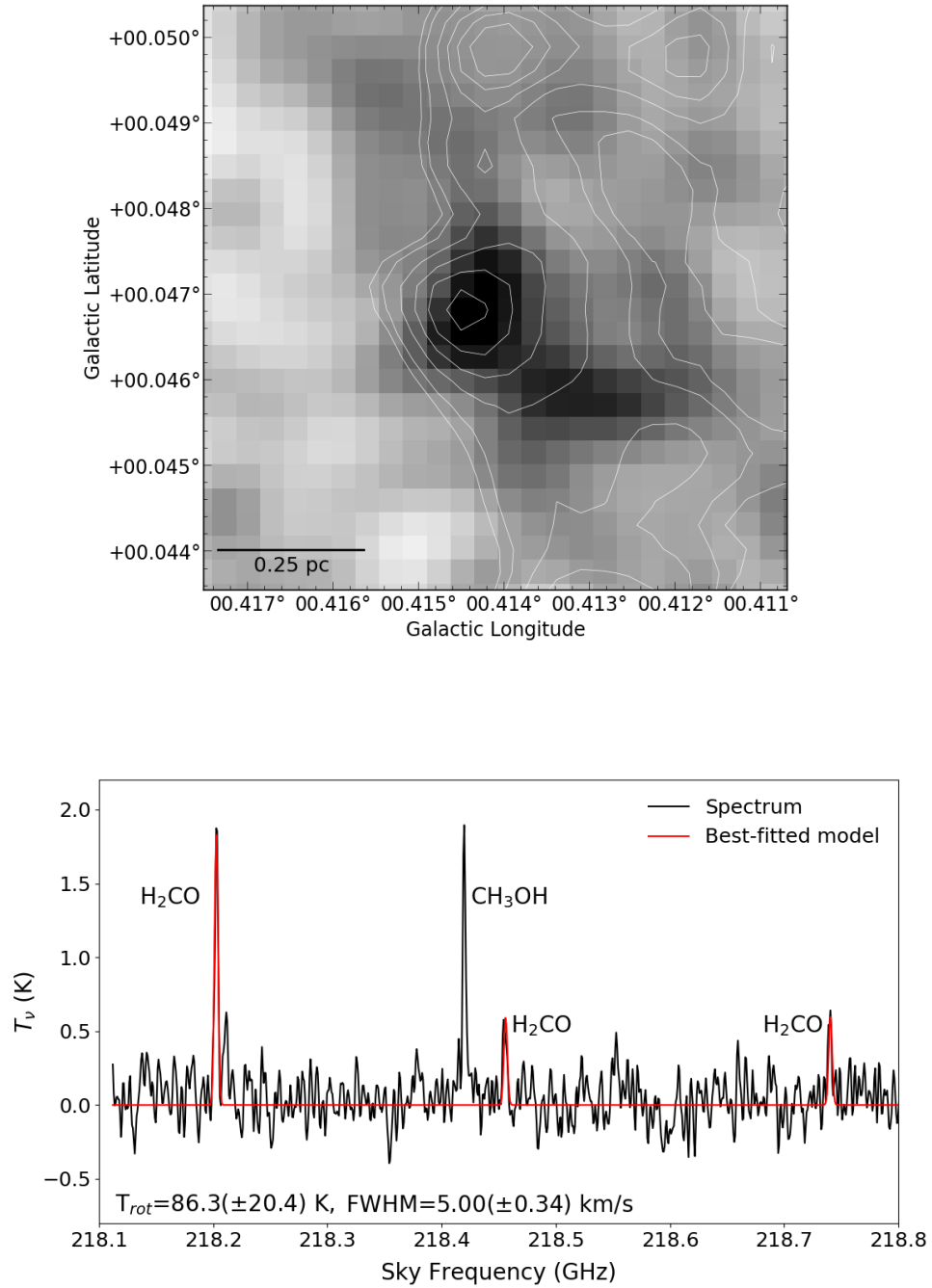


Figure 4.9: *Top*: Integrated intensity map of the para- H_2CO $3_{0,3}-2_{0,2}$ transition towards ‘d2’. White contours are SMA dust continuum. *Bottom*: Spatially-averaged spectrum of the para- H_2CO lines. Using an LTE line-fitting routine, the H_2CO lines are fitted to derive a beam-averaged gas temperature of 86.3 K (± 20.4 K).

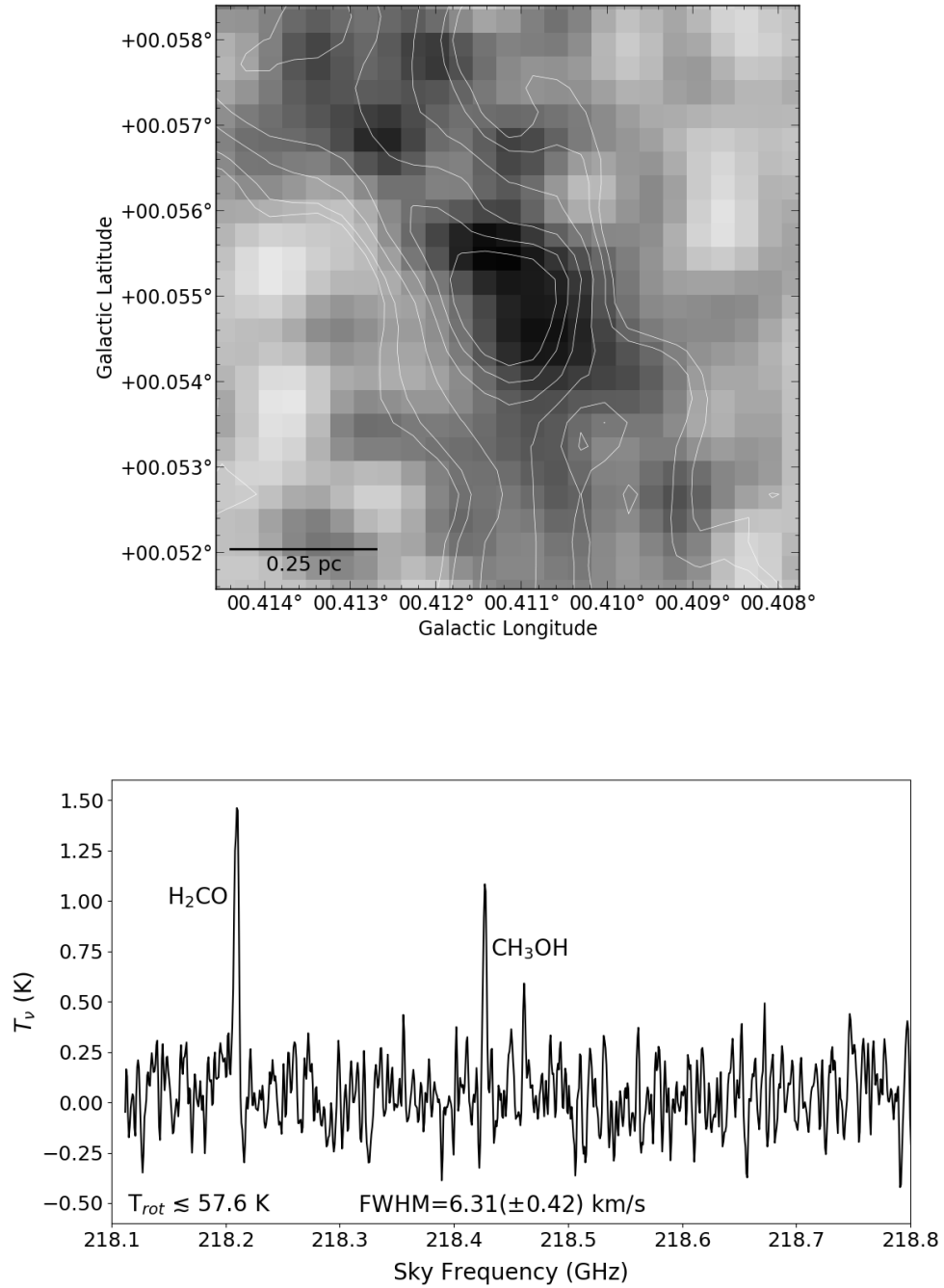


Figure 4.10: *Top*: Integrated intensity map of the para- H_2CO $3_{0,3}-2_{0,2}$ transition towards ‘d6’. White contours are SMA dust continuum. *Bottom*: Spatially-averaged spectrum of the para- H_2CO lines. Given that only the $3_{0,3}-2_{0,2}$ line is well detected, an upper limit is placed on the gas temperature of 57.6 K, as this corresponds to the lower energy level of the $3_{2,2}-2_{2,1}$ line.

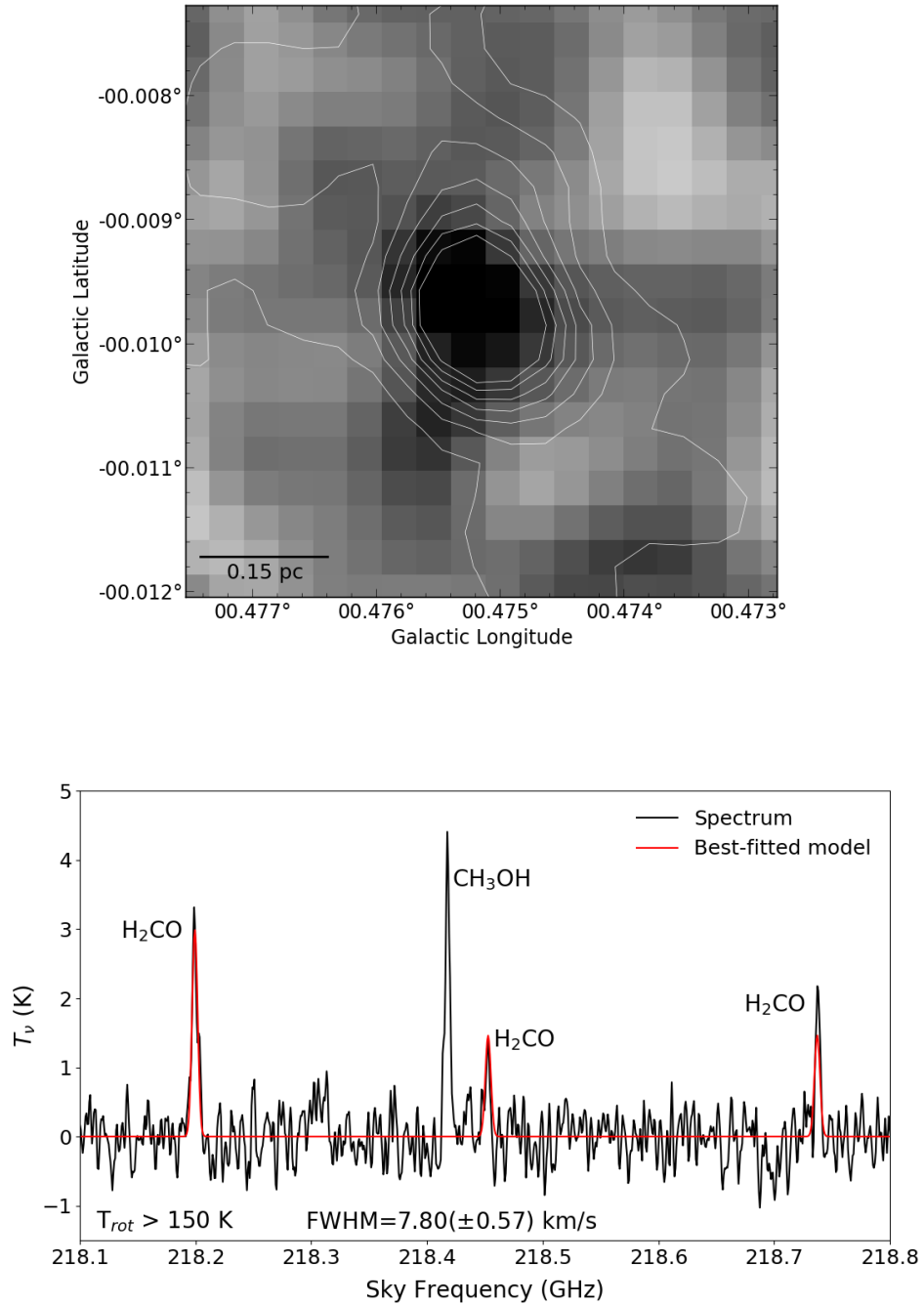


Figure 4.11: *Top*: Integrated intensity map of the para- H_2CO $3_{0,3}-2_{0,2}$ transition towards ‘e1’. White contours are SMA dust continuum. *Bottom*: Spatially-averaged spectrum of the para- H_2CO lines. A reliable fit to the H_2CO lines is not possible, as the large line ratio of $3_{2,1}-2_{2,0}/3_{0,3}-2_{0,2}$ cannot be fit by any models. A lower limit of 150 K is assumed, as the LTE method cannot reliably discern between temperatures beyond this. The cause for the apparent excess in the $3_{2,1}-2_{2,0}$ line is not known, but may suggest that the emission comes from more than one component, and may have a temperature/density gradient.

Chapter 5

On-going and future work

Preface

The previous chapters of this thesis summarise individual self-contained projects that have been completed. The following sections of this chapter provide a summary of projects that are currently on-going and will continue to be worked on beyond the submission of this thesis.

5.1 A time-line for high-mass star assembly with ALMA

As described in Chapter 4, the SMA observations of the dust ridge clouds ‘b’ – ‘f’ as part of the *CMZoom* survey have uncovered a population of high-mass cores. These cores range in mass from $\sim 50 - 2150 M_{\odot}$ within radii of 0.1 – 0.25 pc. Cloud ‘a’ (aka ‘the Brick’; G0.253+0.016) also contains a core of $\sim 260 M_{\odot}$ within 0.1 pc, as revealed by ALMA Cycle 0 observations (Rathborne et al., 2015). In summary, it is now known that the dust ridge harbours a substantial number of compact, high-mass cores. Given this, plus the fact that they are all embedded in dense clumps that provide

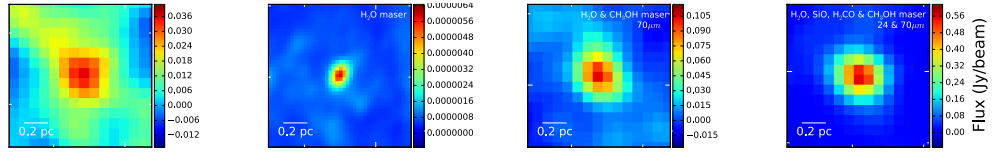


Figure 5.1: The four high-mass cores that are being targeted with ALMA at 230 GHz and $0.13''$ resolution. *From left to right they are:* b1, a1 (Rathborne et al., 2015), e1 and c1. Legends indicate the presence of any star formation indicators.

huge mass reservoirs from which they can accrete, makes these cores prime candidates for the potential formation sites of (very) massive stars.

Additionally, many of the cores display different levels of star-formation activity, based upon the presence of masers and 24 and $70 \mu\text{m}$ emission, all of which are pre-UCH_{II} formation (no centimetre continuum emission detected), as revealed by deep VLA observations (Immer et al., 2012). We therefore have an unprecedented opportunity to study a range of early stages of high-mass star formation prior to the disruption by UCH_{II} regions. As the cores all lie at a similar distance and in a similar environment, any systematic uncertainties affecting their comparison are greatly minimised.

Furthermore, Longmore et al. (2013b) proposed a scenario in which star formation in these dust-ridge clouds may have been triggered by their close passage to the minimum of the Galactic gravitational potential along a common orbital stream (Kruijssen et al., 2015; Henshaw et al., 2016). As the time since triggering is then known, the global properties of these clouds allow us to estimate the number of free-fall times each cloud has undergone since pericentre passage. Remarkably, there is tentative evidence that the cores show increasing mass and signs of star-formation as a function of increasing number of free-fall times since pericentre passage of the parent cloud.

In an effort to exploit the unique opportunity presented by this system of high-mass cores, I am leading an ALMA Cycle 4 project (ID: 2016.1.00949.S) to target a subset of these cores at much higher spatial resolution. I selected the most massive and dense core in clouds ‘a’, ‘c’, ‘d’ and ‘e’ to target at higher angular resolution ($0.13''$), and at the same frequency (230 GHz) with an almost identical spectral setup to the SMA observations. The reason for this is that by targeting the same lines at higher spatial resolution, a multi-scale view of the cores and their dynamical interaction with

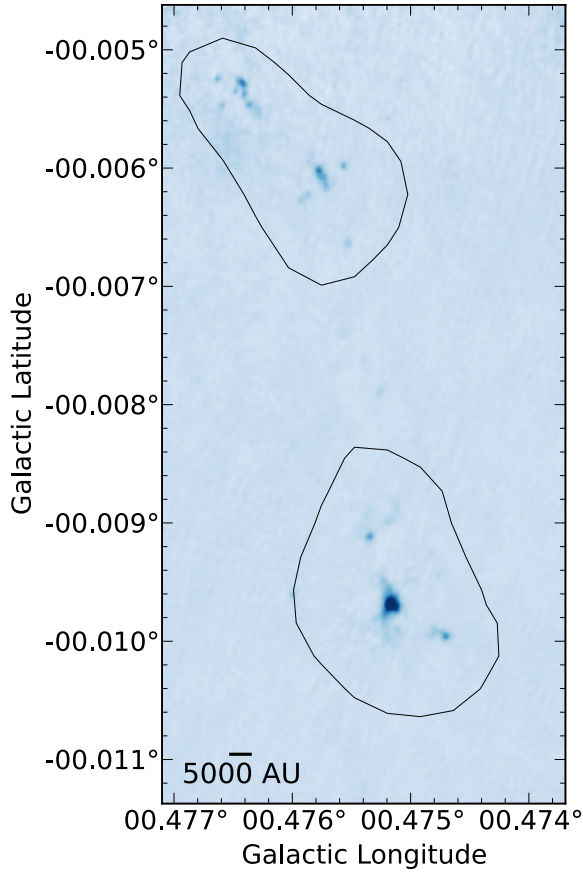


Figure 5.2: ALMA 230 GHz continuum image of cores ‘e1’ and ‘e2’ in dust ridge cloud ‘e’ (G0.489-0.010). Black contours show the SMA 230 GHz continuum emission. There is clear correspondence between the SMA and ALMA dust peaks, and the ALMA observations reveal a high degree of fragmentation. The centre of ‘e1’ is dominated by one bright core, consistent with the fact that there is on-going high-mass star formation there.

the larger reservoir of gas in the cloud can be obtained. These particular cores were chosen as they display a range of star forming indicators, from totally quiescent (core ‘d6’), to a bonafide young high-mass proto-star (core ‘c1’). Using these observations, I will analyse the gas and dust on ~ 1000 AU (5×10^{-3} pc) scales to reveal the internal structure of these cores and address key open questions regarding high-mass star formation (Tan et al. 2014) such as – what are the fragmentation properties in these extremely high-mass cores, and how do they compare to theoretical predictions that are motivated by different physical processes? Do such cores contain a clustered population of low-mass sources and if so, how do these compare to low-mass proto-stars in the disc of the Galaxy? Or are the cores instead dominated by a single proto-star? Are such extreme proto-stars fed via disc accretion as seen for low-mass stars? These data will provide the first look into the earliest stages of the formation of the high-mass stars in the CMZ and allow me to isolate the dominant physical mechanisms governing their formation.

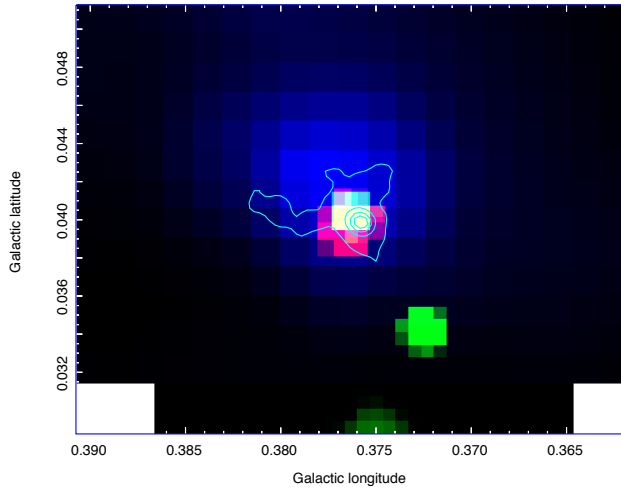


Figure 5.3: Three-colour image of dust ridge cloud c. Blue: dust column density from HiGAL. Red: 70 μm emission from Herschel. Green: 24 μm emission from MIPS GAL. Blue contours show the SMA 230 GHz dust continuum emission.

The observations for this project are still currently underway. So far, one science target has been fully observed – core ‘e1’ in dust ridge cloud ‘e’ (see Table 4.3 in the previous chapter for properties). Figure 5.2 shows an ALMA pipeline calibrated image of the 230 GHz dust continuum, overlaid with SMA 230 GHz continuum contours. The ALMA data reveal a significant degree of fragmentation on smaller spatial scales. Work is currently underway to estimate the masses and sizes of these cores, as well as to identify which molecular lines are detected, and how they can inform our understanding of the chemistry, kinematics and temperature structure of the cores.

5.2 An ALMA view of a high-mass proto-star in the CMZ cloud G0.38+0.04

Of the cores that have been detected with the SMA observations, one stands out in particular. Core ‘c1’ in dust ridge cloud ‘c’ is situated towards the south of the cloud and may contain up to 2150 M_{\odot} in a radius of 0.25 pc. It is also known that strong 70 μm and 24 μm emission is coincident with the position of the core (see Figure 5.3). From Herschel data, it is estimated that the luminosity of this source is $\sim 6.5 \times 10^4 L_{\odot}$. This high luminosity, plus the fact that there have been no H_{II} regions detected towards this region in the centimetre continuum (Immer et al., 2012), means that this source must be very young.

The source also displays a rich amount of maser emission. Figure 5.4 shows the position of all the known masers with respect to the dust core, along with their respective velocities (Ginsburg et al., 2015). It appears to be the richest source of rare maser emission in the Galaxy, coinciding with H₂O, CH₃OH, H₂CO and SiO maser emission. Only eight H₂CO masers have been identified in the Galaxy so far, all of which are seen to be associated with high-mass star formation (see Ginsburg et al. 2015 and references therein). Even more rare are SiO masers. These are commonly detected towards evolved stars, but only rarely towards star-forming regions, and then only in regions of known high-mass star formation. Thus far, only five SiO masers have been identified towards such regions in the Galaxy.

Orion KL, Sagittarius B2 N, Sagittarius B2 MD5, W51N, and G0.38+0.04 (aka dust-ridge cloud ‘c’) are the only known SiO maser sources associated with star formation (Zapata et al., 2009b; Ginsburg et al., 2015). Each of these is in some way unique, and so far no clear connection between them has been identified. SiO masers involve rotational transitions inside excited vibration states, which lie well above the ground state (e.g. Elitzur et al., 1983). In Orion KL, the modelling of their excitation is found to be consistent with radiative pumping (Goddi et al., 2009).

One of the critical difficulties in understanding the origin of the SiO maser emission has been confusion. In Orion, extensive VLBI observations show that the SiO masers trace part of a rotating disk (Goddi et al., 2009; Greenhill et al., 2013). In Sagittarius B2 and W51, however, it has only been observed that the masers are associated with massive hot cores – in these regions, these hot cores are adjacent to extreme H_{II} regions that make resolving individual sources difficult (De Pree et al., 2011). Due to its unique position in the CMZ, its relatively isolated location, its wealth of masers and its lack of H_{II} regions (Immer et al., 2012), core ‘c1’ is the ideal source to permit studies of the origin and nature of rare maser emission towards high-mass star forming regions.

Given this, I am observing this source with ALMA in Cycle 4 (ID: 2016.1.00766.S) at very high spatial (0.078", 3.1×10^{-3} pc or 650 AU) and spectral resolution (0.4 km s⁻¹), at ~ 86 GHz (band 3). The primary motivation behind this observation is to simultaneously study these peculiar SiO masers and the high-mass proto-stars that drive them

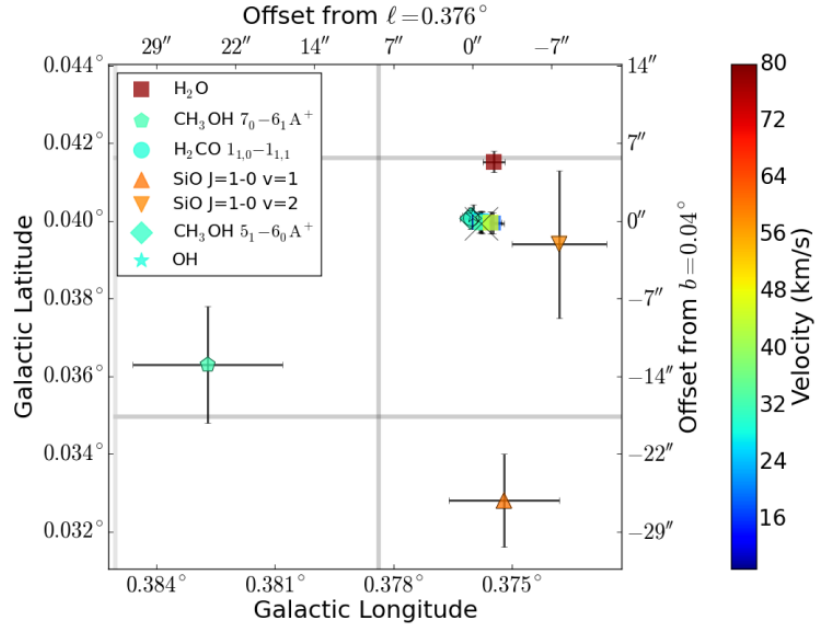


Figure 5.4: Overview of the masers detected towards G0.38+0.04, coloured by velocity (Ginsburg et al., 2015). The positional errors on the SiO and CH₃OH 7₀ – 6₁ A⁺ measurements are much larger than for the other data sets because the measurements are low signal-to-noise from single-dish observations. The grey boxes show the pixel size from the Mopra observations of these lines. The large X marks the centroid location of dust core detected in the 1.3 mm continuum with the SMA.

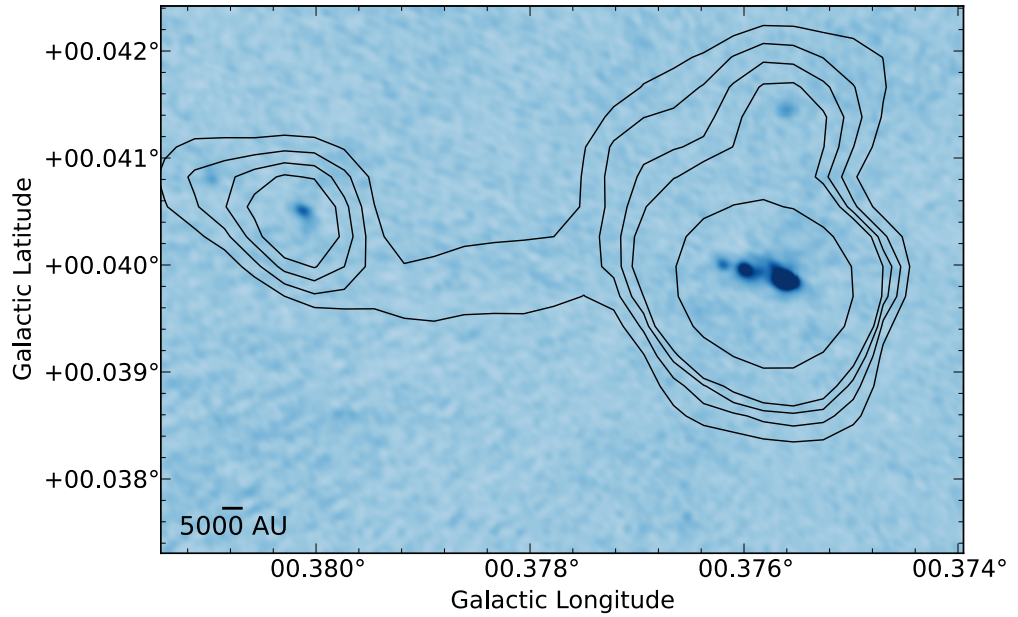


Figure 5.5: ALMA 86 GHz continuum image of cores ‘c1’ and ‘c2’ in dust ridge cloud ‘c’ (G0.38+0.04). Black contours show the SMA 230 GHz continuum emission. There is clear correspondence between the SMA and ALMA dust peaks, and the central bright source fragments into at least 3 individual cores.

down to very small spatial scales. The observations are partially complete. The source has currently been observed at an angular resolution of $\sim 0.36''$, and I am currently waiting for the remaining observations to be taken when the array is in a more extended configuration. Figure 5.5 shows an ALMA pipeline calibrated image of the 86 GHz dust continuum, overlaid with SMA 230 GHz continuum contours. There is clear agreement between the dust emission from the SMA and ALMA. The central bright source is seen to fragment into at least 3 separate cores, that are very close to one another (few thousand AU) and ordered in an intriguingly linear fashion. Whilst waiting for the final observation to be taken, preliminary analysis will begin to search for the molecular lines detected towards this source, with a particular focus on searching for the detection of vibrationally excited SiO emission towards the bright central core.

5.3 Searching for proto-cluster candidates with HOPS and ATLASGAL

In the introduction to this thesis (§1) it was noted that no starless YMC precursors have been identified in the Galactic disc. This is in contrast to the CMZ, where the dust ridge clouds that have been studied in this thesis appear to be largely starless, despite being as massive and dense as similar star-forming clouds in the disc. Even so, it is found that even these are not dense enough to form a typical YMC at their current density distributions (see Chapters 2 and 3). Thus, despite dedicated observational searches, no clouds have been found with a sufficient mass to form a YMC in-situ at their typical stellar density distributions. The fact that more quiescent, less evolved clouds contain less mass in their central regions than highly star-forming clouds, suggests an evolutionary trend in which YMC progenitor clouds continue to accumulate mass towards their centres after the onset of star formation (see conclusion of Chapter 3).

There are several natural consequences of this ‘conveyor-belt’ scenario for YMC formation. Firstly, at the earliest evolutionary stages, the mass in the precursor clouds that

ultimately ends up in the YMC is spread over a much larger radius. As such, potential YMCs precursor clouds at the earliest evolutionary stages may have been excluded from previous searches. Secondly, the gas at these larger radii must converge to the eventual cluster centre in less than ~ 1 Myr – the upper limit to the observed stellar age spreads in YMCs (see e.g. Longmore et al., 2014a). Such converging gas flows should be imprinted in the observed gas kinematics.

This section outlines a method to search for YMC precursor candidates in the Galactic disc using the H₂O Southern Galactic Plane Survey (HOPS, Walsh et al., 2011) and APEX Telescope Large Area Survey of the Galaxy (ATLASGAL, Schuller et al., 2009).

To search for potential YMC precursors in the HOPS catalogue, the sources are first correlated with any corresponding dust continuum emission. In doing this, one can estimate the masses and global kinematics of the sources and examine the morphologies of both the dust and gas emission to identify sources of potential interest. To do this, data from ATLASGAL were utilised. ATLASGAL provides a map of > 400 square degrees of the inner Galaxy at $870 \mu\text{m}$, with an angular resolution of $\sim 19''$.

To match the sources in the HOPS catalogue with regions in the ATLASGAL map, the full ATLASGAL map is smoothed to match the angular resolution of the HOPS data. The 2D HOPS masks are then applied to the ATLASGAL map to extract the data within each mask as an individual map. As the coverage of the two surveys are different, it was not possible to obtain a masked dust map for every HOPS source. Of the 687 sources in the HOPS catalogue, 605 corresponding dust maps were obtained.

Having correlated the gas and dust emission for the HOPS sources, their masses and radii are then estimated. The mass of each source is calculated via the same method outlined in Chapter 2 of this thesis. As the dust temperature is unknown for all of the sources, a uniform value of 15 K is assumed in all cases. Though the true dust temperature is likely to be non-uniform and vary between the regions, 15 K is consistent with typical temperatures seen in molecular clouds (see e.g. Wielen et al., 2012). The distance to each source is taken from those estimated by Urquhart et al. (2014). These

distance estimates are then coupled with the estimated geometric radii of the HOPS masks for each catalogued source to determine their physical radii in parsecs.

The mass and radius estimates for all of the HOPS sources are used to identify which of these may be potential sources of interest in the context of YMC precursors. As YMCs are typically $> 10^4 M_{\odot}$, the search is limited to any sources that contain at least this much mass, such that when accounting for a star formation efficiency and the systematic uncertainties (factor of ~ 2), such a cloud could potentially form a $10^4 M_{\odot}$ cluster. Only clouds with radii of no more than a few tens of parsecs are considered, as clouds larger than this are unlikely to dynamically evolve (collapse) on short enough time-scales that they could form a dense, massive cluster.

Fig. 5.6 displays the mass vs. radius for all of the 605 ATLASGAL regions that were extracted using the HOPS masks. The dotted horizontal line indicates the $10^4 M_{\odot}$ threshold. A total of 12 sources (marked as red points) are found to be above this mass threshold. Many of the sources are found to be projected within a few degrees of the Galactic centre. Inspection of the dust continuum emission and the NH_3 (1,1) integrated intensity, velocity field and the velocity dispersion towards G001.374+0.112, G002.826+0.048, G003.145+0.3014, G003.340+0.396 and G358.894-0.290, show that these sources all have very broad line profiles, with FWHM in excess of 15 km s^{-1} . Inspection of the full HOPS NH_3 data cubes show these sources are clearly associated with prominent features in the Galactic centre such as the 1.3 degree cloud and Sagittarius C. The kinematic models used to determine distances from the V_{LSR} are not reliable for regions so close to the Galactic centre. Placing these sources at the correct distance of $\sim 8.4 \text{ kpc}$ (Reid et al., 2009a, 2014) and using a lower limit to the dust temperature of 20 K, the mass of these sources drops below $10^4 M_{\odot}$. It is therefore concluded that these are unlikely to be YMC precursor clouds. This leaves a total of 7 candidate sources. Table 5.1 summarises the properties of these sources.

To determine whether these sources are potential precursors to YMCs, both the dust continuum and gas kinematics are inspected. This serves to identify sources that possess the qualities one would expect of a YMC precursor that may be forming via a ‘conveyor belt’ mechanism, i.e. centrally-concentrated with kinematic properties that

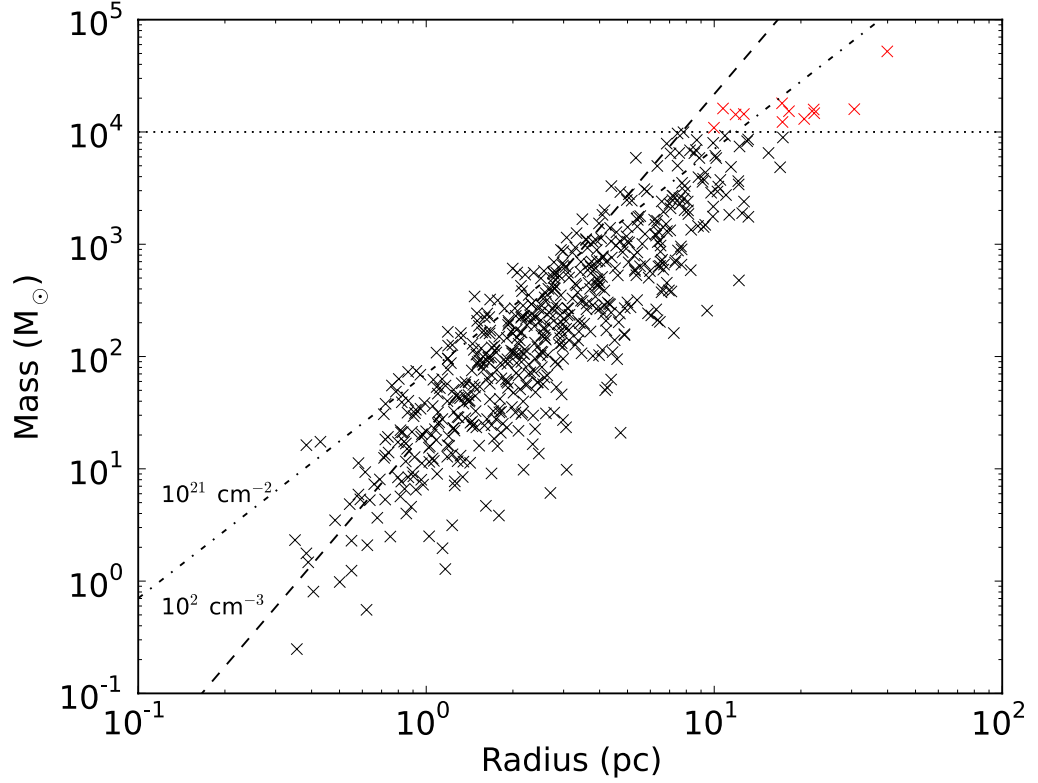


Figure 5.6: Mass-radius plot for all of the 605 HOPS sources. The horizontal dotted line denotes the threshold of $10^4 M_{\odot}$ for selecting potential pre-YMC candidates. The dashed line corresponds to a constant volume density of 100 cm^{-3} (assuming spherical geometry), and the dash-dot line corresponds to a constant column density of 10^{22} cm^{-2} . Sources of interest are marked red.

Source	M $10^4 M_{\odot}$	R pc	FWHM km s^{-1}	d_{near} kpc	d_{far} kpc	$d_{\text{adopted}} (\Delta d)$ kpc	Prob.
G003.432-0.351	1.2	17	3.08	*	*	21.1 (3.7)	0.59
G316.752+0.004	1.5	18	2.95	2.6	9.8	9.8 (0.8)	0.54
G330.881-0.371	1.1	9	3.5	3.9	11.0	11.0 (0.4)	0.7
G338.464+0.034	1.6	10	11.8	3.1	12.7	12.6 (0.5)	0.74
G341.224-0.274	1.3	20	1.89	3.6	12.5	12.4 (0.5)	0.79
G350.170+0.070	1.8	17	5.66	5.8	11.0	10.4 (0.4)	0.72
G357.555-0.323	1.5	22	1.48	*	*	16.8 (2.3)	0.79

Table 5.1: Properties of the HOPS sources that have been identified as candidate precursors to YMCs. Given are the estimated mass (M), radius (R), FWHM, near distance (d_{near}), far distance (d_{far}), adopted distance (d_{adopted}) with associated error (Δd), and the probability the the source is at the adopted distance. *This indicates that near and far distance limits for these sources are not constrained.

may be suggestive of infall/global contraction. To do this, the dust continuum and the integrated intensity, the velocity field and the velocity dispersion of the NH_3 (1,1) emission are all inspected. Additionally, data archives and catalogues are searched to look for associated Herschel $70 \mu\text{m}$ emission, Spitzer/GLIMPSE $8 \mu\text{m}$ emission or absorption and CH_3OH and H_2O maser emission (Walsh et al., 2011; Caswell et al., 2010b, 2011).

The following discusses the characteristics of each of the 7 candidate sources. Please refer to Appendix B for the corresponding images of each source.

G003.432-0.351

This source is centrally-condensed, has a velocity gradient across it of up to 8 km s^{-1} and has a high velocity dispersion that peaks towards its centre. Coupled with its high mass estimate, this seems promising as a candidate YMC precursor. However, it stands out as an absorption feature at $8 \mu\text{m}$, and only has a 59% probability of being at the adopted distance of 21.1 kpc. Given these factors, it is likely that the source is actually at the near distance of 3.08 kpc. This would result in a mass estimate that is ~ 47 times smaller, and thus would not qualify the source as a YMC precursor. It is also found to coincide with a $70 \mu\text{m}$ source and a CH_3OH maser (Caswell et al., 2010b) and is therefore not quiescent.

G316.752+0.004

From the distance likelihood estimation (see Table 5.1), it is only marginally more probable that the source lies at the far distance of 9.8 kpc, rather than the near distance of 2.6 kpc. The mid-IR images also show absorption features with a similar morphology as the dust and NH_3 emission, which would suggest this source is at the near distance. Indeed, previous studies have concluded this source is at the near distance (see e.g. Longmore et al., 2007, and references therein). In which case, the mass in Table 5.1 is overestimated by a factor 13. Thus, it is concluded that this source is

unlikely to be a YMC progenitor cloud.

G330.881-0.371

This region shows two clearly distinct velocity components, with two clumps that are separated by $> 20 \text{ km s}^{-1}$ (see Figure B.5). Masking out the unrelated clump (lower left in Figure B.5) reduces the mass estimate by 11%, down to $\sim 9800 M_{\odot}$. It stands out in absorption against the $8 \mu\text{m}$ and may therefore be at the near distance of 3.9 kpc, which would further reduce the mass estimate to $\sim 1230 M_{\odot}$. It contains a $70 \mu\text{m}$ source and CH_3OH and H_2O maser emission (Caswell et al., 2011; Walsh et al., 2011), showing that star formation is underway, although at an early evolutionary stage. Whether or not this source is YMC progenitor candidate depends primarily on correctly resolving the distance ambiguity. But even if it does lie at the far distance, more detailed calculations of the mass (e.g. including the actual distribution of dust temperature) are required to see if the mass reservoir is large enough for the cloud to produce a YMC.

G338.464+0.034

The dust continuum and NH_3 maps show two distinct peaks of roughly equal intensity, offset by $\sim 5\text{--}10 \text{ pc}$. The $8 \mu\text{m}$ emission shows significant nebulosity, although it is not clear if this is physically associated with the dense gas. The northern gas component has an embedded $70 \mu\text{m}$ source and CH_3OH and H_2O maser emission (Caswell et al., 2011; Walsh et al., 2011), indicating that star formation is underway. The probability that this source lies at the far distance is high (74%), and there is no evidence of $8 \mu\text{m}$ absorption features with similar morphology to the NH_3 and dust emission. At the peak of the NH_3 integrated intensity and dust emission the two gas clumps are offset in velocity by $\sim 6 \text{ km s}^{-1}$. Although there are clear signs of a velocity gradient along the major axis of the two clumps, suggesting that they may be physically associated, the angular resolution of the HOPS data is too coarse to see whether this velocity gradient is unambiguously contiguous from one clump to the other. As such, it cannot be ruled

out that these may be physically unassociated dense clumps. However, if they are physically associated, it is intriguing that the velocity gradient is sufficient to bring the two clumps together in 1 Myr – the maximum age spread observed for YMCs. This is an interesting candidate to follow up as a potential YMC progenitor candidate.

G341.224-0.274

Both the dust and NH₃ emission for show multiple components spread over a projected radius of > 20 pc. The probability that this source is at the far distance is high (79%). Both CH₃OH and H₂O maser emission is found (Caswell et al., 2011; Walsh et al., 2011), along with several 70 μm sources and 8 μm emission that appears to be showing signs of stellar feedback (Figure B.10), indicating intense star formation activity. The NH₃ (1,1) data cubes show that there is almost no change in velocity across the main ridge of the source which contains most of the mass. Unless there are convergent gas motions of > 10 km s⁻¹ purely in the plane of the sky, there is no way that the gas in this source can condense to a radius of ~ 0.1 pc within 1 Myr. It is therefore concluded this is unlikely to be a YMC progenitor, and certainly not a quiescent one.

G350.170+0.070

This region is characterised by at least 3 separate clumps, and it is not clear how/if they are associated. There is an abundance of CH₃OH masers and one H₂O maser (Caswell et al., 2010b; Walsh et al., 2011), and 70 μm sources and 8 μm emission (see Figures B.12 and B.13). It is therefore concluded to not be a quiescent YMC precursor. Further analysis is required to assess the cluster forming potential of the bright, star-forming clump at ~ G350.1+0.100.

G357.555-0.323

This region displays the characteristics of a long, infrared-dark filamentary structure (see Figure B.14). It stands out in absorption at 8 μm and contains one 70 μm source

that is coincident with both CH₃OH and H₂O maser emission is found (Caswell et al., 2011; Walsh et al., 2011). The NH₃(1,1) integrated intensity and velocity dispersion don't appear to peak where the dust continuum peaks, and there is no obvious sign of a coherent velocity gradient across the region. Again, unless there are convergent gas motions of $> 10 \text{ km s}^{-1}$ in the plane of the sky, this region cannot condense to a radius of $\sim 0.1 \text{ pc}$ within 1 Myr. It is therefore concluded this is unlikely to be a YMC progenitor.

Summary of HOPS sources

In summary, the search to find YMC progenitor candidate clouds using the HOPS data has thus far proved inconclusive. The main limiting factor in determining whether or not most of the sources are genuine YMC progenitor candidates is the uncertainty in the distance, and hence mass. Although several sources may lie at the far kinematic distance, and therefore have sufficient mass to form a YMC, more detailed investigation is required to prove this conclusively. The most promising candidates are G330.881-0.371, G338.464+0.034 and G350.170+0.070. If these do lie at the far kinematic distance, and all the gas is physically associated, the NH₃ (1,1) velocity structure suggests the magnitude of the gas motion is sufficient to bring the mass to a radius of $< 1 \text{ pc}$ in under 1 Myr. However, the major caveat for this to occur is that these gas flows must be convergent. Further analysis of these clouds is therefore required.

Regardless of whether these turn out to be YMC progenitor clouds or not, one thing is clear – all the candidates that have been identified are already forming stars. Despite relaxing the search criteria to find younger sources, and despite HOPS having sufficient sensitivity and resolution to find quiescent progenitor clouds, none were found. This leads to the conclusion that starless YMC progenitor gas clouds either do not exist in the disc of the Galaxy, or that the quiescent phase is so short it is effectively not observable given the small number of YMCs expected to be forming at any time in the Milky Way. If any of these sources are YMC precursors that are forming via a ‘conveyor belt’ mode (see Chapters 2 and 3), then this could suggest that there is no

truly starless phase, and that the cluster forms along with concurrent contraction of the system.

Chapter 6

Conclusions

The aim of the work conducted in this thesis was to take a detailed look at the most extreme quiescent molecular clouds in the Galaxy – the Galactic centre dust ridge – in the context of high-mass star and cluster formation, and how their location in the extreme environment of the CMZ may be used to help uncover the extent to which the process of star formation is sensitive to the conditions of its natal environment. The following provides a summary of the results of the work carried out in pursuit of these goals.

6.1 Summary

The conclusions drawn from this research can be summarised as follows –

- (i) Using the multi-wavelength continuum observations of the Herschel infrared Galactic Plane Survey (HiGAL, Molinari et al., 2010) in combination with the spectral line data from the Millimetre Astronomy Legacy Team 90 GHz Survey (MALT90, Foster et al., 2011, 2013; Jackson et al., 2013), the Galactic centre dust ridge clouds are determined to be high-mass ($10^{4-5} M_{\odot}$), compact (1–3 pc) and gravitationally bound. Given their lack of widespread embedded star for-

mation, it is concluded that these are ideal candidates for representing the initial conditions of YMC formation in the CMZ.

- (ii) Comparing the distribution of the gas in the dust ridge clouds (YMC precursors) to that of the stars in Sagittarius B2 (proto-YMC) and the Arches cluster (YMC) reveals a stark contrast in the way the gas and stars are distributed. The stellar content is characterised by central concentration, followed by a sharp density fall off beyond the ‘core radius’. In contrast, the clouds have comparatively shallow mass distributions, with no significant central concentration. ALMA observations instead show that the gas and dust is highly structured throughout. This is concluded to be at odds with theories in which YMCs are predicted to form from very dense initial conditions, followed by expansion due to the expulsion of residual gas.
- (iii) The previous result was found to be true in the CMZ. As this is an extreme region compared to the Galactic disc, a follow up study was conducted to extend this comparison between YMCs and their precursors throughout the Galaxy. This showed that, in all but the case of Westerlund 1, YMC precursor clouds are not sufficiently dense or centrally concentrated that they could form a typical cluster that then expands due to gas expulsion. The observations also reveal a possible evolutionary trend, in which clouds contract and accrete gas towards their central regions along with concurrent star formation. This is argued to favour a ‘conveyor-belt’ mode of YMC formation.
- (iv) As part of the *CMZoom* survey with the SMA, the dust ridge clouds ‘b–f’ were observed at 230 GHz, with $\sim 4''$ angular resolution and 1.1 km s^{-1} spectral resolution. Dendrogram analysis reveals a population of high-mass pre/proto-stellar cores throughout the dust ridge, with masses ranging from $50 - 2150 M_{\odot}$ and radii of $0.1 - 0.25 \text{ pc}$. Of the 15 cores detected, 2 of them are found to contain newly discovered high-mass proto-stars. None of the cores have detected radio continuum emission, leading to the conclusion that these sources are ideal candidates for representing the very early stages of high-mass star formation in the CMZ.

- (v) Comparing the properties of the cores discovered with the SMA with those of high-mass proto-stellar cores in the Galactic disc shows that while they are of comparable mass and size, only 2 of the CMZ cores are proto-stellar, and the rest quiescent. This constitutes further evidence for an environmentally dependent critical density threshold for star formation in the CMZ, which is thought to be due to the high turbulent energy density there.
- (vi) Determining the masses of pre/proto-stellar cores in the CMZ is currently very uncertain. The dust and gas in the CMZ are known to be thermally uncoupled on global scales, but it is not known how this translates on to smaller scales. No direct measurements of the dust temperature exist on these scales, and it is not clear that using the gas temperature as a proxy is appropriate. More detailed models of the interplay between the gas and dust under these conditions and as a function of density are required such that we can begin to place tighter constraints on core masses via the dust continuum.

6.2 Concluding remarks

The work presented in this thesis constitutes a small step in what is a larger journey towards understanding how stars and clusters form under extreme conditions, and ultimately how this ties in with our knowledge of star formation as a whole.

Having shown that these dust ridge clouds are the best candidates for quiescent precursors to YMCs in the Galaxy, and that they harbour the likely initial conditions for high-mass star formation in the CMZ, paves the way for more detailed studies of the sources discovered, and how they interact with their natal environment. As noted in the previous chapter, on-going observations with ALMA are providing an unparalleled insight into the interiors of these cores. With facilities like ALMA, we are now able to study the process of stellar mass assembly in the turbulent environment of the CMZ at spatial resolutions and sensitivities that were previously only accessible for nearby star forming regions.

This work has primarily focused on a very specific region of the CMZ that spans only ~ 37 pc in Galactic longitude. The *CMZoom* survey has provided a complete census of the high-mass cores in the CMZ across a much larger range in longitude, and hence distance from the Galactic centre. Future studies like those presented here that include the full core catalogue promises to offer an unprecedented insight into the properties of high-mass cores as a function of their position in the inner Galaxy. This will pave the way for follow up studies with ALMA, and will significantly advance the current understanding of the formation of high-mass stars and clusters as a function of environment.

Appendix A

SMA data calibration and imaging

Chapter 4 of this thesis presented the 1.3 mm dust continuum and molecular line data from SMA observations of the Galactic centre dust ridge clouds ‘b’ – ‘f’. These observations were taken as part of a large legacy survey of the CMZ (*CMZoom*¹, PIs: Eric Keto and Cara Battersby, see Battersby et al. 2017). The survey was designed to target all regions within the CMZ that lie above a column density threshold of $\gtrsim 10^{23} \text{ cm}^{-2}$, with the aim of targeting the majority of the dense gas in the region, where it is most likely that stars and clusters should form. The *CMZoom* survey was conducted from May 2014 – September 2016, consisting of ~ 500 hours worth of mapping, corresponding to $\sim 240 \text{ arcmin}^2$ coverage of the CMZ at 230 GHz (1.3 mm). The typical angular resolution achieved is $\sim 4''$ (0.16 pc at a distance of 8.4 kpc) and the spectral resolution is $\sim 1.1 \text{ km s}^{-1}$. The target RMS is $\sim 3 \text{ mJy/beam}$ in the dust continuum.

The dust ridge data that are discussed in Chapter 4 comprise only a small fraction (4 tracks) of the total *CMZoom* survey. As part of the data reduction team, I was responsible for calibrating 18 individual tracks. The following section outlines the general method that was employed when calibrating all of the datasets.

¹More details of this survey can be found at <https://www.cfa.harvard.edu/sma/LargeScale/CMZ/>

Calibrating the SMA data

Data calibration for all SMA tracks was performed using the MIR software package. MIR is an IDL-based package that has been developed explicitly to calibrate data from the SMA. The general steps for calibrating the data in MIR are as follows –

Flagging: The data are initially loaded into MIR, and the continuum and spectra are inspected to look for any anomalous data points. Such data points are typically single outliers in the continuum and/or narrow, high-amplitude spikes in the spectra. These are most often caused by the electronics and must be flagged out prior to calibration. There are many other possible sources of bad data, such as atmospheric absorption lines, which are particularly troublesome at low elevation (high airmass).

T_{sys} correction: Prior to any further calibration, the data are first calibrated by the ‘chopper-wheel’ method. This corrects for variations in atmospheric opacity and electronic gain throughout the observation. The T_{sys} (system temperature) correction also weights the data by T_{sys}^2 . This correction provides an initial method of flux calibration, which is typically found to be accurate to within $\sim 20\%$.

Bandpass calibration: This step is important as it corrects for any variations in the phase and amplitude as a function of *frequency*. The corrections are based upon the observed phase and amplitude of a standard calibrator source. Ideal calibrator targets have bright, flat and line-free spectra. Quasars are often used for this purpose.

Gain calibration: This step corrects for any variations in the phase and amplitude as a function of *time*. Quasars are again commonly used for this step.

Flux calibration: Though the aforementioned ‘chopper-wheel’ method does a good job of calibrating the true fluxes of the observed sources, it can be improved upon. This improved flux calibration is often performed using Solar system

bodies (planets and moons) as calibrator sources, as their absolute fluxes are well known. A comparison between the observed and true flux provides a corrective factor – a single number that is ultimately used to scale the observed flux of the science target to match the true flux.

The actual process of data calibration is of course more detailed and nuanced than the above steps. The intent is to give a broad and general overview of the method.

Imaging the data

Once the data are calibrated and science-ready, they must be manipulated and imaged to yield the desired data products, such as continuum images and data cubes. There are several different software packages available for this. The method employed in this thesis uses both MIRIAD and CASA for continuum-line-separation and imaging.

As part of the data team for the *CMZoom* survey, I have written an automated imaging pipeline that is being used to take the calibrated datasets from the full survey and output a standardised set of data products². The following outlines the steps that this pipeline employs to produce these data products –

- (i) Any given science target in the survey will have at least 2 tracks covering it, one in the compact array configuration, and one in the subcompact. For larger maps, or those that were observed more than once (e.g. to improve noise or *uv*-coverage), there may be several tracks corresponding to one source. The first step of the pipeline is to load each track for the given source into MIR. This is done via executing a shell script, followed by the source name and paths to the relevant tracks, e.g. for a source with two tracks, the pipeline would be executed as –

```
pipeline.sh G0.123+4.567 track1.mir track2.mir
```

- (ii) Once loaded into MIR, the `idl2miriad` routine is used to output the lower and upper sidebands for all tracks as *.miriad* files.

²The pipeline can be found at <https://github.com/danw27/SMA-Imaging-Script>

-
- (ii) The *.miriad* files for both sidebands are loaded into MIRIAD. Here, edge channels are flagged on both sidebands via `uvflag`, and the continuum subtraction is performed using `uvlin`. As this is an automated process, only channels in which very bright line emission (e.g. ^{12}CO) is common are flagged for the continuum-line-separation. The `fits` command is then used to output *uvfits* files for the continuum and line data for each sideband, for all tracks covering the source.
 - (iii) All *uvfits* files are then loaded into CASA and imported as *.ms* files using the `importuvfits` command. Both the upper and lower continuum sidebands across all tracks are then concatenated into a single measurement set via `concat`. The upper and lower sidebands for the line data (cubes) are separately concatenated across all tracks.
 - (iv) The concatenated continuum and LSB/USB data cubes are all separately imaged (non-interactively) using the `clean` command in CASA. The `clean` parameters are loosely set, but can be modified by the user in the relevant python script. The resultant images are then output as *.fits* files via the `exportfits` command.
 - (v) To produce several data cubes of particular lines of interest for the survey, the python package `spectral_cube` is used to cut out slices of the LSB or USB cubes about the rest frequency of the desired lines. Currently, the script outputs cut-out cubes of SiO at 217.10498 GHz, H₂CO at 218.22219 (3_{0,3}-2_{0,2}), 218.47563 (3_{2,2}-2_{2,1}) and 218.76007 (3_{2,1}-2_{2,0}) GHz, and C¹⁸O at 219.56036 GHz, with a width of 0.15 GHz either side of the rest frequency.

This is a first iteration of the imaging pipeline for the *CMZoom* survey. Current testing is underway to improve the code, optimise `clean` parameters and automate more of the user inputs.

Appendix B

Images of HOPS YMC precursor candidates

This appendix presents images of the 7 HOPS sources that were identified as potential YMC precursor candidates in Chapter 5, section 3 of this thesis. Though 12 sources were initially identified, 5 of these were discarded as they are situated towards the Galactic centre, and thus their distances, line-widths and masses are not well constrained.

The following pages present, for each of the 7 sources, (i) a four-panel image displaying the dust continuum, integrated $\text{NH}_3(1,1)$ intensity, the $\text{NH}_3(1,1)$ velocity field and the $\text{NH}_3(1,1)$ velocity dispersion, and (ii) a three-colour image of the source, consisting of Herschel 70 μm (red), Spitzer/GLIMPSE 8 μm and dust continuum (blue), overlaid with the positions of catalogued CH_3OH (Caswell et al., 2010b, 2011) and H_2O (Walsh et al., 2011) masers. All images have contours of the ATLASGAL dust continuum (smoothed to the HOPS angular resolution) overlaid.

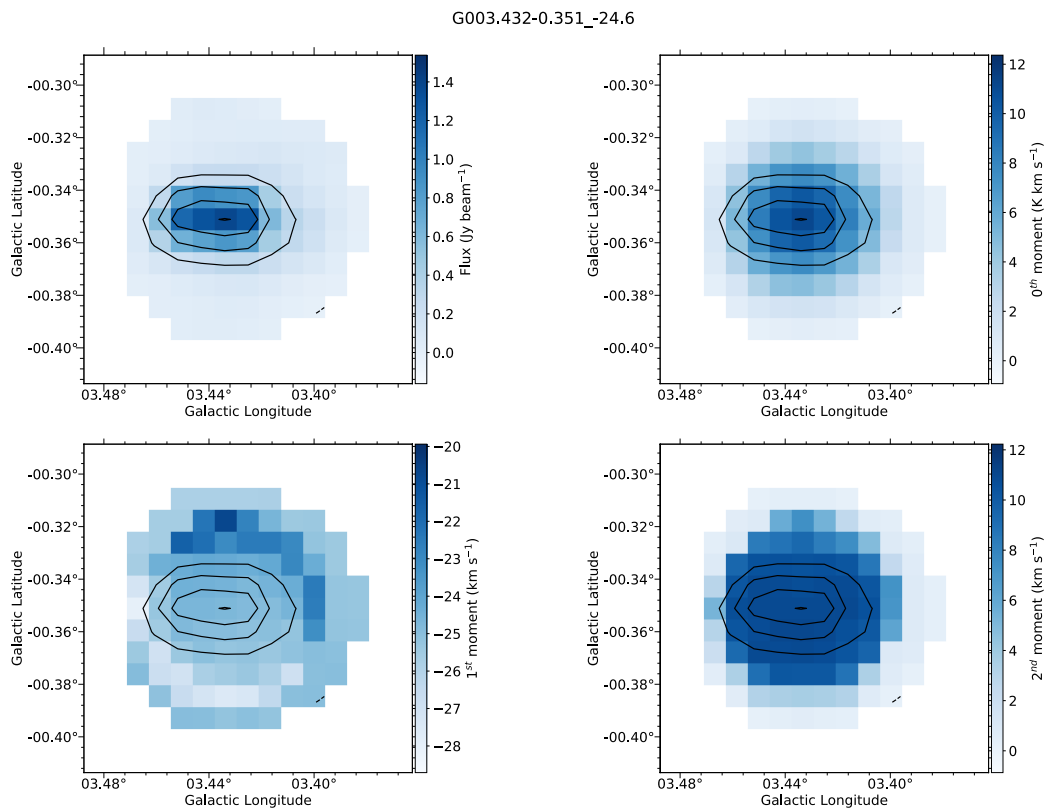


Figure B.1: ATLASGAL dust continuum, integrated NH₃(1,1) intensity, the NH₃(1,1) velocity field and the NH₃(1,1) velocity dispersion for G003.432-0.351. Black contours are from the dust continuum.

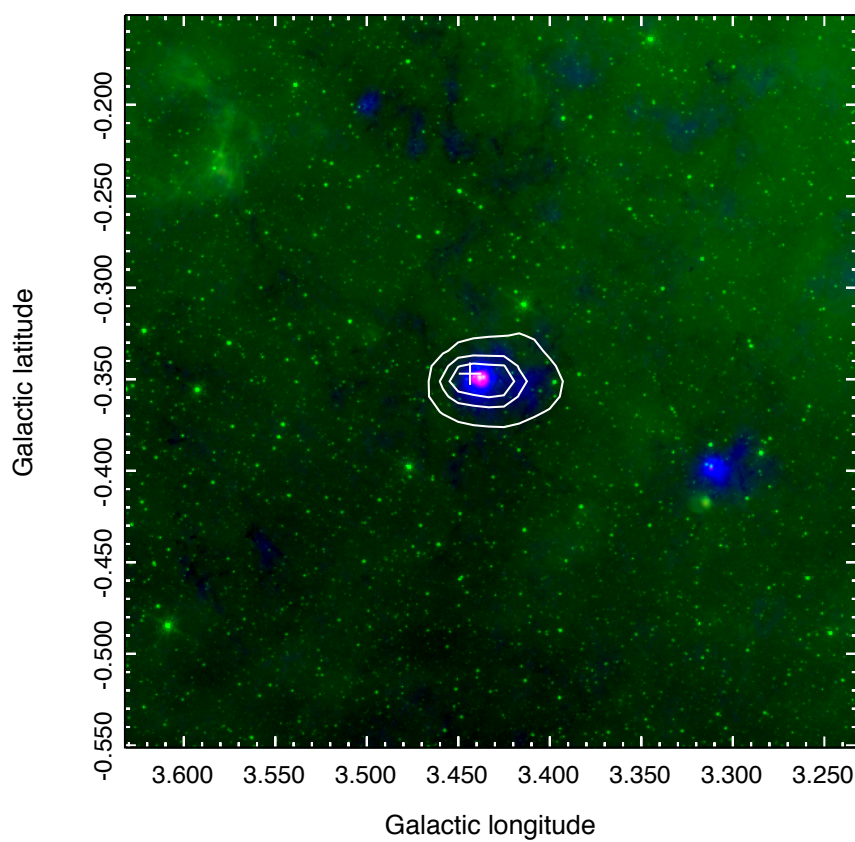


Figure B.2: Three-colour image of G003.432-0.351. Blue: ATLASGAL dust emission. Red: Herschel 70 μm emission. Green: GLIMPSE 8 μm emission. The white cross denotes the position of CH₃OH maser emission (Caswell et al., 2010b). White contours correspond to the ATLASGAL dust continuum, smoothed to the resolution of the HOPS data.

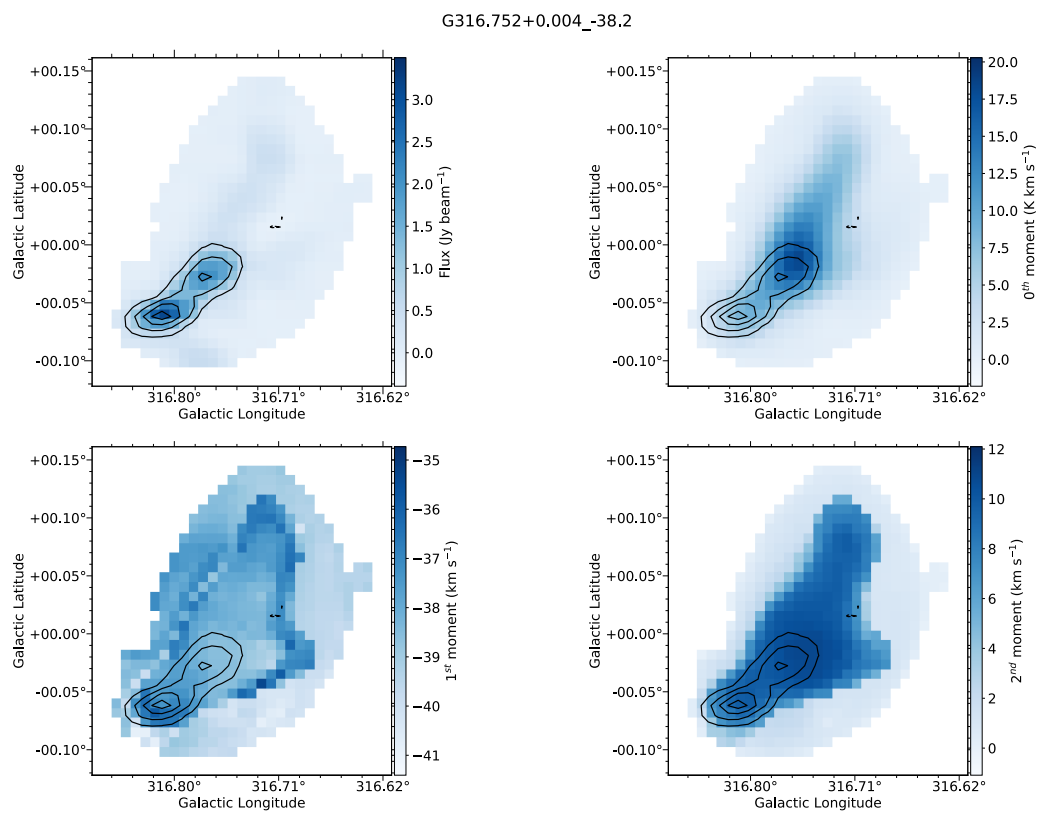


Figure B.3: ATLASGAL dust continuum, integrated NH₃(1,1) intensity, the NH₃(1,1) velocity field and the NH₃(1,1) velocity dispersion for G316.752+0.004. Black contours are from the dust continuum.

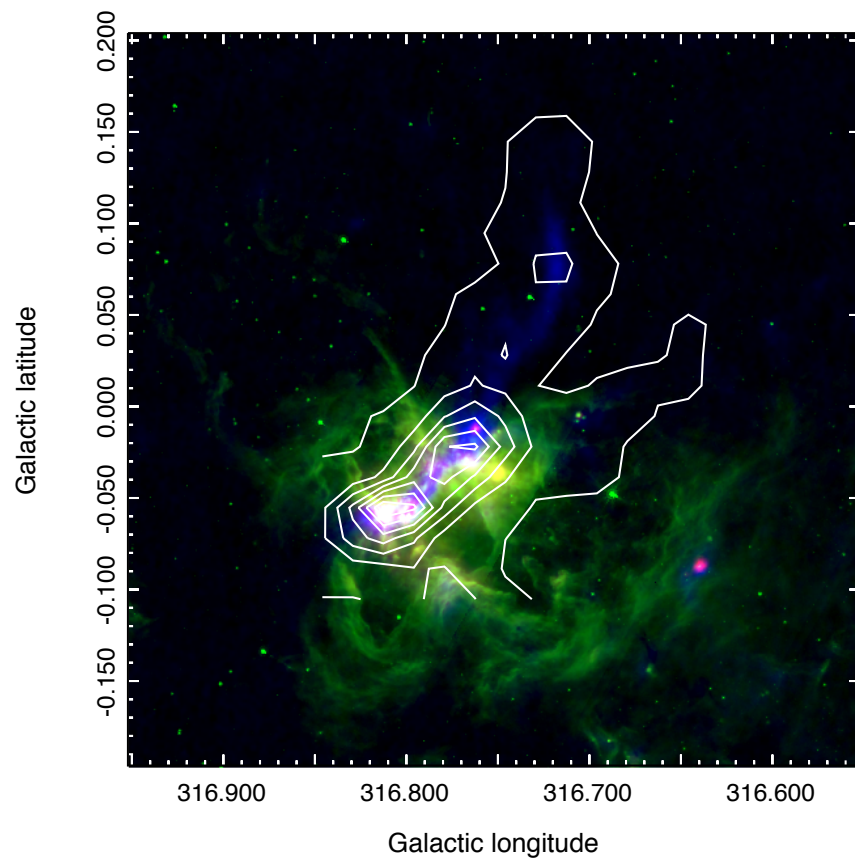


Figure B.4: Three-colour image of G316.752+0.004. Blue: ATLASGAL dust emission. Red: Herschel 70 μm emission. Green: GLIMPSE 8 μm emission. White contours correspond to the ATLASGAL dust continuum, smoothed to the resolution of the HOPS data.

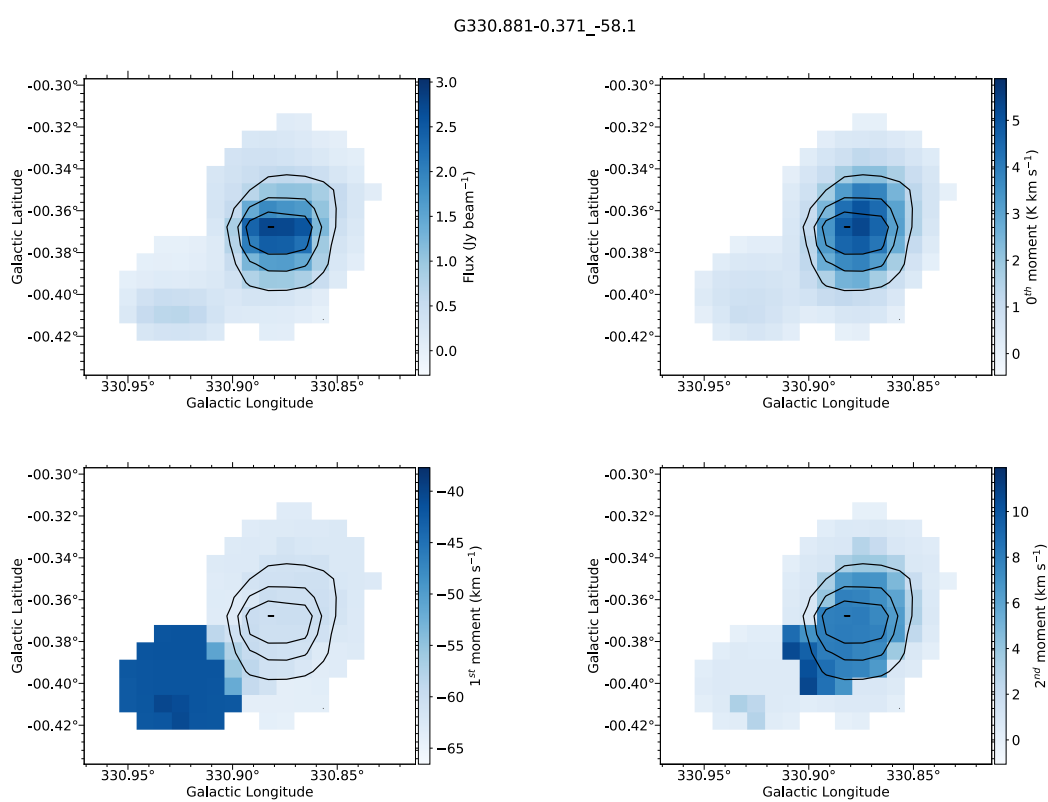


Figure B.5: ATLASGAL dust continuum, integrated NH₃(1,1) intensity, the NH₃(1,1) velocity field and the NH₃(1,1) velocity dispersion for G330.881-0.371. Black contours are from the dust continuum. Note that the clump to the lower left is unrelated.

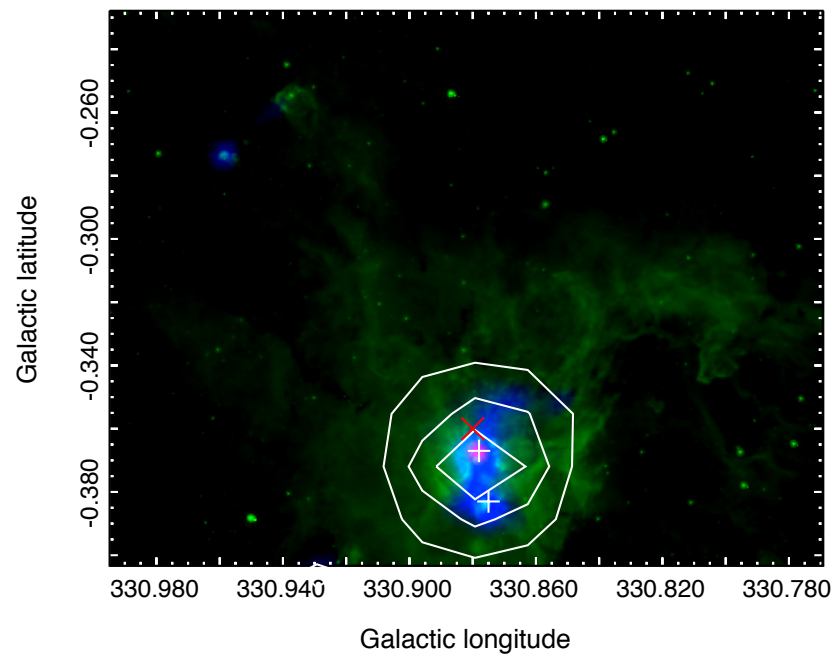


Figure B.6: Three-colour image of G330.881-0.371. Blue: ATLASGAL dust emission. Red: Herschel 70 μm emission. Green: GLIMPSE 8 μm emission. The white crosses mark the position of CH₃OH maser emission (Caswell et al., 2011). The red cross marks the position of H₂O maser emission (Walsh et al., 2011). White contours correspond to the ATLASGAL dust continuum, smoothed to the resolution of the HOPS data.

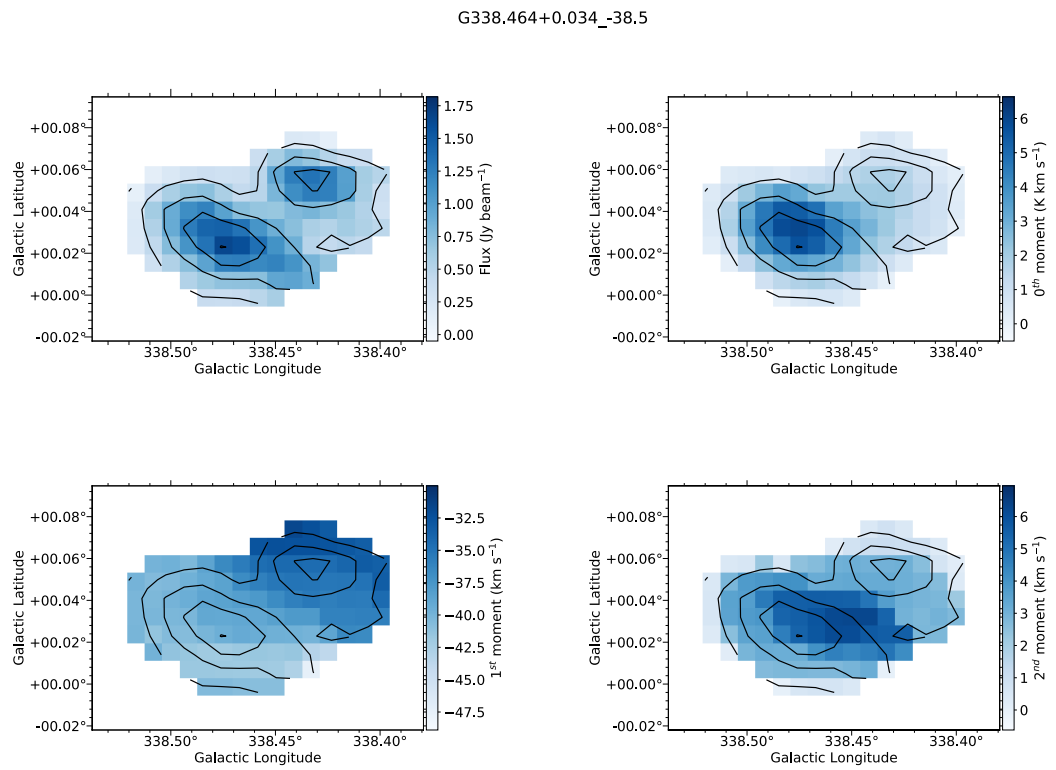


Figure B.7: ATLASGAL dust continuum, integrated $\text{NH}_3(1,1)$ intensity, the $\text{NH}_3(1,1)$ velocity field and the $\text{NH}_3(1,1)$ velocity dispersion for G338.464+0.034. Black contours are from the dust continuum.

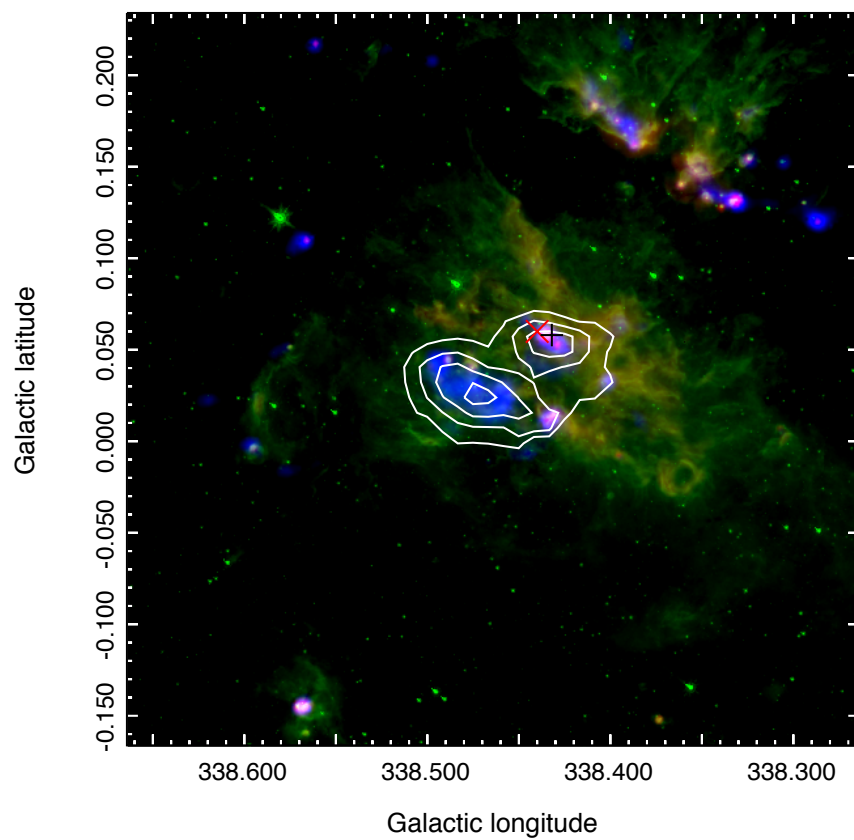


Figure B.8: Three-colour image of G338.464+0.034. Blue: ATLASGAL dust emission. Red: Herschel 70 μm emission. Green: GLIMPSE 8 μm emission. The black cross marks the position of CH₃OH maser emission (Caswell et al., 2011). The red cross marks the position of H₂O maser emission (Walsh et al., 2011). White contours correspond to the ATLASGAL dust continuum, smoothed to the resolution of the HOPS data.

G341.224-0.274_-43.8

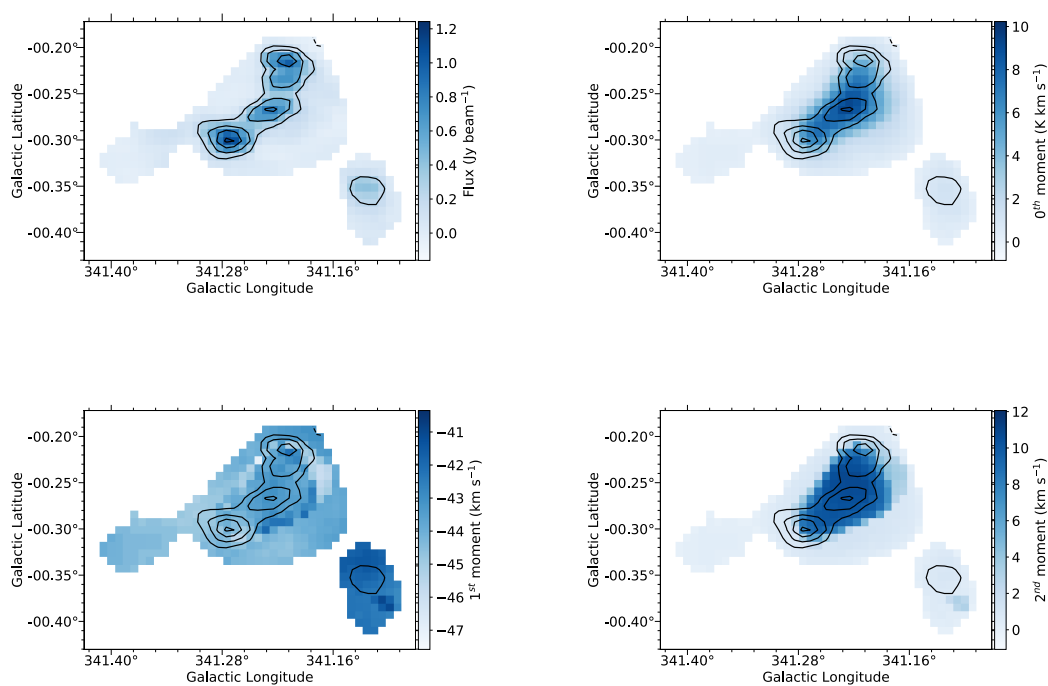


Figure B.9: ATLASGAL dust continuum, integrated NH₃(1,1) intensity, the NH₃(1,1) velocity field and the NH₃(1,1) velocity dispersion for G341.224-0.274. Black contours are from the dust continuum.

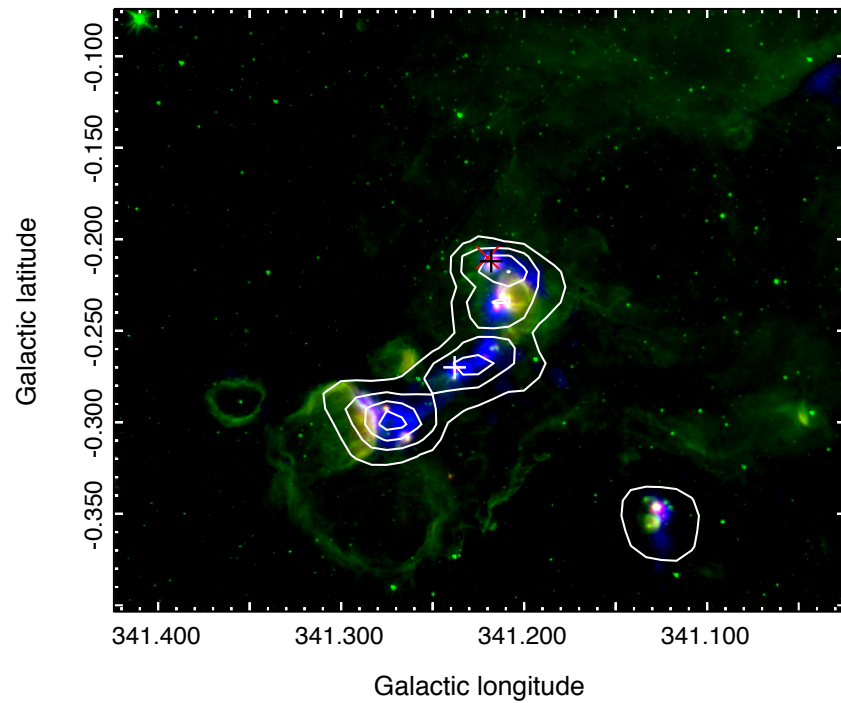


Figure B.10: Three-colour image of G341.224-0.274. Blue: ATLASGAL dust emission. Red: Herschel 70 μm emission. Green: GLIMPSE 8 μm emission. Black and white crosses mark the position of CH₃OH maser emission (Caswell et al., 2011). The red cross marks the position of H₂O maser emission (Walsh et al., 2011). White contours correspond to the ATLASGAL dust continuum, smoothed to the resolution of the HOPS data.

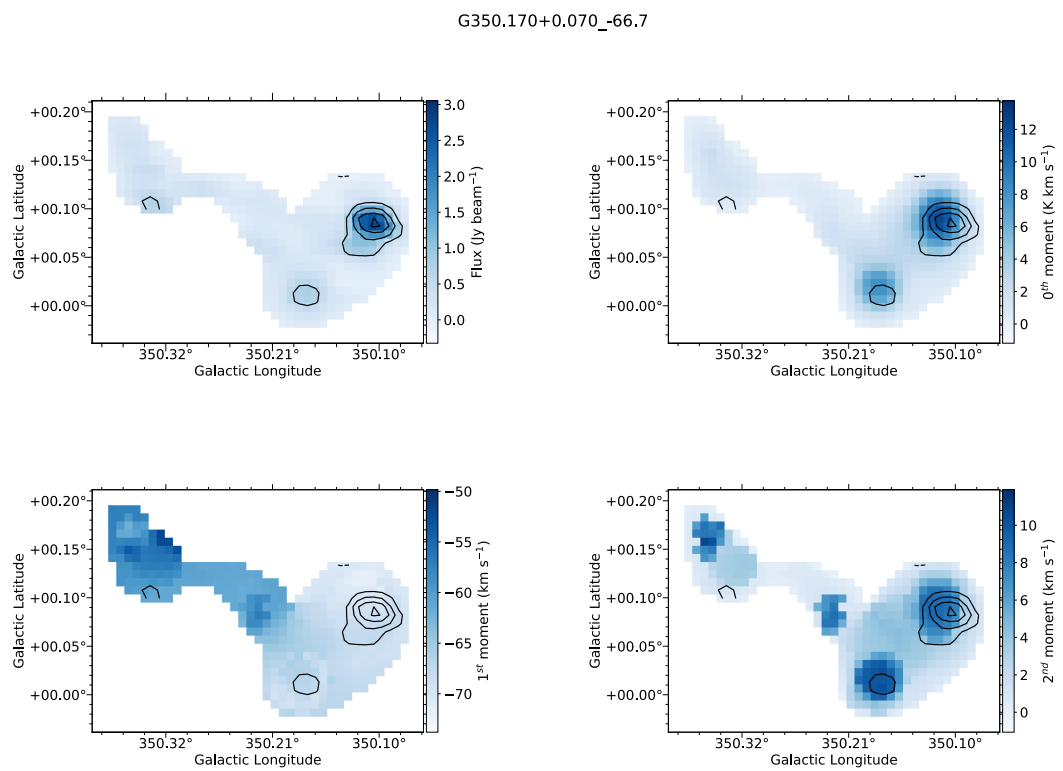


Figure B.11: ATLASGAL dust continuum, integrated $\text{NH}_3(1,1)$ intensity, the $\text{NH}_3(1,1)$ velocity field and the $\text{NH}_3(1,1)$ velocity dispersion for G350.170+0.070. Black contours are from the dust continuum.

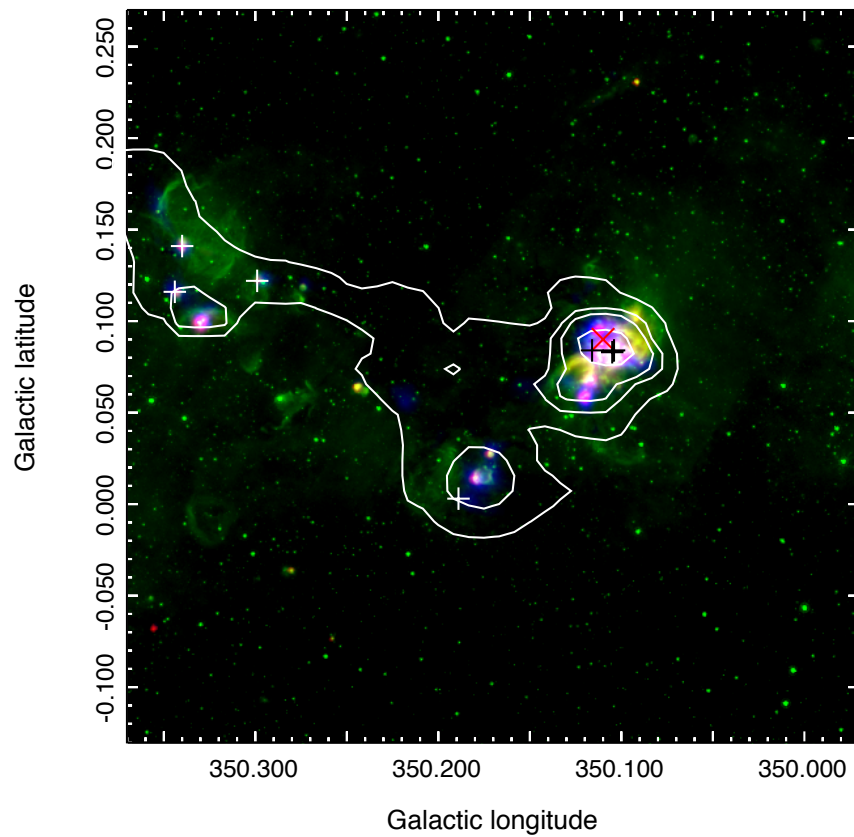


Figure B.12: Three-colour image of G350.170+0.070. Blue: ATLASGAL dust emission. Red: Herschel 70 μm emission. Green: GLIMPSE 8 μm emission. Black and white crosses mark the position of CH₃OH maser emission (Caswell et al., 2011). The red cross marks the position of H₂O maser emission (Walsh et al., 2011). White contours correspond to the ATLASGAL dust continuum, smoothed to the resolution of the HOPS data.

G357.555-0.323_+004.5

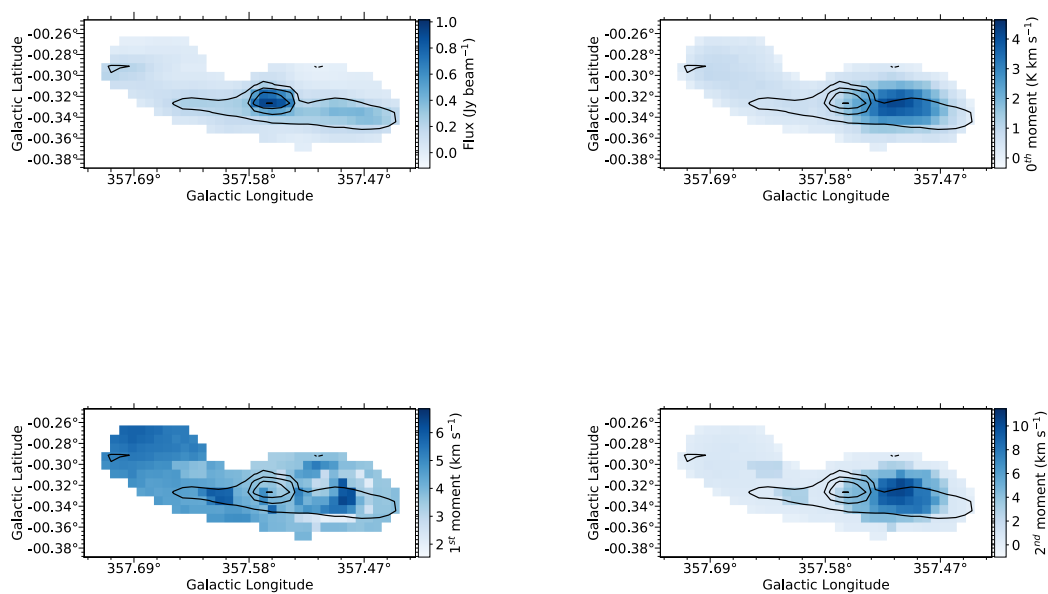


Figure B.13: ATLASGAL dust continuum, integrated NH₃(1,1) intensity, the NH₃(1,1) velocity field and the NH₃(1,1) velocity dispersion for G357.555-0.323. Black contours are from the dust continuum.

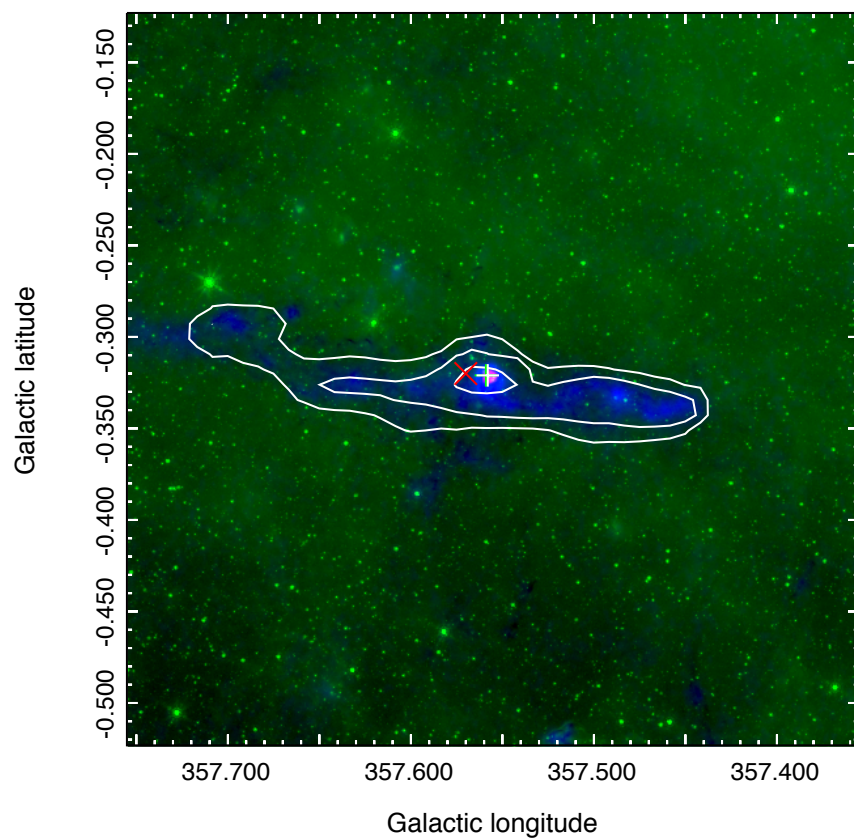


Figure B.14: Three-colour image of G357.555-0.323. Blue: ATLASGAL dust emission. Red: Herschel 70 μm emission. Green: GLIMPSE 8 μm emission. The white cross denotes the position of CH₃OH maser emission (Caswell et al., 2010b). The red cross marks the position of H₂O maser emission (Walsh et al., 2011). White contours correspond to the ATLASGAL dust continuum, smoothed to the resolution of the HOPS data.

Bibliography

- Aguirre J. E., Ginsburg A. G., Dunham M. K., et al 2011, *ApJS*, 192, 4
- Alves J., Lombardi M., Lada C. J., 2007, *A&A*, 462, L17
- André P., Men'shchikov A., Bontemps S., et al. 2010, *A&A*, 518, L102
- André P., Di Francesco J., Ward-Thompson D., Inutsuka S.-I., Pudritz R. E., Pineda J. E., 2014, *Protostars and Planets VI*, pp 27–51
- Ao Y., Henkel C., Menten K. M., et al 2013, *A&A*, 550, A135
- Arzoumanian D., André P., Didelon P., et al. 2011, *A&A*, 529, L6
- Ascenso J., Alves J., Vicente S., Lago M. T. V. T., 2007, *A&A*, 476, 199
- Assmann P., Fellhauer M., Kroupa P., Brüns R. C., Smith R., 2011, *MNRAS*, 415, 1280
- Bally J., 2016, *ARA&A*, 54, 491
- Bally J., Zinnecker H., 2005, *AJ*, 129, 2281
- Banerjee S., Kroupa P., 2013, *ApJ*, 764, 29
- Banerjee S., Kroupa P., 2014, *ApJ*, 787, 158
- Banerjee S., Kroupa P., 2015, *MNRAS*, 447, 728
- Barnard E., 1905, PLATE 41, In *Aquila, Northwest of Altair*
- Bastian N., Goodwin S. P., 2006, *MNRAS*, 369, L9

- Bastian N., Covey K. R., Meyer M. R., 2010, *ARA&A*, 48, 339
- Battersby C., Bally J., Ginsburg A., et al 2011, *A&A*, 535, A128
- Battersby C., Keto E., Zhang Q., et al. 2017, in Crocker R. M., Longmore S. N., Bicknell G. V., eds, *IAU Symposium Vol. 322, The Multi-Messenger Astrophysics of the Galactic Centre*. pp 90–94 (<http://arxiv.org/abs/1610.05805> arXiv:1610.05805)
- Baumgardt H., Kroupa P., 2007, *MNRAS*, 380, 1589
- Bigiel F., Leroy A. K., Jiménez-Donaire M. J., et al 2016, *ApJ*, 822, L26
- Boily C. M., Kroupa P., 2003, *MNRAS*, 338, 673
- Bonnell I. A., Davies M. B., 1998, *MNRAS*, 295, 691
- Bonnell I. A., Bate M. R., Clarke C. J., Pringle J. E., 2001, *MNRAS*, 323, 785
- Brandner W., Clark J. S., Stolte A., Waters R., Negueruela I., Goodwin S. P., 2008, *A&A*, 478, 137
- Bressert E., Bastian N., Evans C. J., et al. 2012a, *A&A*, 542, A49
- Bressert E., Ginsburg A., Bally J., et al 2012b, *ApJ*, 758, L28
- Cabrera-Ziri I., et al., 2016, *MNRAS*, 457, 809
- Carey S. J., Noriega-Crespo A., Mizuno D. R., et al 2009, , 121, 76
- Caswell J. L., Fuller G. A., Green J. A., et al 2010a, *MNRAS*, 404, 1029
- Caswell J. L., et al., 2010b, *MNRAS*, 404, 1029
- Caswell J. L., et al., 2011, *MNRAS*, 417, 1964
- Cesaroni R., Churchwell E., Hofner P., Walmsley C. M., Kurtz S., 1994, *A&A*, 288
- Cesaroni R., Hofner P., Araya E., Kurtz S., 2010, *A&A*, 509, A50
- Chabrier G., 2003, , 115, 763

- Churchwell E., et al., 2009, , 121, 213
- Clark J. S., Negueruela I., Crowther P. A., Goodwin S. P., 2005, *A&A*, 434, 949
- Clark P. C., Glover S. C. O., Ragan S. E., et al 2013, *ApJ*, 768, L34
- Conroy C., van Dokkum P. G., 2012, *ApJ*, 760, 71
- Contreras Y., Rathborne J. M., Guzman A., Jackson J., Whitaker S., Sanhueza P., Foster J., 2017, *MNRAS*, 466, 340
- Cyganowski C. J., Brogan C. L., Hunter T. R., et al. 2014, *ApJ*, 796, L2
- Cyganowski C. J., Brogan C. L., Hunter T. R., et al. 2017, *MNRAS*, 468, 3694
- Dale J. E., Ercolano B., Bonnell I. A., 2015, *MNRAS*, 451, 987
- Davies B., Figer D. F., Kudritzki R.-P., et al 2007, *ApJ*, 671, 781
- De Pree C. G., Wilner D. J., Goss W. M., 2011, *AJ*, 142, 177
- Di Francesco J., Johnstone D., Kirk H., et al 2008, *ApJS*, 175, 277
- Draine B. T., 2011, *Physics of the Interstellar and Intergalactic Medium*
- Elitzur M., Watson W. D., Western L. R., 1983, *ApJ*, 274, 210
- Elmegreen B. G., 2008, *ApJ*, 672, 1006
- Elmegreen B. G., Efremov Y. N., 1997, *ApJ*, 480, 235
- Elson R. A. W., Fall S. M., Freeman K. C., 1987, *ApJ*, 323, 54
- Espinoza P., Selman F. J., Melnick J., 2009, *A&A*, 501, 563
- Fall S. M., Zhang Q., 2001, *ApJ*, 561, 751
- Field G. B., Blackman E. G., Keto E. R., 2011, *MNRAS*, 416, 710
- Figer D. F., McLean I. S., Morris M., 1999a, *ApJ*, 514, 202

- Figer D. F., Kim S. S., Morris M., Serabyn E., Rich R. M., McLean I. S., 1999b, *ApJ*, 525, 750
- Figer D. F., Kim S. S., Morris M., Serabyn E., Rich R. M., McLean I. S., 1999c, *ApJ*, 525, 750
- Figer D. F., et al., 2002, *ApJ*, 581, 258
- Forster J. R., Caswell J. L., 1999a, *A&A Supplement*, 137, 43
- Forster J. R., Caswell J. L., 1999b, *A&A Supplement*, 137, 43
- Foster J. B., Jackson J. M., Barnes P. J., et al 2011, *ApJS*, 197, 25
- Foster J. B., Rathborne J. M., Sanhueza P., et al 2013, *PASA*, 30, 38
- Fujii M. S., Saitoh T. R., Portegies Zwart S. F., 2012, *ApJ*, 753, 85
- Galli D., Walmsley M., Gonçalves J., 2002, *A&A*, 394, 275
- Galván-Madrid R., Liu H. B., Zhang Z.-Y., et al 2013, *ApJ*, 779, 121
- Gaume R. A., Claussen M. J., de Pree C. G., et al 1995, *ApJ*, 449, 663
- Gennaro M., Brandner W., Stolte A., Henning T., 2011, *MNRAS*, 412, 2469
- Ginsburg A., Bressert E., Bally J., Battersby C., 2012, *ApJ*, 758, L29
- Ginsburg A., Glenn J., Rosolowsky E., et al 2013, *ApJS*, 208, 14
- Ginsburg A., Walsh A., Henkel C., et al 2015, *A&A*, 584, L7
- Ginsburg A., Goss W. M., Goddi C., et al 2016a, preprint
(<http://arxiv.org/abs/1605.09402> arXiv:1605.09402)
- Ginsburg A., Henkel C., Ao Y., et al 2016b, *A&A*, 586, A50
- Girichidis P., Federrath C., Banerjee R., Klessen R. S., 2012, *MNRAS*, 420, 613
- Goddard Q. E., Bastian N., Kennicutt R. C., 2010, *MNRAS*, 405, 857

- Goddi C., Greenhill L. J., Chandler C. J., Humphreys E. M. L., Matthews L. D., Gray M. D., 2009, *ApJ*, 698, 1165
- Goldsmith P. F., Langer W. D., 1978, *ApJ*, 222, 881
- Goss W. M., Radhakrishnan V., 1969, , 4, 199
- Greenhill L. J., Goddi C., Chandler C. J., Matthews L. D., Humphreys E. M. L., 2013, *ApJ*, 770, L32
- Griffin M. J., Abergel A., Abreu A., et al. 2010, *A&A*, 518, L3
- Harayama Y., Eisenhauer F., Martins F., 2008, *ApJ*, 675, 1319
- Harfst S., Portegies Zwart S., Stolte A., 2010, *MNRAS*, 409, 628
- Hartmann L., 1998, *Accretion Processes in Star Formation*
- Hartmann L., Herczeg G., Calvet N., 2016, *ARA&A*, 54, 135
- Heggie D., Hut P., 2003, *The Gravitational Million-Body Problem: A Multidisciplinary Approach to Star Cluster Dynamics*
- Heiderman A., Evans II N. J., Allen L. E., Huard T., Heyer M., 2010, *ApJ*, 723, 1019
- Henshaw J. D., Longmore S. N., Kruijssen J. M. D., et al 2016, *MNRAS*, 457, 2675
- Heyer M., Krawczyk C., Duval J., Jackson J. M., 2009, *ApJ*, 699, 1092
- Holtzman J. A., Faber S. M., Shaya E. J., Lauer T. R., et al 1992, *AJ*, 103, 691
- Hopkins A. M., Beacom J. F., 2006, *ApJ*, 651, 142
- Hopkins P. F., Murray N., Quataert E., Thompson T. A., 2010, *MNRAS*, 401, L19
- Immer K., Menten K. M., Schuller F., Lis D. C., 2012, *A&A*, 548, A120
- Immer K., Kauffmann J., Pillai T., Ginsburg A., Menten K. M., 2016, preprint (<http://arxiv.org/abs/1607.03535> arXiv:1607.03535)
- Jackson J. M., Rathborne J. M., Shah R. Y., et al 2006, *ApJS*, 163, 145

- Jackson J. M., Rathborne J. M., Foster J. B., et al 2013, *PASA*, 30, 57
- Jeans J. H., 1902, *Philosophical Transactions of the Royal Society of London Series A*, 199, 1
- Johnston K. G., Beuther H., Linz H., Schmiedeke A., Ragan S. E., Henning T., 2014, *A&A*, 568, A56
- Kauffmann J., Pillai T., 2010, *ApJ*, 723, L7
- Kauffmann J., Bertoldi F., Bourke T. L., Evans II N. J., Lee C. W., 2008, *A&A*, 487, 993
- Kauffmann J., Pillai T., Zhang Q., 2013a, *ApJ*, 765, L35
- Kauffmann J., Pillai T., Goldsmith P. F., 2013b, *ApJ*, 779, 185
- Kauffmann J., Pillai T., Zhang Q., et al 2016a, preprint (<http://arxiv.org/abs/1610.03499> arXiv:1610.03499)
- Kauffmann J., Pillai T., Zhang Q., et al 2016b, preprint (<http://arxiv.org/abs/1610.03502> arXiv:1610.03502)
- Keto E., 2007, *ApJ*, 666, 976
- Kim S. S., Morris M., Lee H. M., 1999, *ApJ*, 525, 228
- Kong S., Tan J. C., Caselli P., et al. 2017, *ApJ*, 834, 193
- Kroupa P., 2001, *MNRAS*, 322, 231
- Kruijssen J. M. D., 2012, *MNRAS*, 426, 3008
- Kruijssen J. M. D., 2014, *Classical and Quantum Gravity*, 31, 244006
- Kruijssen J. M. D., 2015, *MNRAS*, 454, 1658
- Kruijssen J. M. D., Longmore S. N., 2013, *MNRAS*, 435, 2598
- Kruijssen J. M. D., Maschberger T., Moeckel N., et al 2012, *MNRAS*, 419, 841

- Kruijssen J. M. D., Longmore S. N., Elmegreen B. G., et al 2014, MNRAS, 440, 3370
- Kruijssen J. M. D., Dale J. E., Longmore S. N., 2015, MNRAS, 447, 1059
- Krumholz M. R., Kruijssen J. M. D., 2015, MNRAS, 453, 739
- Krumholz M. R., McKee C. F., 2005, ApJ, 630, 250
- Krumholz M. R., McKee C. F., 2008, Nature, 451, 1082
- Krumholz M. R., Klein R. I., McKee C. F., Offner S. S. R., Cunningham A. J., 2009, Science, 323, 754
- Krumholz M. R., Dekel A., McKee C. F., 2012, ApJ, 745, 69
- Krumholz M. R., Kruijssen J. M. D., Crocker R. M., 2016, preprint (<http://arxiv.org/abs/1605.02850> arXiv:1605.02850)
- Kuiper R., Klahr H., Beuther H., Henning T., 2011, ApJ, 732, 20
- Lada C. J., Lada E. A., 2003, ARA&A, 41, 57
- Lada C. J., Margulis M., Dearborn D., 1984, ApJ, 285, 141
- Lada C. J., Lombardi M., Alves J. F., 2010a, ApJ, 724, 687
- Lada C. J., Lombardi M., Alves J. F., 2010b, ApJ, 724, 687
- Lada C. J., Forbrich J., Lombardi M., Alves J. F., 2012, ApJ, 745, 190
- Larsen S. S., 2009, A&A, 494, 539
- Larson R. B., 1969, MNRAS, 145, 271
- Larson R. B., 1981, MNRAS, 194, 809
- Larson R. B., 2003, Reports on Progress in Physics, 66, 1651
- Lis D. C., Menten K. M., 1998, ApJ, 507, 794
- Lis D. C., Menten K. M., Serabyn E., Zylka R., 1994, ApJ, 423, L39

- Lis D. C., Li Y., Dowell C. D., Menten K. M., 1999, in Cox P., Kessler M., eds, ESA Special Publication Vol. 427, The Universe as Seen by ISO. p. 627
- Longmore S. N., Burton M. G., Barnes P. J., Wong T., Purcell C. R., Ott J., 2007, MNRAS, 379, 535
- Longmore S. N., Pillai T., Keto E., Zhang Q., Qiu K., 2011, ApJ, 726, 97
- Longmore S. N., Rathborne J., Bastian N., et al 2012, ApJ, 746, 117
- Longmore S. N., Bally J., Testi L., et al 2013a, MNRAS, 429, 987
- Longmore S. N., Kruijssen J. M. D., Bally J., et al 2013b, MNRAS, 433, L15
- Longmore S. N., Kruijssen J. M. D., Bastian N., et al 2014a, Protostars and Planets VI, pp 291–314
- Longmore S. N., Kruijssen J. M. D., Bastian N., et al 2014b, Protostars and Planets VI, pp 291–314
- Longmore S., et al., 2016, preprint (<http://arxiv.org/abs/1601.02654> arXiv:1601.02654)
- Louvet F., Motte F., Hennebelle P., et al 2014, A&A, 570, A15
- MacLaren I., Richardson K. M., Wolfendale A. W., 1988, ApJ, 333, 821
- Madau P., Dickinson M., 2014, ARA&A, 52, 415
- Mangum J. G., Shirley Y. L., 2015, , 127, 266
- Maraston C., Bastian N., Saglia R. P., et al 2004, A&A, 416, 467
- Marks M., Kroupa P., 2012, A&A, 543, A8
- Matzner C. D., McKee C. F., 2000, ApJ, 545, 364
- McKee C. F., Ostriker E. C., 2007, ARA&A, 45, 565
- McKee C. F., Tan J. C., 2003, ApJ, 585, 850

- McMullin J. P., Waters B., Schiebel D., Young W., Golap K., 2007, in Shaw R. A., Hill F., Bell D. J., eds, *Astronomical Society of the Pacific Conference Series Vol. 376, Astronomical Data Analysis Software and Systems XVI*. p. 127
- Molinari S., Swinyard B., Bally J., et al 2010, , 122, 314
- Molinari S., Bally J., Noriega-Crespo A., et al 2011, *ApJ*, 735, L33
- Molinari S., Schisano E., Elia D., et al 2016, preprint (<http://arxiv.org/abs/1604.05911>
arXiv:1604.05911)
- Morris M., Serabyn E., 1996, *ARA&A*, 34, 645
- Nordlund Å. K., Padoan P., 1999, in Franco J., Carraminana A., eds, *Interstellar Turbulence*. p. 218 (<http://arxiv.org/abs/astro-ph/9810074>
arXiv:astro-ph/9810074)
- Oka T., Hasegawa T., Sato F., et al 2001, *ApJ*, 562, 348
- Ossenkopf V., Henning T., 1994, *A&A*, 291, 943
- Ostriker E. C., Stone J. M., Gammie C. F., 2001, *ApJ*, 546, 980
- Padoan P., Nordlund Å., 2011, *ApJ*, 730, 40
- Padoan P., Jones B. J. T., Nordlund Å. P., 1997, *ApJ*, 474, 730
- Padoan P., Federrath C., Chabrier G., Evans II N. J., Johnstone D., Jørgensen J. K., McKee C. F., Nordlund Å., 2014, *Protostars and Planets VI*, pp 77–100
- Panagia N., 1973, *AJ*, 78, 929
- Parker R. J., Wright N. J., Goodwin S. P., Meyer M. R., 2014a, *MNRAS*, 438, 620
- Parker R. J., Wright N. J., Goodwin S. P., Meyer M. R., 2014b, *MNRAS*, 438, 620
- Peretto N., Fuller G. A., Duarte-Cabral A., et al 2013, *A&A*, 555, A112
- Pillai T., Kauffmann J., Tan J. C., et al 2015, *ApJ*, 799, 74

- Plummer H. C., 1911, MNRAS, 71, 460
- Poglitsch A., Waelkens C., Geis N., et al. 2010, A&A, 518, L2
- Portegies Zwart S. F., Makino J., McMillan S. L. W., Hut P., 2002, ApJ, 565, 265
- Portegies Zwart S. F., McMillan S. L. W., Gieles M., 2010, ARA&A, 48, 431
- Qin S.-L., Schilke P., Rolffs R., et al 2011, A&A, 530, L9
- Rathborne J. M., Longmore S. N., Jackson J. M., et al 2014a, ApJ, 786, 140
- Rathborne J. M., Longmore S. N., Jackson J. M., et al 2014b, ApJ, 795, L25
- Rathborne J. M., et al., 2015, ApJ, 802, 125
- Reid M. J., et al., 2009a, ApJ, 700, 137
- Reid M. J., Menten K. M., Zheng X. W., et al 2009b, ApJ, 700, 137
- Reid M. J., Menten K. M., Brunthaler A., et al 2014, ApJ, 783, 130
- Rochau B., Brandner W., Stolte A., et al 2010, ApJ, 716, L90
- Roman-Duval J., Jackson J. M., Heyer M., et al 2010, ApJ, 723, 492
- Rosolowsky E. W., Pineda J. E., Kauffmann J., Goodman A. A., 2008, ApJ, 679, 1338
- Rosolowsky E., Dunham M. K., Ginsburg A., et al 2010, ApJS, 188, 123
- Salpeter E. E., 1955, ApJ, 121, 161
- Sana H., Momany Y., Gieles M., et al 2010, A&A, 515, A26
- Sault R. J., Teuben P. J., Wright M. C. H., 1995, in Shaw R. A., Payne H. E., Hayes J. J. E., eds, *Astronomical Society of the Pacific Conference Series Vol. 77, Astronomical Data Analysis Software and Systems IV*. p. 433 (<http://arxiv.org/abs/astro-ph/0612759> arXiv:astro-ph/0612759)
- Schmiedeke A., et al., 2016, A&A, 588, A143

- Schneider F. R. N., Izzard R. G., de Mink S. E., et al 2014, *ApJ*, 780, 117
- Schöier F. L., van der Tak F. F. S., van Dishoeck E. F., Black J. H., 2005, *A&A*, 432, 369
- Schuller F., Menten K. M., Contreras Y., et al 2009, *A&A*, 504, 415
- Shetty R., Beaumont C. N., Burton M. G., Kelly B. C., Klessen R. S., 2012, *MNRAS*, 425, 720
- Silva-Villa E., Larsen S. S., 2011, *A&A*, 529, A25
- Smith R. J., Longmore S., Bonnell I., 2009, *MNRAS*, 400, 1775
- Solomon P. M., Rivolo A. R., Barrett J., Yahil A., 1987, *ApJ*, 319, 730
- Stolte A., Hußmann B., Morris M. R., et al 2014, *ApJ*, 789, 115
- Tan J. C., Kong S., Butler M. J., et al. 2013, *ApJ*, 779, 96
- Tan J. C., Beltrán M. T., Caselli P., Fontani F., Fuente A., Krumholz M. R., McKee C. F., Stolte A., 2014, *Protostars and Planets VI*, pp 149–172
- Tremblay C. D., Walsh A. J., Longmore S. N., Urquhart J. S., König C., 2015, *PASA*, 32, e047
- Turner B. E., Matthews H. E., 1984, *ApJ*, 277, 164
- Urquhart J. S., Moore T. J. T., Schuller F., et al 2013, *MNRAS*, 431, 1752
- Urquhart J. S., et al., 2014, *MNRAS*, 443, 1555
- Usero A., Leroy A. K., Walter F., et al 2015, *AJ*, 150, 115
- Vacca W. D., Garmany C. D., Shull J. M., 1996, *ApJ*, 460, 914
- Valdettaro R., Palla F., et al. 2001, *A&A*, 368, 845
- Vazquez-Semadeni E., 1994, *ApJ*, 423, 681
- Vesperini E., 2001, *MNRAS*, 322, 247

- Walker D. L., Longmore S. N., Bastian N., Kruijssen J. M. D., Rathborne J. M., Jackson J. M., Foster J. B., Contreras Y., 2015, *MNRAS*, 449, 715
- Walker D. L., Longmore S. N., Bastian N., et al 2016, *MNRAS*, 457, 4536
- Walsh A. J., Breen S. L., Britton T., et al. 2011, *MNRAS*, 416, 1764
- Whitmore B. C., 2002, in Geisler D. P., Grebel E. K., Minniti D., eds, *IAU Symposium Vol. 207, Extragalactic Star Clusters*. p. 367
- Wienen M., Wyrowski F., Schuller F., Menten K. M., Walmsley C. M., Bronfman L., Motte F., 2012, *A&A*, 544, A146
- Wright N. J., Parker R. J., Goodwin S. P., Drake J. J., 2014, *MNRAS*, 438, 639
- Zapata L. A., Menten K., Reid M., Beuther H., 2009a, *ApJ*, 691, 332
- Zapata L. A., Menten K., Reid M., Beuther H., 2009b, *ApJ*, 691, 332
- Zinnecker H., Yorke H. W., 2007, *ARA&A*, 45, 481
- van der Tak F. F. S., Black J. H., Schöier F. L., Jansen D. J., van Dishoeck E. F., 2007, *A&A*, 468, 627